SKIN BARRIER FUNCTION ASSESSED QUANTITATIVELY AND NONINVASIVELY WITH MULTIMODAL MICROSCOPY AND SPECTROSCOPY METHODS

by

MARY CATHERINE MACK

A dissertation submitted to the

Graduate School-New Brunswick

Rutgers, The State University of New Jersey

and

The Graduate School of Biomedical Sciences

In partial fulfillment of the requirements

For the degree of

Doctor of Philosophy

Graduate Program in Biomedical Engineering

Written under the direction of

Nada N. Boustany

And approved by

_____

_____

_____

_____

New Brunswick, New Jersey

October, 2015

ABSTRACT OF THE DISSERTATION

Skin Barrier Function Assessed Quantitatively and Noninvasively with Multimodal Microscopy and Spectroscopy Methods

By MARY CATHERINE MACK

Dissertation Director:

Nada N. Boustany

The skin barrier is responsible for regulating water loss and preventing penetration of exogenous substances into the body. Traditional measurement techniques rely on invasive sampling through biopsy or the measurement of macroscopic parameters. Non-invasive skin measurement methodologies which probe skin biology and biophysics are therefore needed to expand our understanding of disease and non-disease states and to establish methods for assessing therapies targeted towards skin barrier.

The goal of this work is to identify quantitative physiological and functional parameters of skin barrier suitable for non-invasive measurement, and establish the usefulness of these parameters to monitor barrier quality through in-vivo proof-of-principle studies utilizing models of controlled barrier disruption. Specifically, we investigate changes in endpoints related to epidermal morphology and endpoints related to composition and molecular order of stratum corneum (SC) lipids. Through controlled disruption of skin barrier function and measurement of morphological and compositional parameters by

non-invasive microscopy and spectroscopy techniques, the contribution of these parameters to skin barrier function may be quantified.

To evaluate the morphological contribution to skin barrier function, we utilize a tape stripping methodology to partially remove the SC. We observe that in addition to the expected increase in water loss resulting from altering the diffusion gradient across the SC, morphological changes are induced in the viable epidermis immediately after tape stripping and continue to evolve in the days following the tape stripping barrier insult. Thus, monitoring the cell size and epidermal layer thickness may provide insight into the immediate and longer term responses of the skin, including lamellar body degranulation, proliferation, and differentiation. We also probed the contribution of the composition and organization of the SC barrier lipids to overall skin barrier function. In vivo infrared spectroscopy and fluorescence microscopy were used to demonstrate the impact of disordering SC lipids and link the molecular interaction of exogenous agents with SC lipids to the resulting changes in barrier function. Through this work, methodologies were developed utilizing non-invasive multimodal microscopy and spectroscopy techniques to quantify skin properties at the molecular and cellular level and to relate these endpoints to the overall skin barrier function.

ACKNOWLEDGEMENTS

The materials, images and text used in Chapters 4 and 5 of this thesis have been previously published, at least in part, as original manuscripts in Experimental Dermatology and Langmuir (M. Catherine Mack Correa, Guangru Mao, Peter Saad, Carol R. Flach, Richard Mendelsohn, Russel M. Walters. "Molecular Interactions of Plant Oil Components Correlate with Clinical Measures of Skin Barrier Function", Experimental Dermatology, 23:39-44, 2014; Guangru Mao, Dina VanWyck, Xin Xiao, M. Catherine Mack Correa, Euen Gunn, Carol R. Flach, Richard Mendelsohn, Russel M. Walters. "Oleic Acid Disorders Stratum Corneum Lipids in Langmuir Monolayers", Langmuir, 29:4857-65, 2013).

I would like to thank my family: Mom, Dad, James, Lena, Aunt Mary, Uncle Steve, and those whom I consider my family: Mary Lou, Bob, Julia for always supporting me however and whenever I needed it. I would also like to thank my colleagues and management at Johnson & Johnson as well as Dr. Boustany and the BME department for their support and flexibility, without which I would not have been able to achieve this goal. I would finally like to thank the J&J / Rutgers Newark crew, including Dr. Mendelsohn, Carol, Guangru, and Russ, for a stimulating collaboration over these past years.

TABLE OF CONTENTS

LIST OF TABLES

LIST OF FIGURES

CHAPTER 1 Introduction and Novel Contributions

1.1 Epidermal Structure

The epidermis may be divided into four layers, based on cellular morphology and differentiation status (Figure 1.1). The stratum basale (SB) consists of one layer of columnar-shaped keratinocytes bound to the basement membrane of the dermal-epidermal junction (DEJ). As basal cells divide, the daughter cells move up into the epidermis, and the differentiation process begins. Epidermal differentiation is a form of non-apoptotic, programmed cell death which is associated with the formation of stratified, sheet-like ultrastructure, and is orchestrated across all the cells of the epidermis [1].

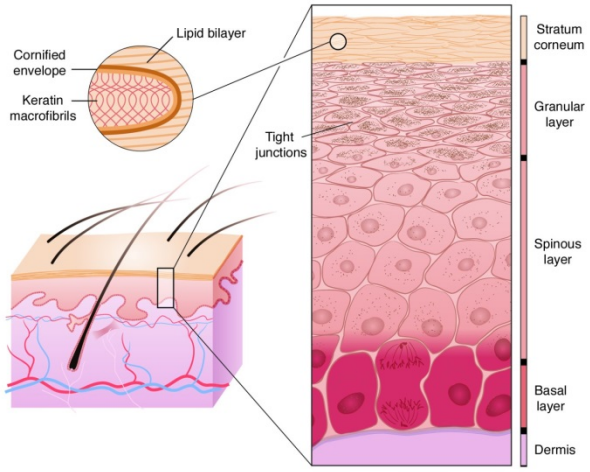

Figure 1.1 Structure of the Epidermis
The epidermis is formed of keratinocytes divided into four layers. Keratinocytes of the basal layer divide and as differentiation processes are initiated, move up through the epidermis. The final transition occurs at the interface of the granular layer and stratum corneum, where cellular organelles disintegrate, cellular contents are extruded into the extracellular space, and dehydrated keratin-rich corneocytes form. The Journal of Clinical Investigation by AMERICAN SOCIETY FOR CLINICAL INVESTIGATION.

The second layer of the epidermis is the stratum spinosum (SS), above the SB. In the SS, keratin intermediate filaments form bundles, some of which are connected to the desmosomes which anchor neighboring cells together [3]. These filament bundles give these cells a spiny appearance histologically, leading to the name of this epidermal layer. The keratinocytes differentiate further forming the stratum granulosum (SG). In this layer, organelles within the keratinocytes begin to disintegrate and lamellar bodies form, containing pro-barrier lipids and enzymes involved in lipid processing and desquamation. At the interface between the SG and the stratum corneum (SC), the contents of the lamellar bodies are extruded into the intercellular space, cellular organelles completely disintegrate, and viable keratinocytes transform into non-viable, keratin packed corneocytes.

As the cells transition from the SB to SS to SG, the cell shape evolves from columnar to cuboidal to squamous. Through this transition, cell volume doubles as the lateral projected area of the cells increases [4]. In the final transformation from SG to SC the cells become even more flattened and the projected area doubles as corneocytes mature and move through the SC [5]. In addition to keratin which provides structural integrity, corneocytes contain the protein filaggrin and its breakdown products which contribute to maintaining an appropriate hydration level in the SC [6, 7]. Several of these morphological changes may be monitored through in-vivo confocal microscopy, and will be investigated as part of this thesis.

The corneocytes in the SC are surrounded by lipids composed of primarily ceramides, free fatty acids, and cholesterol, exhibiting various levels of axial and lateral organization (Figure 1.2) [8].

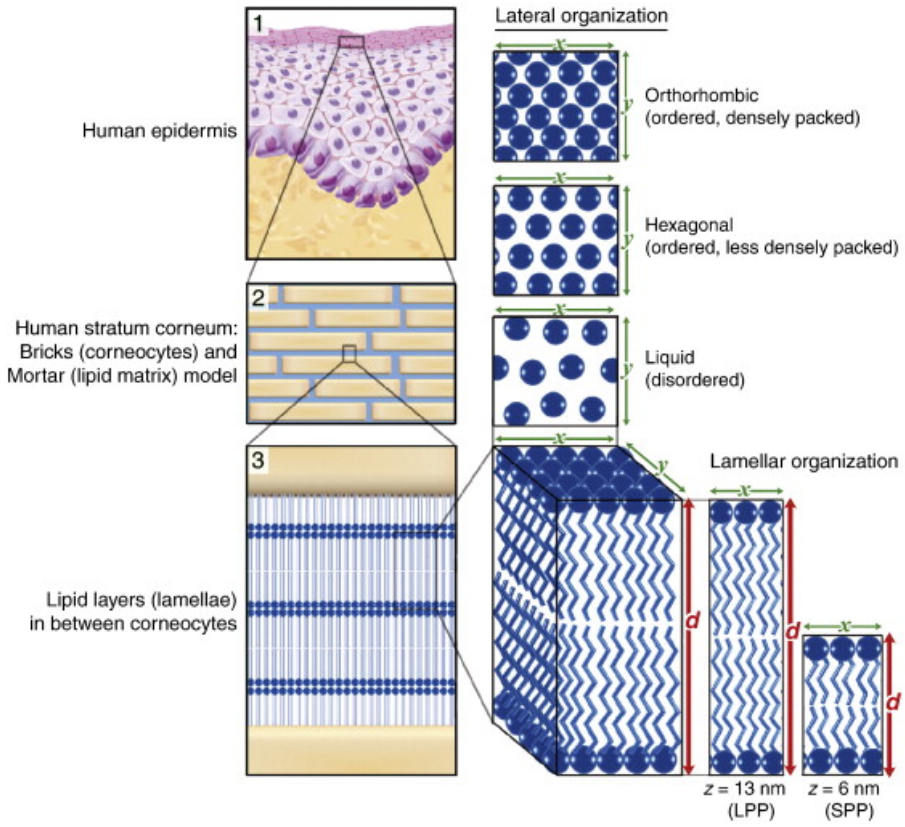

Figure 1.2 Lamellar Organization of Lipids in the Stratum Corneum
The axial lamellar organization and lateral packing of lipids in the stratum corneum impact barrier function. Reprinted from Biochimica et Biophysica Acta (BBA) – Molecular and Cell Biology of Lipids, 1841, J. van Smeden, M. Janssens, G. S. Gooris, J. A. Bouwstra, The important role of stratum corneum lipids for the cutaneous barrier function, 295-313, 2014 with permission from Elsevier [9].

The axial lamellar organization has been shown to comprise two distinct repeat distances on the order of 6 nm and 13 nm [9, 10]. Laterally, the lipids organize into primarily an orthorhombic and hexagonal crystal structure, with some fluid domains interspersed

within the organized domains [11, 12]. Both axial (presence or absence of long periodicity phase) and lateral (orthorhombic – hexagonal packing ratio) organization have been correlated to skin barrier function [13, 14]. Vibrational spectroscopy may be utilized to monitor changes in lipid packing and conformational order in-vivo, and these methods will be used in this thesis to investigate skin barrier function.

1.2 Skin Barrier Function

The complex ultrastructure previously described results in development of a highly efficient barrier. Contributors to the barrier function include elements of the viable layers (thickness of the viable epidermis, tight junctions between the keratinocytes) and to a large extent properties of the SC (thickness of the SC, lipid content and organization, corneocyte composition) [7, 15]. The maintenance and periodic renewal of the skin barrier is achieved by the highly coordinated processes of proliferation, differentiation, and desquamation.

The skin turnover rate may be defined as the time that a single keratinocyte takes from initial displacement from the basal layer to sloughing off at the surface of the SC. Rates of proliferation and desquamation both contribute to turnover rate: increasing proliferation with no change in desquamation initially results in shorter turnover rate due to cells traversing the epidermis faster, and increasing desquamation with no change in proliferation results in shorter turnover rate due to a smaller distance that the cells must traverse. In general, skin turnover rate and differentiation are inversely related. If the rate

of keratinocyte and corneocyte differentiation remains constant and the turnover rate becomes shorter, corneocytes at the surface of the skin do not have the time to completely differentiate.

Dysregulation of one or more of these processes is often observed in skin diseases and associated with reduced barrier function. Impaired desquamation is associated with ichthyosis as excessively dehydrated surface layers of corneocytes are not sloughed off, giving the appearance of dry, flaky skin [16]. Both psoriasis and atopic dermatitis are inflammatory disorders associated with altered hyperproliferation of the viable epidermis, but present with opposite extremes of dysregulated desquamation [2]. The pathophysiologies of diseases characterized by dysregulated epidermal differentiation are currently investigated through clinical assessment and invasive collection of skin biopsies. Advances in in-vivo measurement techniques which are able to be applied in a clinical setting, such as the optical imaging and spectroscopic methods investigated in this thesis, are necessary so that primary defects may be distinguished from secondary effects.

1.3 Measures of Skin Barrier Function

Epidermal differentiation status has been monitored by the hydrophobicity of corneocyte envelopes sampled from the surface of the SC, measurement of the fragility of surface corneocytes, levels of specific differentiation-associated structural proteins (involucrin, loricrin, keratins 1 and 10) and enzymes (transglutaminase, caspase-14) within the epidermis and SC, evaluation of changes in desmosomes through electron microscopy,

SC proliferation and turnover rate, and SC thickness [1, 7, 17, 18]. Typically, those techniques which provide the most detailed information (protein concentration, gene expression, morphology at the molecular level) are also the most invasive (i.e. require tissue collection through biopsy). Noninvasive techniques to study the skin are advantageous not only because obtaining subject consent is less of an obstacle than with invasive methods, but also because of the expanded range of experimental protocols feasible. For example, time course experiments where a particular skin site or lesion is monitored over a period of minutes to months, are possible because measurement is non-destructive. In addition, because the tissue under study remains in its native environment, assumptions regarding the generalizability of ex-vivo results to in vivo phenomena are not necessary.

Properties of the SC and epidermis which are easily measured noninvasively are transepidermal water loss (TEWL, water flux - property of entire SC), conductance (interrogation depth dependent on instrumental design), apparent concentration of chromophores (entire epidermis, superficial dermis), and macroscopic properties of the skin as documented through various imaging modalities (entire epidermis, superficial dermis) [19-22]. More recently, minimally invasive techniques which involve the collection of skin samples by adhesive tapes, cyanoacrylate, or scraping have been developed, however these techniques are typically limited by both collection and analytical protocols. Sampling is limited to the SC, and analytical protocols may be constrained by sample extraction techniques and interference of adhesives with analytical methods.

1.3.1 Microscopic Imaging of Skin

Recently, noninvasive optical techniques which enable collection of depth-resolved data in vivo have been developed. Ultrasound and optical coherence tomography (OCT) are two such techniques which can collect data to depths up to centimeters or hundreds of micrometers (μm) within tissue, respectively. Both ultrasound and OCT operate under the principle of collecting reflected/backscattered signal. Advanced high frequency ultrasound instruments are able to collect images of the skin with axial resolution on the order of 10 μm and lateral resolution on the order of 50-100 μm [23]. OCT utilizes near infrared illumination and depending on instrument configuration can deliver axial and lateral resolutions on the order of 10-15 μm [24, 25]. However, the currently available resolution of these techniques is not sufficient to accurately measure all of the morphological features of the epidermis evaluated as markers of skin barrier in this work [25]. The thickness of the SC (5-15 μm) and the size of individual keratinocytes within the various layers of the viable epidermis (5-10 μm in diameter) are key features which require lateral and axial resolution on the order of 5 μm or better for quantitative measurements.

Confocal microscopy measurement techniques offer enhanced image resolution to the cellular level, but are only able to collect data to depths of a few hundred μm. In skin, imaging is limited to the epidermis and upper dermis. Confocal microscopes designed for imaging skin in vivo operate in reflectance and/or fluorescence modes and enable the

collection of images at sequential depths within the skin, yielding morphological information about the skin site [26-30].

Measurement Technique	Sampling Region	Spatial Resolution	Limitations
Transepidermal Water Loss	Entire Epidermis	None	Non-specific measure of skin barrier
Multi-modal Digital Imaging	Entire Epidermis / Superficial Dermis	System dependent	Non-specific
Reflectance Spectroscopy	Entire Epidermis / Superficial Dermis	None	Measure of apparent concentration of skin chromophores
Collection of superficial corneocytes (tape stripping or scraping)	Stratum Corneum	No lateral resolution / limited axial resolution	Extraction methodologies limit analysis endpoints, Limited to upper SC
Ultrasound	Epidermis / Dermis / Subcutaneous layers	Lateral: 50-100 μm / Axial: 10 μm	Resolution limitations
Optical Coherence Tomography	Epidermis / Dermis	Lateral and axial: 10-15 μm	Resolution limitations
Confocal Microscopy	Epidermis / Upper Dermis	Lateral: 1 μm / Axial: 5 μm	Measurement depth limited to upper dermis
Vibrational Spectroscopy	Epidermis	System dependent	Molecular composition and structure

Table 1.1 Comparison of Skin Measurement Techniques

Reflectance confocal microscopy (RCM) images yield comparable information to hematoxylin and eosin stained histology slides [27]. Measurement of skin thickness with RCM has been validated through comparison of RCM measurements with measurements of histology sections from biopsy samples collected at the same site [31]. Cellular detail near the surface of the skin is best observed with blue light illumination due to better lateral resolution, but contrast deteriorates in images of the SS and SB due to increased scattering with shorter wavelength illumination, and therefore increased detection of

multiply scattered light. The DEJ and superficial dermis are best observed with red / near infrared wavelength illumination due to decreased scattering losses.

In dermatological fields, confocal microscopy has been most widely used for noninvasive detection of melanoma or to assist surgeons in mapping the edges of tumors in real time during excision [26, 32, 33]. It has also been used to characterize morphological aspects of various types of skin lesions and disease states [34-39], as well as to monitor penetration of exogenous molecules, such as highly scattering particulates (zinc oxide, titanium dioxide) and fluorescent dyes [29, 40]. Recently, confocal microscopy has been evaluated as a technique to demonstrate the effects of various treatments, including resolution of disease symptoms [41]. With few exceptions, methodologies for in-vivo skin assessment using confocal microscopy rely on qualitative grading of features in the images. While useful in assessing presence or absence of features relating to disease symptoms, qualitative grading is of limited utility when evaluating non-disease states as the differences in skin features are generally more subtle and occur on a spectrum rather than as a binary endpoint.

As the application of confocal microscopy to measure skin has expanded to non-disease states, efforts to quantify skin features from confocal images have focused on measurement of SC and epidermal thickness [5, 31, 42-44]. Currently layer thicknesses are calculated based on visual examination of image stacks. However efforts are underway to develop automated image analysis methods [45]. Additional morphological features observable in reflectance mode that are suitable for quantification are

keratinocyte projected area, amplitude of DEJ undulation, and scattering intensity profiles. Fluorescence mode confocal microscopy enables evaluation of barrier properties through measurement of dye penetration into the SC and epidermis. Reflectance mode and fluorescence mode confocal microscopy will be utilized in this thesis for measurement of skin barrier function through quantification of epidermal layer thickness, keratinocyte cell area, scattering intensity profiles, and fluorescent dye penetration.

1.3.2 Spectroscopy of Skin

In addition to microscopy techniques, non-invasive methods for evaluating composition and molecular organization of the skin have been developed based on spectroscopic methods traditionally used for chemical identification. Vibrational spectroscopy (Raman and Infrared (IR)) as applied to skin may be used to quantify many of the components which are important to the development of the skin barrier, such as the cross-linked protein corneocyte envelope, sebaceous and barrier lipids, keratins, natural moisturizing factor, and water [46-48]. Vibrational spectroscopy allows for changes in lipid and protein structure to be monitored due to the spectral changes with molecular environment [48]. Specifically, conformational order and lateral packing of SC lipids may be measured using infrared spectroscopy, and these endpoints may be probed in-vivo through application of Attenuated Total Reflectance – Fourier Transform Infrared (ATR-FTIR) spectroscopy [49, 50]. Quantification of spectral features related to SC lipid organization has been utilized extensively in in-vitro and ex-vivo experiments to demonstrate changes with SC lipid composition and effect of exogenous compounds [51-

53]. In addition, ATR-FTIR has been used to demonstrate correlation between measures of SC lipid organization to barrier function, and this methodology will be employed in this thesis to investigate the mechanism of barrier function disruption by a topically applied compound [13, 54, 55].

1.4 Novel Contributions Made in this Thesis

The overall function of the skin barrier is drawn from both morphological and compositional properties, and both aspects of skin barrier function may be dysregulated in cases of skin disease. In this work, we developed in vivo models for studying epidermal morphology and the molecular order of SC lipids non-invasively and we then integrated these methodologies with functional assessments of skin barrier to demonstrate the relationship of these features to skin barrier function.

We show an immediate change in skin morphology in the viable epidermis after a moderate barrier disruption limited to the SC, which has been previously unreported. We also show through measurements of the temporal response of both morphological and functional aspects of the skin barrier that the magnitude of the response to barrier disruption scales to the magnitude of the damage to the barrier. Finally, we link the molecular-scale organization of SC lipids to the barrier function of the skin measured by water loss and penetration of a marker dye. We elucidate the mechanism of barrier disruption through in-vitro experiments which show that the permeation enhancer oleic acid mixes with and fluidizes SC lipids which are confirmed through in-vivo experiments

showing disruption of the organization of endogenous SC lipids. Through this work, we establish structure-function relationships of the skin barrier, measureable through non-invasive methodologies, which may be leveraged for development of novel therapeutic approaches to treatment of skin disease as well as for improving diagnostic capabilities through understanding the mechanism and etiology of skin barrier disruption.

CHAPTER 2 Assessment of Reflectance Mode and Fluorescence Mode Confocal Microscopy for Measurement of Skin Barrier Function

2.1 Background and Objective

Technological advances in imaging and microscopy have expanded the possibilities for in-vivo measurements of skin. In-vivo confocal microscopy enables collection of depth-resolved images under the skin surface and has the potential to enable in-situ monitoring of alterations in skin barrier without the need for invasive procedures or introduction of histological artifacts. This measurement technique has been extensively applied to diagnosis of skin cancers and qualitative assessment of skin morphology in normal skin and disease states such as acne, atopic dermatitis, contact dermatitis, psoriasis, and vitiligo [32, 34-36, 38, 39, 56-59]. Development of quantitative methodologies first requires an assessment of the theoretical and in-use resolution of the available in-vivo confocal microscope and identification of the optimum instrumental parameters.

The objective of this chapter is to evaluate the suitability of the Vivascope 1500 trilaser confocal microscope (Caliber ID, Rochester NY) to quantify skin features of interest relevant to barrier function. Important parameters to be used to evaluate the instrument suitability are the resolution limits practically achieved when imaging skin and the maximum imaging depth. The microscope's resolution limits will be first theoretically calculated and these theoretical calculations will be compared to experimental results. Maximum imaging depth will be evaluated through in-vivo proof of concept experiments.

Confocal imaging is accomplished by placement of a pinhole before the detector in a conjugate plane to the object plane which eliminates out of focus signal and generates depth-resolved images (Figure 2.1). In confocal microscopes, the choice of pinhole size is a tradeoff between the light intensity reaching the detector and the resolution of the image produced. A very large pinhole negates the gains in resolution achieved through the confocal configuration; however a very small pinhole excludes the majority of light from reaching the detector. The optimal pinhole size is a function of imaging wavelength, and objective magnification and numerical aperture (NA).

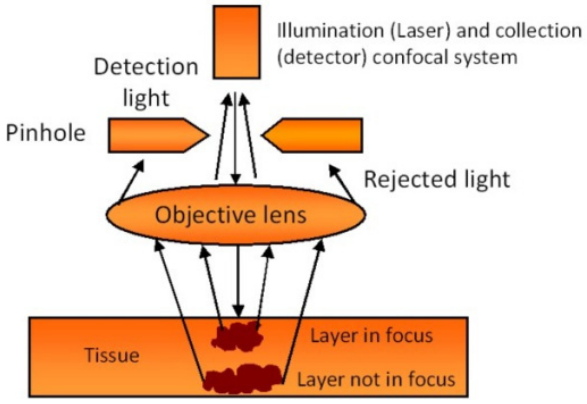

Figure 2.1 Schematic of Confocal Imaging
Insertion of a pinhole before the detector eliminates out of focus signal, enabling depth resolved imaging. Reproduced from [60] under the Creative Commons Attribution License (CC-BY-3.0)

Through the use of diffraction theory and application of appropriate approximations, the ideal resolution limits may be defined for a specific optical configuration. These resolution limits aid in optimization of the microscope hardware and software, and aid in identification of features observed in the images produced. Optical configurations may

be compared through evaluation of the point spread function (PSF). The PSF mathematically describes the degree of blurring which an optical system produces when imaging a point object, and is a measure of image resolution [61].

2.2 Theoretical Point Spread Functions of the Trilaser Confocal Microscope

The trilaser confocal microscope is equipped with three lasers of wavelengths 445 nm, 658 nm, and 785 nm. These wavelengths were chosen to enable imaging of fluorophores with specific excitation wavelengths. In addition, a range of wavelengths allows for the choice of greater resolution (shorter wavelength) versus greater imaging depth (longer wavelength) to be determined based on experimental design and the sample to be measured. The objective in use is a 40x, 0.9 NA water immersion objective.

MATLAB was used to calculate the lateral and axial PSFs of the trilaser confocal microscope for each laser wavelength as a function of various pinhole sizes (Figures 2.2, 2.3) as described in the literature using equations derived from first principles [61-63]. As there is no depth discrimination for planar objects in widefield microscopy, the increase in axial resolution realized by the confocal configuration is theoretically greater for planar sources than for point sources, and therefore the effect of pinhole size on axial resolution is more pronounced for planar sources. Therefore, a planar source was chosen for the axial PSF model to maximize the potential differences with pinhole size. Three pinhole sizes were modeled based on the pinhole sizes recommended for use by the manufacturer. The ideal case of the infinitely small pinhole (delta function) was also

calculated for comparison. Resolution limits were first calculated in normalized coordinates from the PSF and were then transformed to spatial coordinates (Tables 2.1, 2.2). The full width at half maximum (FWHM) of the PSF in spatial coordinates (x-FWHM , z-FWHM) was used to compare resolution limits across laser wavelength and pinhole size.

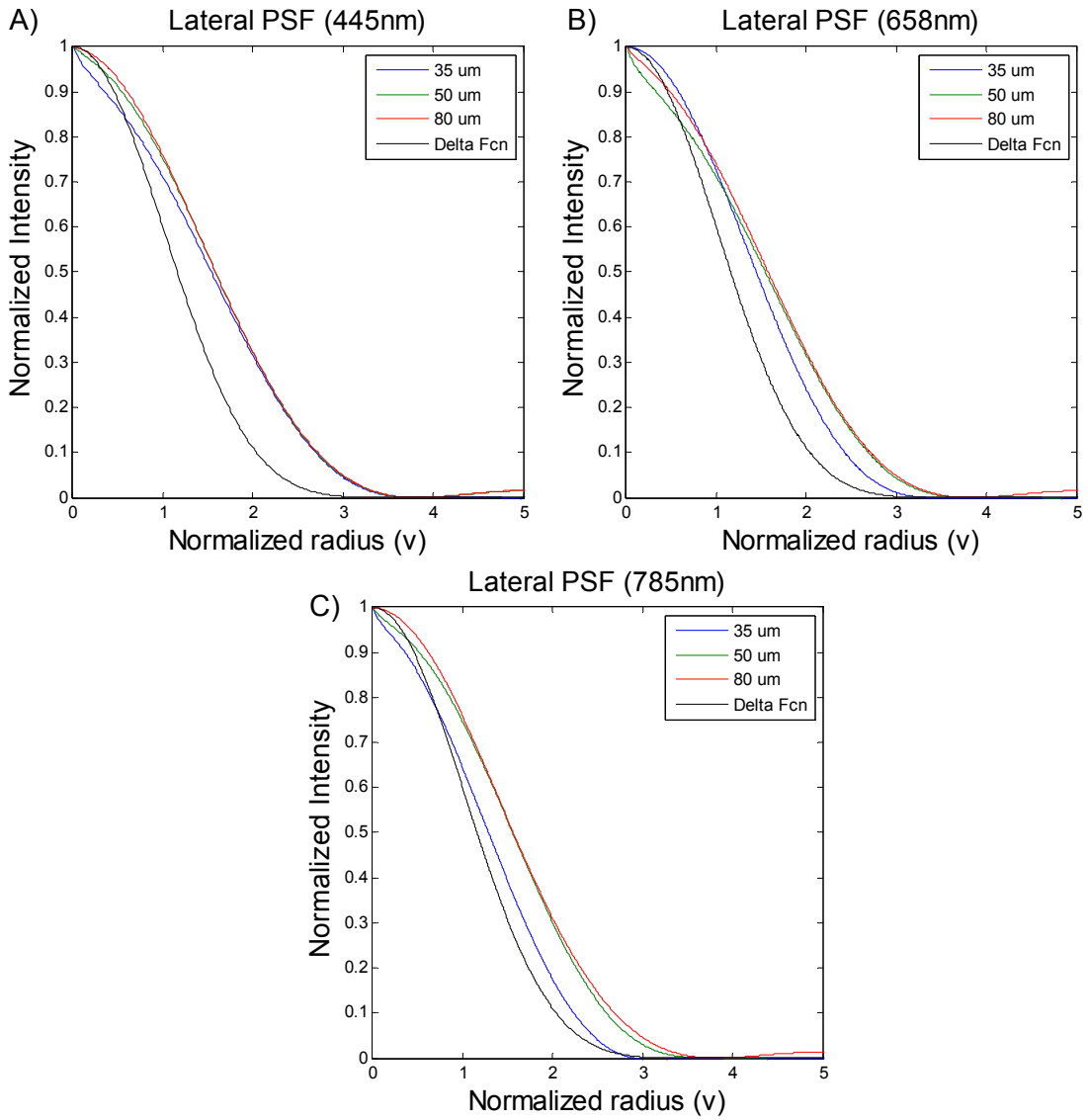

Figure 2.2 Evaluation of Theoretical Lateral Resolution of a Point Object in Reflectance Mode of the Confocal Microscope: Comparison Across Wavelengths and Pinhole Size.

2.2A: Lateral PSF calculated for a wavelength of 445 nm. 2.2B: Lateral PSF calculated for a wavelength of 658 nm. 2.2C: Lateral PSF calculated for a wavelength of 785 nm.

Lateral resolution degrades with increasing wavelength and with increasing pinhole size, although pinhole size does not have as great an effect at the 445 nm wavelength. Among all combinations of laser wavelength and pinhole size, the worst lateral resolution is theoretically 0.43 µm (785 nm laser, 80 µm pinhole).

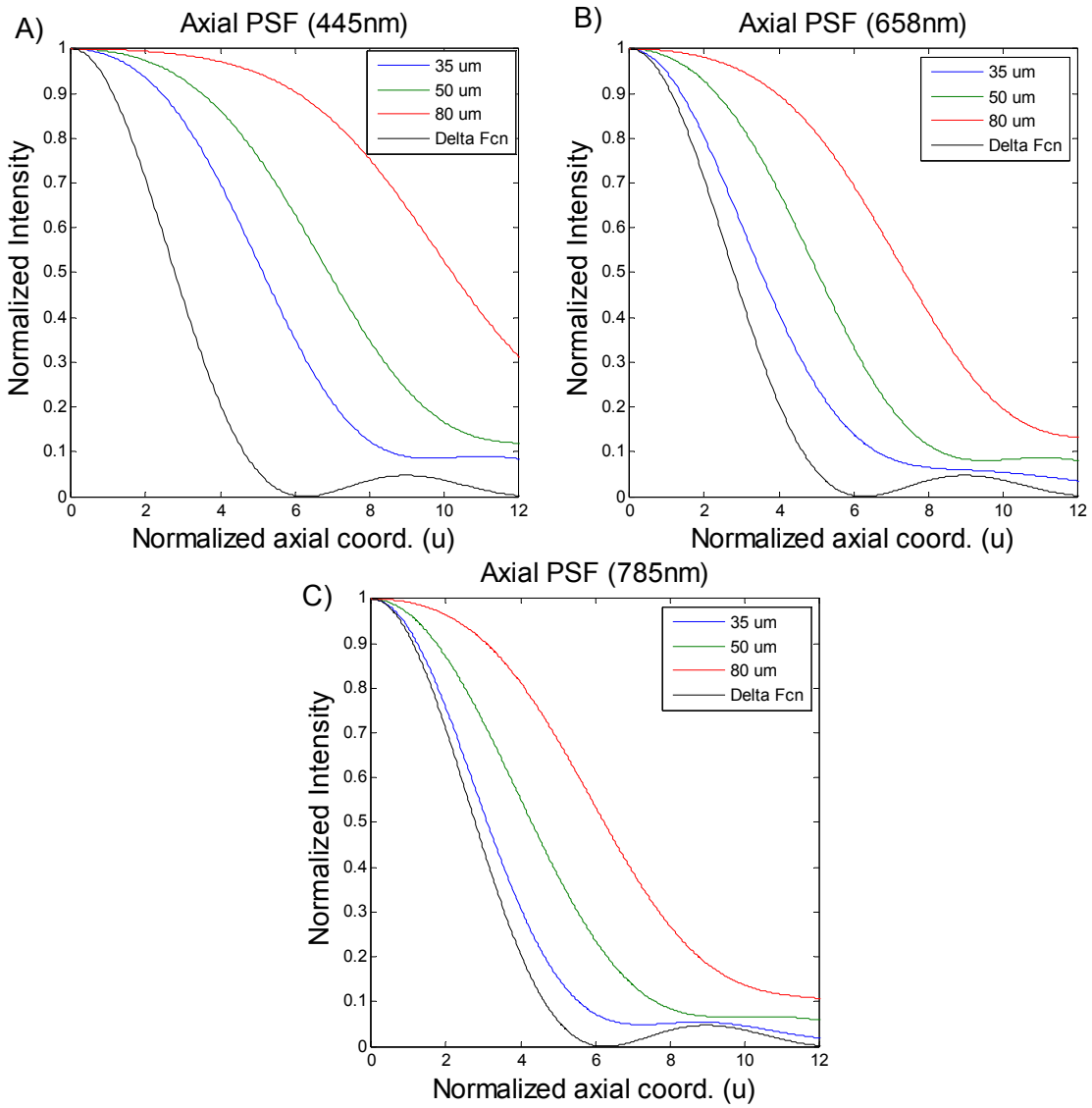

Figure 2.3 Evaluation of Theoretical Axial Resolution through a Planar object in Reflectance Mode of the Confocal microscope: Comparison Across Wavelengths and Pinhole Size.
2.3A: Axial PSF calculated for a wavelength of 445 nm. 2.3B: Axial PSF calculated for a wavelength of 658 nm. 2.3C: Axial PSF calculated for a wavelength of 785 nm.

Axial resolution is more dependent on pinhole size than lateral resolution at all wavelengths (Figure 2.3). In all laser/pinhole combinations considered, the worst axial resolution is theoretically 1.93 μm (785 nm laser, 80 μm pinhole).

Lateral Resolution: Point Object *($v_{1/2}$ / x-FWHM (um))*	445 nm	658 nm	785 nm
Delta Function	1.1603 / 0.1826	1.1603 / 0.2700	1.1603 / 0.3221
35 μm	1.5390 / 0.2422	1.4453 / 0.3364	1.2873 / 0.3574
50 μm	1.5860 / 0.2496	1.5463 / 0.3599	1.5568 / 0.4322
80 μm	1.5845 / 0.2494	1.5769 / 0.3670	1.5630 / 0.4339

Table 2.1 Comparison of Lateral PSF with Increasing Pinhole size and Laser Wavelength.

Axial Resolution: Plane Object *($u_{1/2}$ / z-FWHM (um))*	445 nm	658 nm	785 nm
Delta Function	2.7831 / 0.4866	2.7831 / 0.7196	2.7831 / 0.8586
35 μm	5.1474 / 0.9002	3.5229 / 0.9110	3.1098 / 0.9594
50μm	6.9159 / 1.2094	5.0365 / 1.3024	4.3012 / 1.3268
80 μm	10.2318 / 1.7892	7.3826 / 1.9090	6.2443 / 1.9262

Table 2.2 Comparison of Axial PSF with Increasing Pinhole Size and Laser Wavelength.

In the fluorescence case, the difference between the excitation and emission wavelengths (Stokes shift) has an effect on the PSF. However the Stokes shifts of the fluorophores commonly in use are sufficiently small to have a minimal impact in practice compared to the differences observed with changing the pinhole size or excitation wavelength [64].

2.3 Experimental Point Spread Functions of the Trilaser Confocal Microscope

Resolution limits of the trilaser confocal microscope were assessed through measurement of lateral and axial PSFs in reflectance mode with the 35 μm pinhole installed. Polystyrene beads (diameter = 0.771 μm) mounted in Aqua-Poly/Mount mounting media (Polysciences Inc., Warrington PA) on a glass slide were used for point source calculations. The beads were dispersed throughout the mounting media, and the bead/mounting media dispersion was spread on the glass slide to a thickness of a few millimeters. After drying for approximately 8 hours, the dispersion was covered with a glass coverslip and left to completely dry. This mounting procedure was found to more reliably produce usable samples with several individual beads suspended in mounting media and not in contact with either the slide or the coverslip.

Image stacks of the polystyrene bead standards were collected at the same location with the three lasers using the smallest available z-step (0.982 μm). The stacks were analyzed for both axial and lateral resolution (Figure 2.4). First, three beads were selected through visual examination of each image stack and the maximum reflectance intensity in a 20 by 20 pixel region of interest (ROI) surrounding each bead was recorded for each image. A Gaussian distribution was fit to the axial intensity profile.

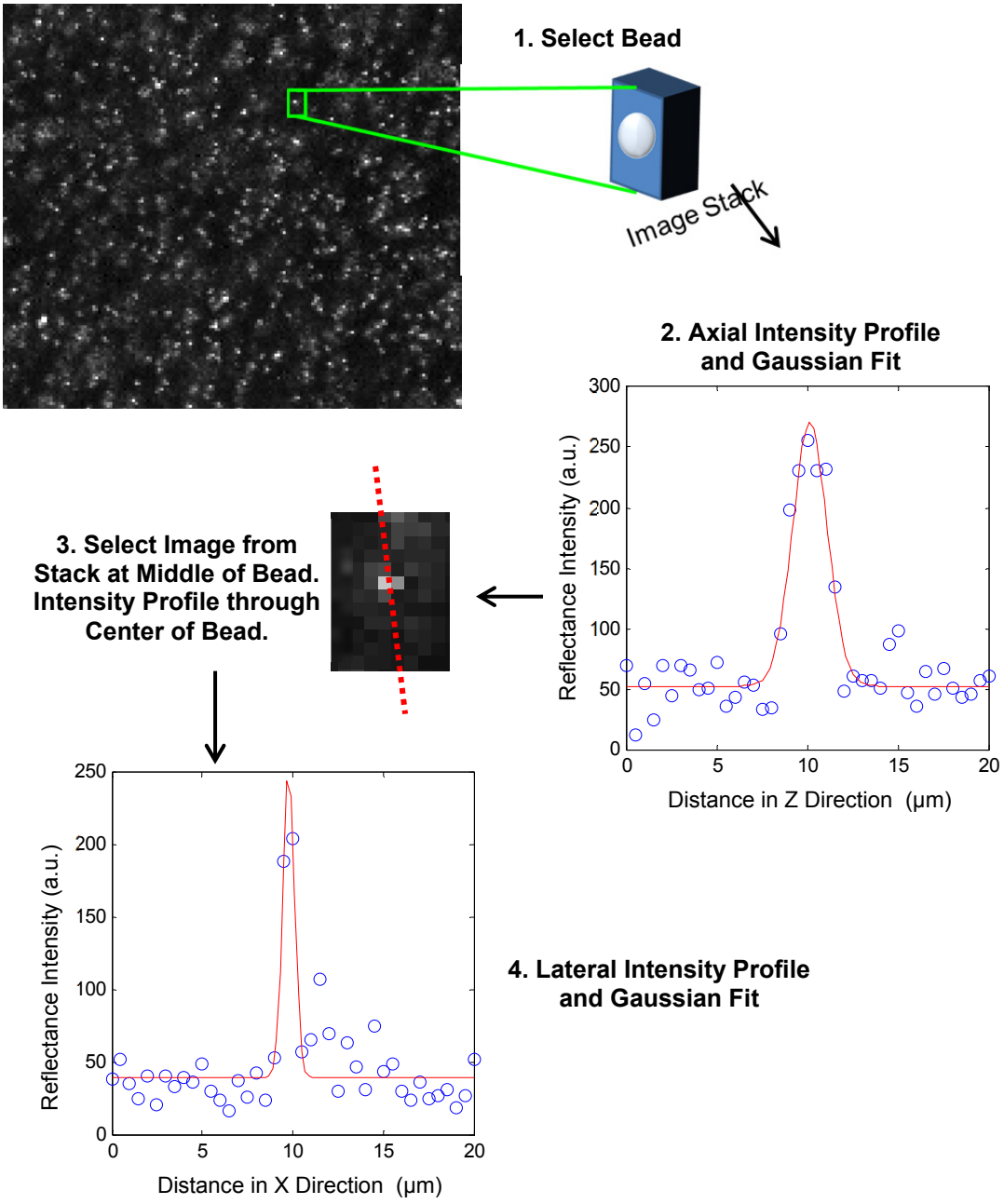

Figure 2.4 Analysis Method for Calculation of Point Source Lateral and Axial Resolution Limits.
Polystyrene beads (0.771 μm diameter) were mounted on a glass slide and imaged with all three wavelengths. Three beads were selected from each image stack (1), and axial intensity profiles (2) were generated from the maximum intensity in a 20x20 pixel region surrounding the bead. The image frame closest to the middle of the bead was determined from the axial intensity profile (3), and a lateral intensity profile was generated in the

designated frame for each bead (4). In the intensity profile graphs (2,4), blue circles represent reflectance intensity measured from the images, and the red lines indicate the Gaussian distributions fit to the intensity profiles. Resolution was calculated as the standard deviation of the Gaussian fit multiplied by 2.35.

For calculation of lateral resolution, the image closest to the middle of the bead was selected from within the stack by determining the z-position in the stack at which the maximum of the axial Gaussian distribution occurs. This image was then used to generate the lateral reflectance intensity profile along a line through the center of the bead. A Gaussian distribution was then fit to the lateral intensity profile.

Planar source resolution limits were assessed by measurement through the immersion gel – measurement window interface. The measurement window is essentially a thick plastic coverslip with adhesive around the edges of the top and bottom surface, used to adhere the window to the microscope housing and the skin. The refractive index mismatch between the immersion gel and the plastic window results in light scattering, and a measurable image, when the confocal plane passes through this interface. As the backscatter occurs at the interface the sample can be considered infinitely thin, similarly as a mirror imaged for these purposes would be considered infinitely thin. Image stacks of the immersion gel – measurement window interface were analyzed for axial resolution in a plane as follows: profiles of reflectance intensity at nine points in the image were extracted from each stack and fit to a Gaussian distribution (Figure 2.5).

For all lateral and axial intensity profiles collected as described in Figures 2.4-2.5, the FWHM of each profile was calculated as the standard deviation of the fitted Gaussian

multiplied by 2.35 [65]. Lateral and axial resolution limits were calculated by averaging the FWHM across all profiles by wavelength.

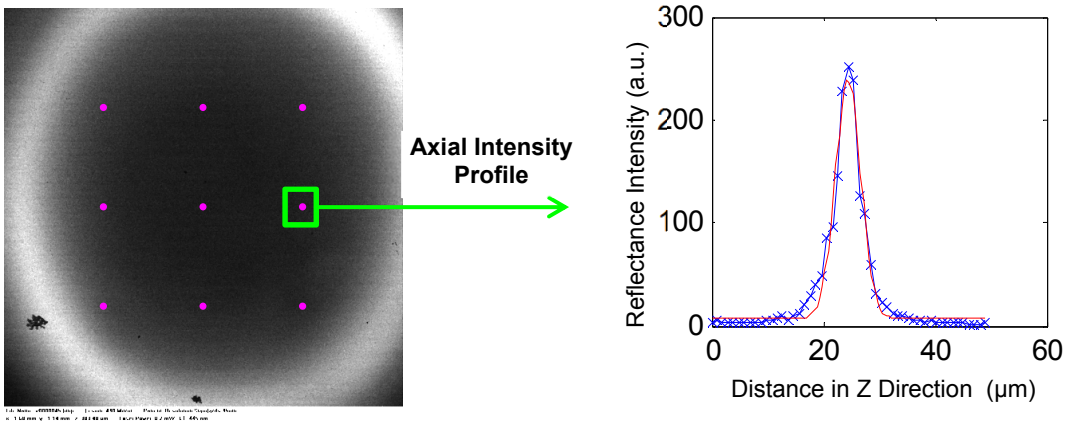

Figure 2.5 Analysis Method for Calculation of Planar Axial Resolution Limit. A representative image of the immersion gel – measurement window interface is shown. Nine points in each image stack were selected (pink dots in image), and reflectance intensity profiles were generated at each point (blue crosses on graph). Gaussian distributions (red line on graph) were fit to the axial intensity profiles, and resolution was calculated as the standard deviation of the Gaussian fit multiplied by 2.35.

Measured lateral resolution varied from 0.8 μm to 0.9 μm (Figure 2.6A), which is between two and four times the theoretical resolution of 0.24-0.43 μm. As predicted, lateral resolution is best at the short wavelength but does not approach the theoretical calculations. However, due to sampling constraints (pixel size is 0.5 μm x 0.5 μm), the expected lateral resolution would be at best approximately 1μm. These results indicate that the lateral resolution in the current image acquisition configuration is sampling-limited or limited due to the optical components used in the microscope.

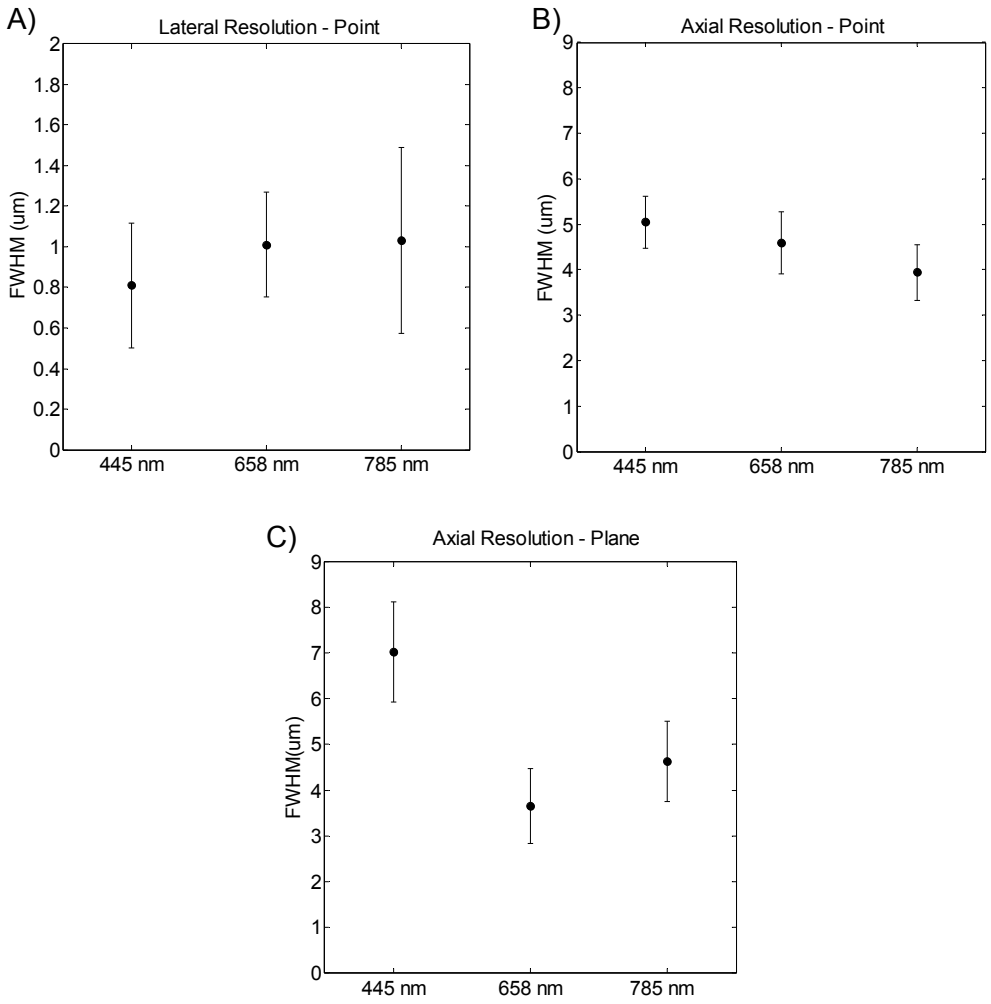

Figure 2.6 Measurement of Resolution Limits of the Trilaser Confocal Microscope. 2.6A: Measurement of lateral PSF through reflectance intensity profiles across polystyrene beads (0.771 um diameter). 2.6B: Measurement of axial PSF of a point object through reflectance intensity profiles across polystyrene beads (0.771 um diameter). 2.6C: Measurement of axial PSF of a plane object through reflectance intensity profiles across the measurement window-immersion gel interface.

Measurement of axial resolution with the polystyrene spheres indicates similar resolution limits across all three lasers, between 3 μm and 5 μm. Resolution limits calculated from images collected across the gel – window interface range from 4 μm to 7 μm, with the worst resolution limit measured at 445 nm. The measured axial resolution results do not

fit with the theoretical prediction of better resolution with use of a shorter wavelength laser and better resolution for a planar object versus a point object (Figures 2.6B, 2.6C) [61]. The inferior axial resolution measured from the planar sample compared to the polystyrene sphere sample may be due to the image acquisition process of the gel-window interface. Very low laser powers were necessary during acquisition of the gel-window interface images in order to avoid image saturation, which may affect the stability of the laser output. The departures from ideality observed in both lateral and axial resolution indicate that the in-use measurements are limited by practical aspects such as development of optics suitable for a range of wavelengths and maintaining alignment of all three lasers within the microscope.

Additional standards using different sizes of polystyrene beads were prepared and imaged but were not used for final calculations due to experimental complications. Although the theoretical lateral resolution ranges from 0.24-0.43 μm, polystyrene beads smaller than 0.771 μm were not visible during imaging. Additionally, the lateral sampling of 0.5 μm effectively limits the resolution in use to 1 μm.

2.4 Morphological and Functional Measurements of Skin Barrier with the Trilaser Confocal Microscope

The prior results indicate that the microscope is suitable for measuring certain morphological properties of the epidermis. There are morphological features of interest which contribute to the formation of the skin barrier at multiple length scales (nm, 1-10

μm, tens to hundreds of μm, mm to cm). Features on the nm length scale are below the resolution limits of the microscope. Features on the mm to cm length scale would be impractical to measure with the microscope as the field of view is 500 μm by 500 μm.

Features of the skin barrier suitable to measure with the confocal microscope include the thickness of each layer of the epidermis (stratum corneum (SC), stratum granulosum (SG), stratum spinosum (SS), stratum basale (SB)), the size of cells within the viable epidermis, the organization of cells within the viable epidermis, and the amplitude of the undulations of the dermal epidermal junction. Functional measurements of skin barrier integrity are also possible through measurement of fluorescent dye penetration into the skin. The lateral resolution of the microscope is sufficient to image corneocytes at the surface of the SC. However in reflectance mode there isn't sufficient contrast due to a relatively uniform refractive index across the surface of the SC. The axial resolution limits thickness measurements to epidermal layers, and is not sufficient to calculate thickness of individual cells.

Maximum imaging depth in reflectance mode has been well established in the literature [43, 66]. Depending on skin condition and body site being imaged, reflectance images with sufficient contrast and resolution may be collected to 100 to 300 μm into skin (generally into the papillary dermis). It has been qualitatively reported that image contrast degrades when imaging the lower epidermis and dermis using the blue laser [67]. Imaging depth in fluorescence mode has not been as widely studied, and the relevance of

literature results to the current studies is limited due to a wide range of fluorophores used and differing application and sample preparation protocols.

2.4.1 Feasibility of Quantifying Skin Barrier through Reflectance Mode and Fluorescence Mode Confocal Imaging: Proof of Concept Measurements

The trilaser confocal microscope can collect reflectance and fluorescence images at the same location through insertion of a filter bar with either a low-pass (reflectance) or a high-pass (fluorescence) filter in front of the detector. The microscope also allows for on-line switching between the three lasers, enabling direct comparison of the image quality as a function of wavelength. Fluorescein was chosen as the exogenous fluorophore for its spectral properties and extensive history of use in vivo [29, 68, 69]. The toxicity profile of fluorescein is well known due to the long history of use, and the dye's quantum yield is high enough to generate detectable fluorescence emission using the 445 nm laser for excitation.

To identify parameters of epidermal morphology relevant to skin barrier function and able to be quantified using the trilaser confocal microscope, proof of concept measurements were collected on two test sites on the upper inner arm in one subject (25 year old Caucasian female). One site was treated twice daily with an 8% glycolic acid (GA) lotion and a placebo lotion was applied to an adjacent site for four weeks. GA is known to induce epidermal desquamation and proliferation [70-72]. In both the GA treated site and the placebo treated site, two sub-sites were measured: one sub-site was measured in reflectance mode only with all three lasers, and the other sub-site patched for

one hour with 0.15% sodium fluorescein in deionized water under a Hill Top Chamber (Hilltop Research, Miamiville OH) was measured in reflectance and fluorescence mode using the 445 nm laser.

2.4.2 Comparison of Image Contrast by Wavelength in Reflectance Mode

To quantitatively compare image quality across the three lasers in reflectance mode, a region of interest (ROI) was selected across three image stacks collected with the three different lasers at the same location. Distribution parameters of the reflectance intensity in the ROI were calculated in an image frame within the SC, approximately 10 μm into the skin, and an image frame within the dermis, approximately 70 μm into the skin (Table 2.3).

The standard deviation of the intensity distribution was used to compare contrast within the images as typical measures of contrast comparing maximum and minimum signal cannot be applied to these images. The instrument software automatically adjusts the laser power for maximum signal without excessive image saturation by increasing the power, up to the maximum power allowed, until a set number of pixels are saturated. Therefore, the maximum intensity of the majority of images collected with this microscope will be 255. The maximum intensity of the image is only less than 255 when the laser power reaches the defined threshold and cannot increase further. When comparing images collected with the same laser, the power adjustment can be accounted for by normalizing the intensity by the power. However, laser power cannot be used to

normalize images across wavelength due to differences in maximum power allowed for each laser and differences in power scales reflective of the inherent differences in energetic and scattering properties with wavelength.

	Reflectance Intensity at 9.82 um in skin				Reflectance Intensity at 68.74 um in skin			
	Min.	**Max.**	**Mean**	**Std. Dev.**	**Min.**	**Max.**	**Mean**	**Std. Dev.**
445 nm	1	255	75.249	28.592	7	169	64.53	17.504
658 nm	0	255	98.257	46.236	3	255	82.539	34.383
785 nm	0	255	78.998	44.362	0	255	68.112	36.008

Table 2.3 Image Contrast by Wavelength in the Stratum Corneum and the Dermis

Image quality in the dermis is compromised when imaging with the 445 nm laser, as shown by the reduced standard deviation of the intensity distribution (17.5 compared to 34.4 / 36.0 for the 658 nm and 785 nm lasers, respectively). The reduced range of pixel intensity observed indicates that scattering losses have reduced the signal output even with the laser power at the maximum level. The reduced standard deviation also indicates a reduction in image contrast. Contrast in the images collected with the 658 nm laser and the 785 nm laser are comparable.

2.4.3 Skin Barrier Endpoints Measureable in Reflectance and Fluorescence Mode

Image stacks were visually graded for thickness of the SC (SCT) and thickness of the viable epidermis (VET). Cell outlines in the SG were manually traced and cell area was calculated in Fiji [73, 74]. SCT was reduced in the GA treated site compared to the placebo treated site, and granular cells were smaller in the GA treated site compared to

the placebo treated site (Table 3, Figures 2.7A, 2.7B). Both observations of reduced SCT and smaller keratinocytes are consistent with the known effects of GA on induction of desquamation and proliferation.

	Stratum Corneum Thickness (um)	Thickness of Viable Epidermis (um)	Granular Cell Size (um^2)
Glycolic Acid	2.21 ± 0.49 *	48.1 ±3.8	460 ± 94.8 *
Placebo	5.16 ± 0.49	43.5 ±1.7	748 ± 108

Table 2.4 Proof of Concept of Measurement of Epidermal Morphology
Morphological differences in sites treated with either an 8% glycolic acid (GA) lotion or a placebo lotion twice a day for four weeks. Data is presented as averages ± standard deviations. Statistically significant differences between the GA and placebo sites are denoted by an asterisk in the GA row. ($p<0.05$, unpaired students t-test).

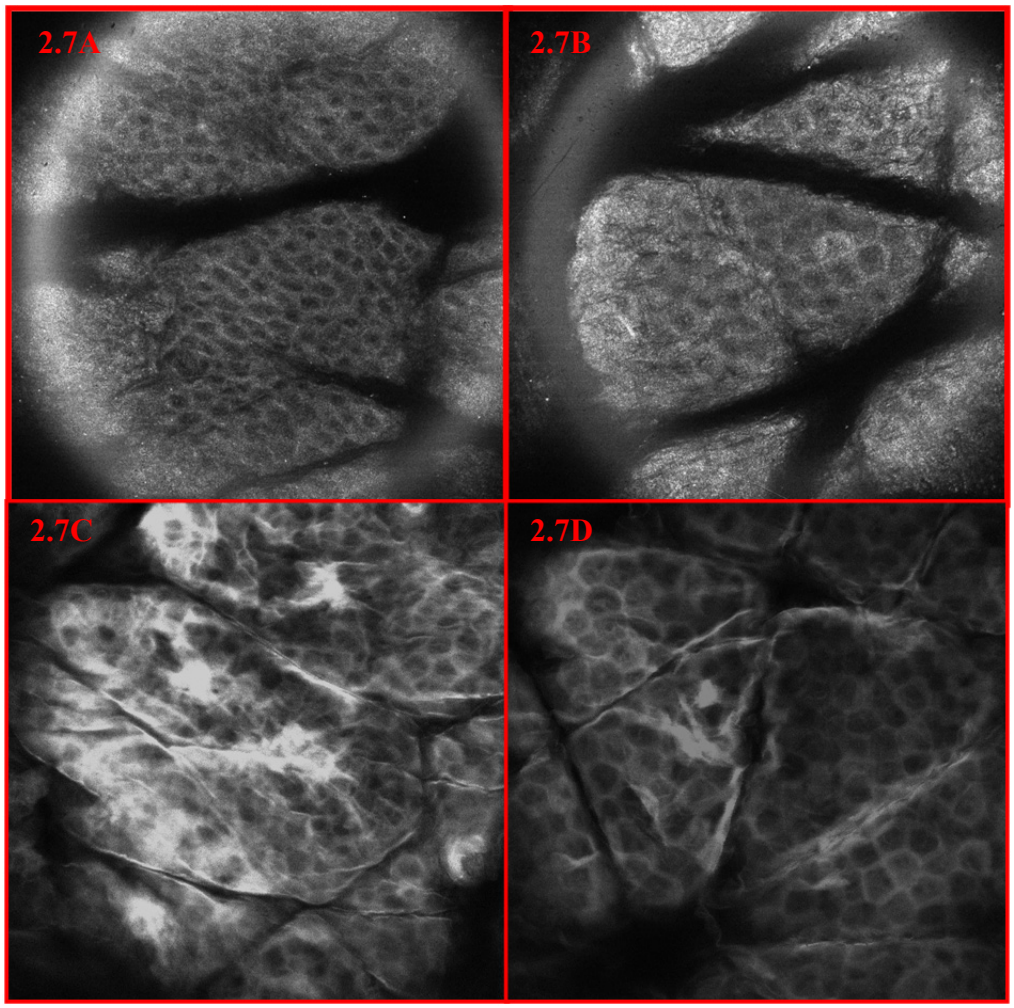

Figure 2.7 Reflectance Mode and Fluorescence Mode Images May be Used to Quantify Skin Barrier Properties
Proof of Concept experiment to establish epidermal morphology parameters of interest and to develop the Fluorescent Dye Penetration method for evaluation of skin barrier function. 2.7A Reflectance image in the granular layer of a skin site treated for 4 weeks with a 8% glycolic acid formulation. 2.7B Reflectance image in the granular layer of a skin site treated for 4 weeks with a placebo formulation. 2.7C Fluorescence image in the granular layer of a skin site treated for 4 weeks with a 8% glycolic acid formulation and patched for one hour with a 0.15% solution of fluorescein in deionized water. 2.7D Fluorescence image in the granular layer of a skin site treated for 4 weeks with a placebo formulation and patched for one hour with a 0.15% solution of fluorescein in deionized water.

Sodium fluorescein highlights corneocytes within the SC, and penetrates around the cells in the viable epidermis (Figures 2.7C, 2.7D). Fluorescence images were brighter in the GA treated site (Figures 2.7C, 2.7D), indicating increased fluorescein partitioning and penetration into the skin. Fluorescein penetration was quantified by calculation of average fluorescence intensity in a selected ROI in each image, normalized by the acquisition laser power (Figure 2.8).

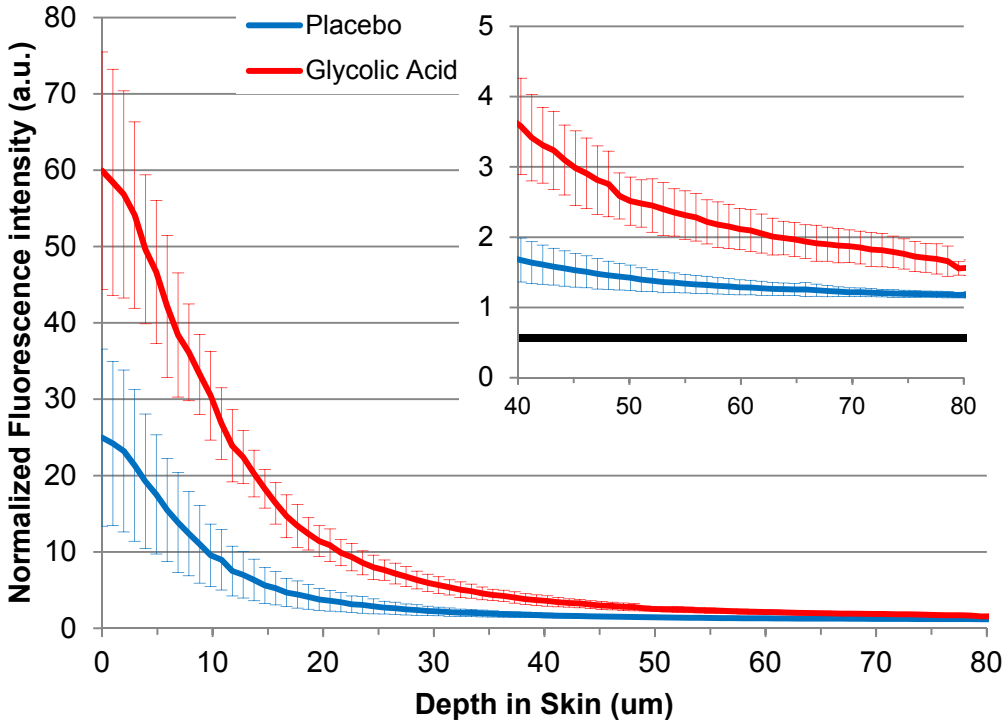

Figure 2.8 Fluorescein Penetration into Skin Measured through Fluorescence Intensity Profiles
Normalized fluorescence intensity profiles measured from the glycolic acid (GA) treated site and placebo treated site. Fluorescence intensity is higher in the GA treated site both at the surface of the SC and in the viable epidermis. Inset shows normalized fluorescence intensity profiles between 40-80 μm on a magnified scale. Fluorescence intensity remains elevated in the GA treated site up to 80 μm, and fluorescence intensity is elevated versus background levels (black line, normalized fluorescence intensity ~0.5-0.6) in both GA and placebo treated sites.

Average fluorescence intensity profiles as a function of depth were calculated by averaging over intensity profiles of all ROI's in all image stacks. The fluorescence intensity profile was higher in the GA treated site than the placebo treated site both at the surface of the skin and throughout the epidermis (Figure 2.8).

Fluorescence images of skin without applied fluorescein were collected to calculate background intensity, and the average normalized background intensity was between 0.5-0.6. Normalized fluorescence intensity remained elevated compared to background levels in both the GA and placebo treated sites for up to 80 μm into the skin. Additionally, normalized fluorescence intensity in the GA treated site was statistically higher than in the placebo treated site for up to 80 μm (t-test, $p<0.05$). These results indicate that the dye patching method may be used as an in-vivo functional assay to differentiate treatment effects on skin barrier integrity.

2.5 Conclusion

The practically achievable resolution limits of the trilaser confocal microscope do not approach theoretical values. Additionally, the experimentally determined resolution

limits do not exhibit the theoretically expected wavelength dependence, likely due to the abberations from the design and optical constraints of inclusion of three lasers into one optical train packaged in a portable device suitable for measurements in-vivo. Because the resolution limits measured in this chapter were similar between the three wavelengths, the choice of laser for use in clinical studies may be governed by the particular experimental protocol. For example, evaluation of fluorescence with sodium fluorescein necessitated the use of the 445 nm laser whereas any of the three lasers may be used in experiments with reflectance mode measurements only. Protocols evaluating properties of the viable epidermis should utilize the 658 nm or 785 nm lasers due to significant degradation of image contrast with depth when using the 445 nm laser.

In summary, the work presented in this chapter demonstrates that the resolution limits and imaging depth achievable with the trilaser confocal microscope are suitable for the measurement of certain parameters of epidermal morphology relating to skin barrier function. These parameters include thickness of the stratum corneum and viable epidermis, size of cells in the stratum granulosum and stratum spinosum, and dye penetration, and they will be used to quantify the functional integrity of the skin barrier in the work presented in this thesis.

CHAPTER 3 Noninvasive Measures of Epidermal Morphology Correlate with Functional Assessment of Skin Barrier Repair Dynamics

3.1 Abstract

Development of non-invasive methodologies for measurement of skin barrier function has long been a focus of dermatological research. While traditional in-vivo measures of skin barrier focus on the water permeability barrier (transepidermal water loss – TEWL), technological advances in instrumentation have enabled more specific measurement of the skin morphological and compositional parameters that contribute to the overall quality of the skin barrier. In order to evaluate whether noninvasive assessments of epidermal morphology could be correlated to skin barrier function in vivo, we utilized a tape stripping protocol to compromise skin barrier integrity and followed the recovery of the skin barrier through TEWL and reflectance confocal microscopy (RCM) imaging. 19 subjects were enrolled in a one week clinical study in Skillman, NJ. Two sites on the upper inner arm were tape stripped until TEWL was between three and four times the baseline value. TEWL and cross-polarized digital imaging measurements were collected at baseline, immediately after tape stripping, and 24 hours, 48 hours, 72 hours, and one week post-tape stripping. RCM imaging was performed on a non-tape stripped control site and test sites immediately after tape stripping, and 24 hours, 48 hours, 72 hours, and one week post-tape stripping. Petrolatum was applied to one test site twice daily, however the treatment did not impact any of the measures of skin barrier recovery in this model. Morphological changes were observed in the viable epidermis immediately after tape stripping. TEWL and stratum corneum thickness, measured from RCM images,

were observed to recovered in a linear manner over one week. Through integration of morphological and functional assessments of skin barrier condition, non-invasive measures may be used to monitor properties of biological processes within the skin.

3.2 Background and Objective

The skin provides a physical barrier between the body and the external environment, and morphological parameters such as thickness of the layers of the skin and size of cells may be used to monitor the function of this physical barrier [75]. Dynamic measures of barrier disruption and recovery enable evaluation of the contribution of these features to the overall function of the skin barrier as well as provide insight into the biological processes at work to maintain barrier function homeostasis.

When the skin barrier is compromised, permeability of the skin increases to both the inward permeation of exogenous agents and to the outward flux of water. Recovery processes initiated after barrier disruption include both immediate responses aimed at reducing water loss and re-establishing a barrier to external irritants, as well as mid to long term responses which reinforce the skin barrier to protect from future insults. One immediate response to barrier disruption is degranulation of lamellar bodies from cells in the stratum granulosum (SG) to the SG / stratum corneum (SC) interface, which occurs on the order of minutes after barrier disruption [76]. Lamellar bodies contain precursors of the barrier lipids of the SC, and extrusion of these contents provides immediate additional hydrophobic material to strengthen the permeability barrier.

Disruption of the skin barrier also induces a proliferative response which has been documented across a broad range of mechanisms of barrier disruption: physical removal of the SC through tape stripping, application of chemical irritants such as sodium lauryl sulfate, and exposure to ultraviolet radiation [42, 77-79]. The proliferative response increases cell number within the viable epidermis, thus enhancing the barrier to future insults. For the greatest impact on barrier function, proliferation must be accompanied by differentiation of the newly formed keratinocytes to increase the content and thickness of the SC, from which the majority of the barrier function of the skin is derived [80].

Current methodologies to measure disruption of barrier properties and their recovery involve invasive measures to evaluate changes in gene and protein expression, lipid content, and ion gradients as well as the noninvasive measurement of the permeability barrier through transepidermal water loss (TEWL). Additional non-invasive measures include monitoring of stratum corneum thickness (SCT) and changes in the viable epidermis through reflectance confocal microscopy (RCM) and fluorescence spectroscopy [31, 42].

Tape stripping is a well-known method of compromising the skin barrier [81]. Efforts have been made to standardize the tape stripping process, and specialized adhesive tapes and pressure applicators have been developed for this purpose. However, the extent of barrier damage caused by the removal of each tape is inherently variable due to the surface properties of the skin including presence of flakes, lipids, and hydration state. In

addition, thickness of the SC and basal levels of transepidermal water loss (TEWL), a standard parameter used to quantify skin barrier function, are subject to interpersonal variations [82]. To address these issues, we standardized the tape stripping protocol by setting a relative target of a three times increase in TEWL over baseline, similar to the levels of TEWL increase observed in atopic dermatitis, psoriasis, and diaper dermatitis [83-85]. Therefore, the number of tape strips varied among subjects and between the different test sites within a subject based on the baseline TEWL level and amount of material removed by each tape. The restoration of barrier function was monitored as percent recovery to baseline values.

Epidermal repair processes have been widely studied in vitro, in animal models and to a lesser extent in humans [86-88]. Several studies have investigated repair after significant barrier disruption or injury, including removal of the entire SC or epidermis [42, 79, 89-92]. In one such study, Bargo et al. utilized RCM and TEWL measurements to document barrier repair after removal of the full SC through tape stripping, and found that SC thickness increased linearly after SC removal while TEWL decreased in a biphasic manner over the course of 10 days [42]. The present study builds on this prior work through utilization of a moderate barrier disruption as well as the addition of quantitative assessment of erythema.

RCM has also been used in observational studies of skin disease to probe skin barrier dysfunction. Others have compared the use of confocal microscopy as a measure of epidermal morphology to the standard functional assay of skin barrier, TEWL, in dry and

atopic skin states [41, 93]. In these studies, epidermal morphology was qualitatively compared across subjects and treatments by grading the appearance of glyphic structures, dryness of the stratum corneum, and the pattern of keratinocyte arrangement in the stratum spinosum (SS) [41, 93].

The purpose of the work presented in this chapter was to assess the relationship between epidermal morphology and skin barrier function to further understand the kinetics of barrier repair and regeneration processes. In order to probe the epidermal structure-function relationship in a dynamic fashion, a tape stripping protocol was utilized to disrupt both epidermal structure and barrier function. We utilized RCM imaging in conjunction with measurement of TEWL and erythema to investigate the changes in skin barrier morphology and function following a moderate disruption. We also evaluated the impact of treatment with a common topical skin protectant, but did not observe any differential effects due to treatment. We found that in addition to the expected increase in erythema, immediate changes in the viable epidermis were evident after tape stripping. Both the functional assessment of skin barrier (TEWL) and the most closely related morphological parameter (SC Thickness) recovered in a linear manner over one week.

3.3 Materials and Methods

3.3.1 Clinical Protocol

24 healthy Caucasian subjects with no history of skin disease were enrolled in a one week study in Skillman, NJ. The study protocol was approved by the Allendale Investigational

Review Board (Old Lyme, CT) and conducted in accordance with the ethical principles of the Declaration of Helsinki. Written informed consent was obtained from all participants prior to enrollment. After 30 minutes acclimatization to the study room environment, two 1 in by 1 in sites were marked on the upper inner arm, and TEWL (Evaporimeter, cyberDERM, Bromall PA) measurements were performed. The Evaporimeter utilizes an open cylindrical chamber which is placed perpendicular to the skin surface. The chamber has two temperature / relative humidity sensors set at fixed distances to the skin surface. The vapor pressure is calculated at each sensor location, and Nilsson's Vapor Pressure Gradient Estimation Method is used to calculate TEWL [94]. Each site was tape stripped using the methodology described below until the TEWL value was between three and four times the baseline TEWL value.

Standardized adhesive tapes (D-Squame D100 Standard Sampling Discs, Cuderm Corporation, Dallas TX) were placed on each measurement site with forceps, pressed to the skin using a standardized plunger (D-Squame D500 Pressure Instrument, Cuderm Corporation, Dallas TX) and left for one minute. After one minute, the tapes were gently removed with forceps, and another adhesive tape was applied to the site following the same procedure. The direction of removal of each tape was rotated 90° from the previous tape direction to ensure even stripping over the measurement site. To reach three times baseline TEWL values, a set of five tape strippings was performed as described and TEWL was measured after a five minute re-acclimatization period. After the first set of five tape strippings, additional strippings were performed singly or in sets of five as determined by study staff evaluation.

TEWL and cross polarized images (custom built digital imaging station) were collected at baseline, immediately after tape stripping, 24 hours, 48 hours, 72 hours, and 7 days. In a subset of subjects (n=8), RCM image stacks were collected at all timepoints except baseline. Immediately after tape stripping, RCM image stacks were collected on an adjacent control site. Two or three image stacks were collected at each test site with a Vivascope 1500 (Caliber ID, Rochester NY) outfitted with a 785 nm laser source. Image stacks consisted of 100 images (500 μm x 500 μm) collected at 1.43 μm z-step size.

Subjects applied ¼ fingertip unit (approximately $^{1}/_{8}$ g) of white petrolatum to one site twice daily and the other site served as an untreated control. At the end of the first visit after the post-tape stripping skin measurements, study staff demonstrated the proper dosing and supervised the subjects' first product application. On measurement days, the subjects were instructed to not apply the product in the morning, and to perform the first product application of that day after the study measurements. To reduce the potential for hyperpigmentation, subjects were instructed to wear long sleeve or elbow length shirts and avoid direct sun exposure on the upper inner arms for the duration of the study.

3.2.2 Analysis of RCM image stacks

SC thickness (SCT) and thickness of the viable epidermis (VET) were calculated through visual inspection of image stacks acquired in reflectance mode (Figure 3.1). The surface of the SC was identified as the image frame below the window-skin interface (Figure

3.2A**)**. Due to field curvature and the uneven topography of the skin surface, the surface of the SC appears in different frames for different regions of the image. For standardization of analysis, a region of interest (ROI) near the center of the image and excluding glyphic structures was identified for each image stack.

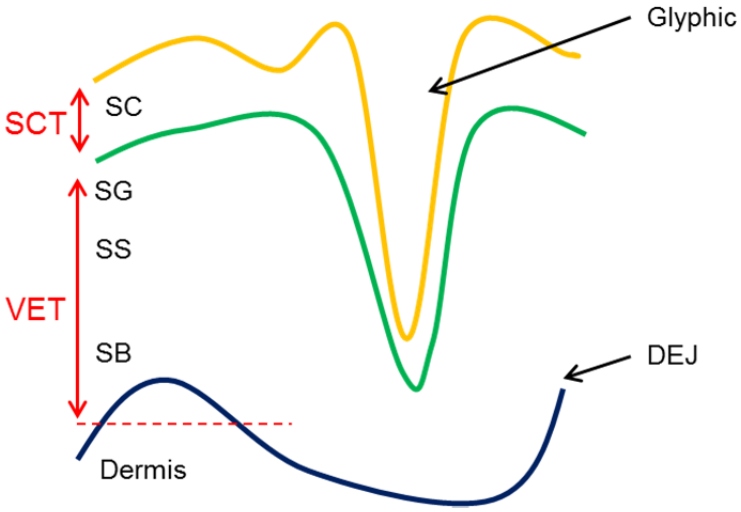

Figure 3.1 Measurement of Stratum Corneum Thickness and Thickness of the Viable Epidermis
Stratum corneum thickness (SCT) was measured as the distance from the top of the stratum corneum (SC) to the top of the stratum granulosum (SG). Thickness of the viable epidermis (VET) included the SG, stratum spinosum (SS), and stratum basale (SB) layers, and was measured as the distance from the top of the SG to the midpoint of the dermal-epidermal junction (DEJ).

The image frame containing the top of the SC within the designated ROI was noted (Figure 3.2A). The top of the stratum granulosum (SG) was identified as the first image frame where distinct, approximately circular, cellular outlines were observed in the ROI (Figure 3.2B). SCT was defined as the difference in depth of the top of the SC and the top of the SG.

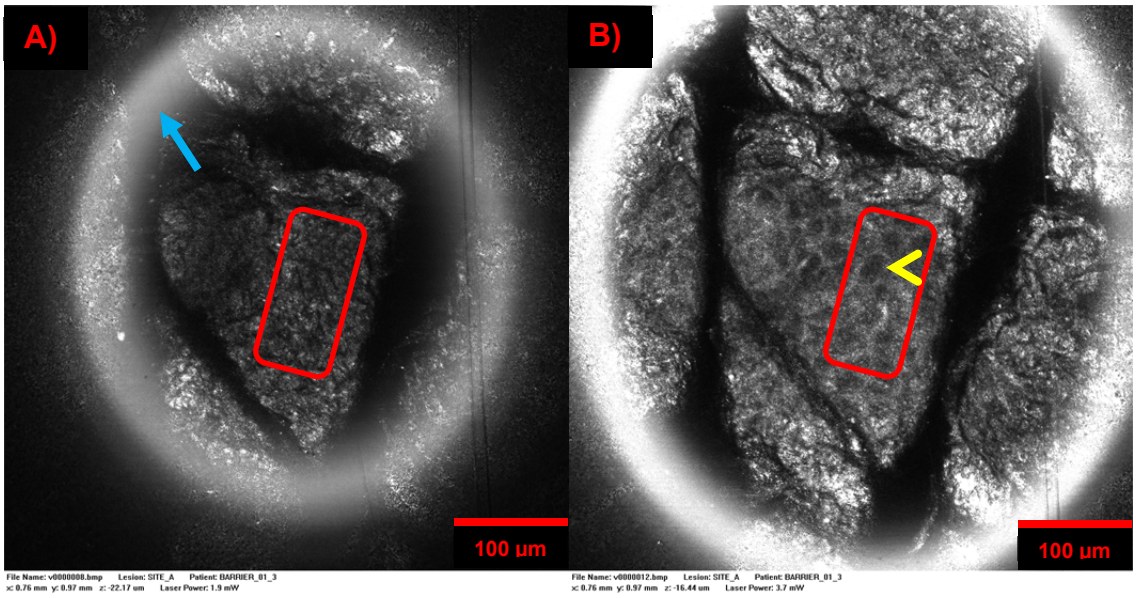

Figure 3.2 RCM Features Utilized to Determine SCT.
3.1A: The window-skin interface (blue arrow) is identified by a highly scattering ring which steadily expands through 3-5 image slices. For each image stack, an ROI (red outline) was identified near the center of the image and excluding glyphic structures. The top of the SC within the ROI was set as the image frame below the window-skin interface within the image stack ROI. 3.1B: The top of the SG within the measurement ROI was identified as the first image frame where distinct, approximately circular cellular outlines were observed (yellow arrowhead). Scale bar = 100 µm.

VET was measured as the depth between the top of the SG and the middle of the dermal epidermal junction (DEJ) within the ROI. In pigmented subjects, the stratum basale (SB) is indicated by brightly scattering melanosome-laden keratinocytes generally clustered around the top of the dermal papillae. In lightly pigmented subjects, the SB / DEJ is indicated by the disappearance of cellular structures. Within the ROI, the top of the DEJ was defined as the first image frame where cellular outlines disappear (Figure 3.3A,C). The bottom of the DEJ was defined as the image frame immediately below the last image frame where cellular outlines are visible within the ROI (Figure 3.3B,D). For the

purposes of VET calculation, the middle of the DEJ was defined as the frame halfway between the top of the DEJ and the bottom of the DEJ within the ROI.

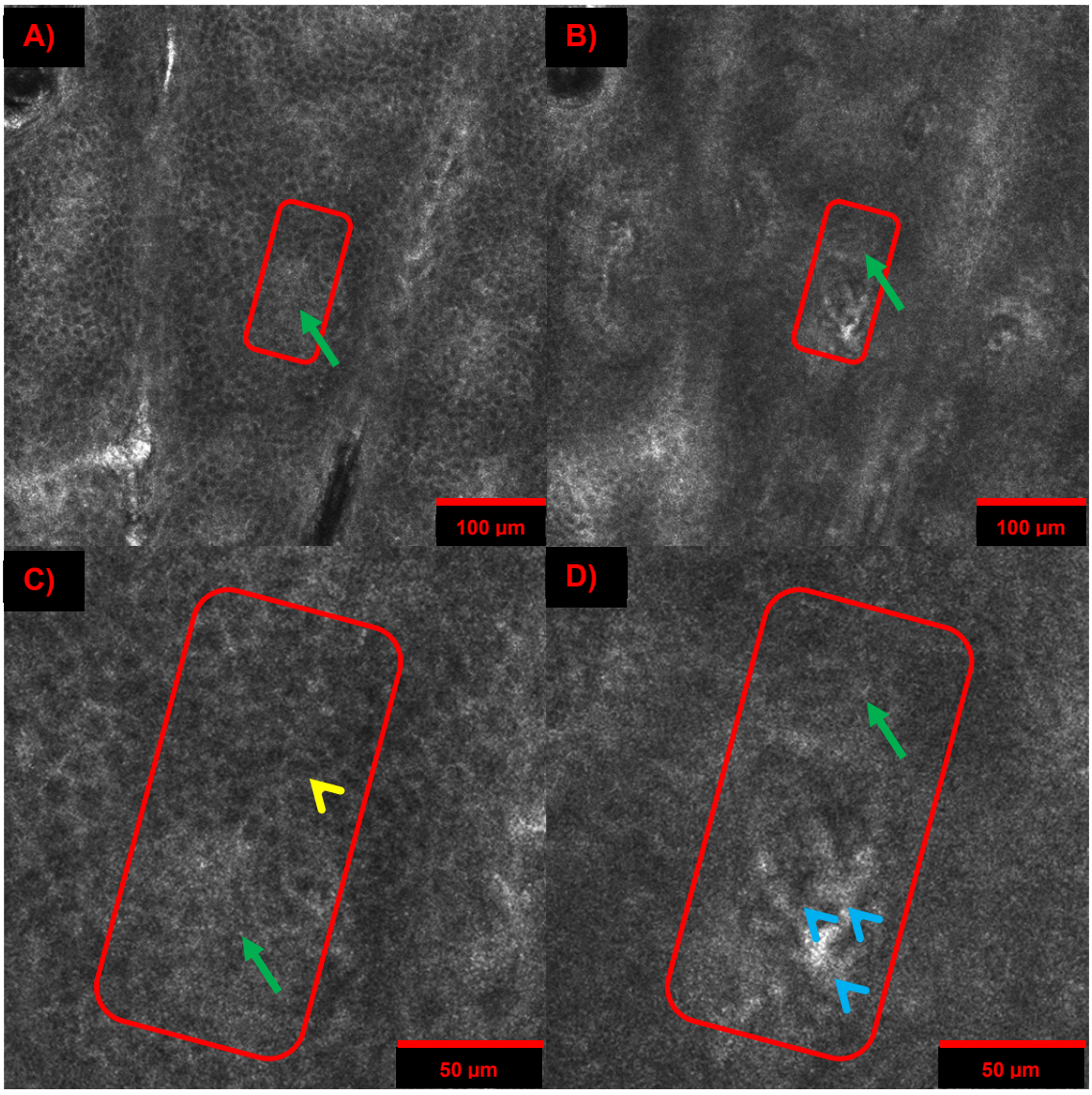

Figure 3.3 RCM Features of the DEJ Utilized to Determine VET
The same measurement ROI shown in Figure 3.2 is indicated by the red outline in each sub-panel. 3.1A, C: The top of the DEJ within the ROI was identified as the first frame in the ROI where cellular outlines were not distinct, indicating an area containing the feature-less basement membrane (green arrows). Cellular outlines (yellow arrowhead) are visible in the upper portion of the ROI. The bottom of the DEJ was defined as the frame below the last frame in the ROI where cellular outlines were distinguishable. 3.1B, D:

No circular cellular outlines are visible in the ROI. The upper portion of the ROI contains basement membrane (green arrows), and the lower portion of the ROI contains highly scattering, linear features of the dermal matrix (blue arrowheads).

For cell area measurements, an image frame within the SG and one within the SS was identified in each image stack based on characteristic cell morphology of the two layers (SG – immediately below the SC with larger cells; SS – below the SG, transition between the two layers in the image stack identified when cells become smaller). Cells within each image frame were manually outlined using the 'Freehand selections' tool in Fiji and the area of the outlined regions was calculated using the 'Measure' function in Fiji [73, 74]. The areas of approximately 10 cells were measured in the SG and SS of each image stack. A program was developed to randomize the grading order of image stacks, and to blind the grader to test site information (subject, timepoint, treatment).

3.3 Results: A Moderate Barrier Insult Confined to the SC Induces Changes in the Viable Epidermis

To evaluate the immediate effects of tape stripping, data from both test sites were pooled for the baseline and post-tape stripping timepoints as the first Petrolatum application occurred after the post-tape stripping measurements were completed.

3.3.1 Tape Stripping to Three Times Baseline TEWL Removes Half of the SC

Test sites were tape stripped using a standardized methodology until TEWL was between three and four times the baseline value (Figure 3.4). To confirm that the amount of

barrier disruption was similar between the test sites randomized for treatment and sites randomized for no treatment, the TEWL values before and after tape stripping were compared for both sets of test sites. TEWL increased in the Petrolatum designated test sites from 4.49 ± 0.51 g/m^{2}hr to 14.1 ± 1.54 g/m^{2}hr, and TEWL increased in the untreated designated test sites from 4.38 ± 0.43 g/m^{2}hr to 14.45 ± 1.46 g/m^{2}hr (mean ± standard error of the mean).

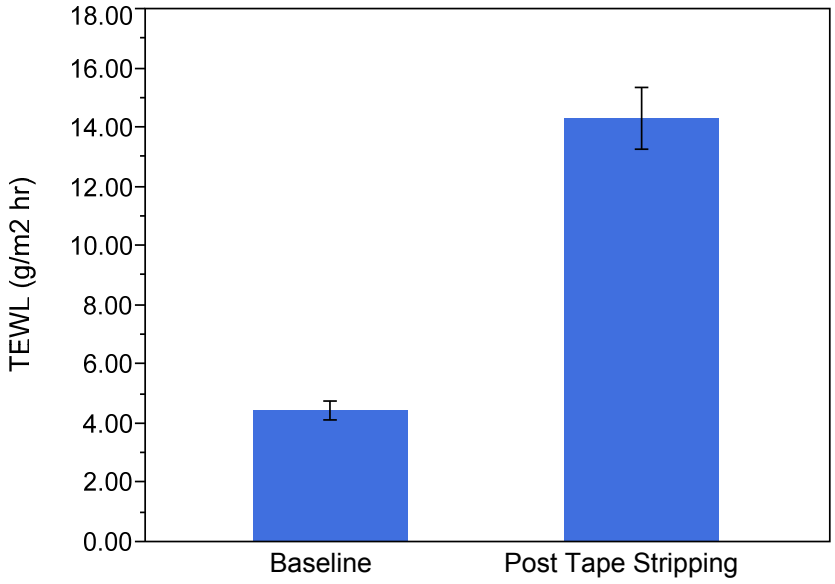

Figure 3.4 Test Sites were Tape Stripped to Three Times Baseline TEWL
Average pre-tape stripping TEWL (4.43 ± 0.33 g/m^{2}hr) and post-tape stripping TEWL (14.29 ± 1.04 g/m^{2}hr) including both test sites randomized to Petrolatum treatment and test sites randomized to no treatment. Data is represented as mean ± standard error of the mean.

Average SCT in tape stripped sites was 4.5 ± 0.3 μm compared to 10.7 ± 1.3 μm in control sites (Figure 3.5). To further confirm that the level of barrier disruption was similar in test sites randomized to treatment versus test sites randomized to no treatment, SCT after tape stripping was compared between the two sets of test sites. SCT in sites

designated for Petrolatum treatment was 4.5 ± 0.6 µm, and SCT in sites designated for no treatment was 4.5 ± 0.4 µm. SCT is reported as mean ± standard error of the mean.

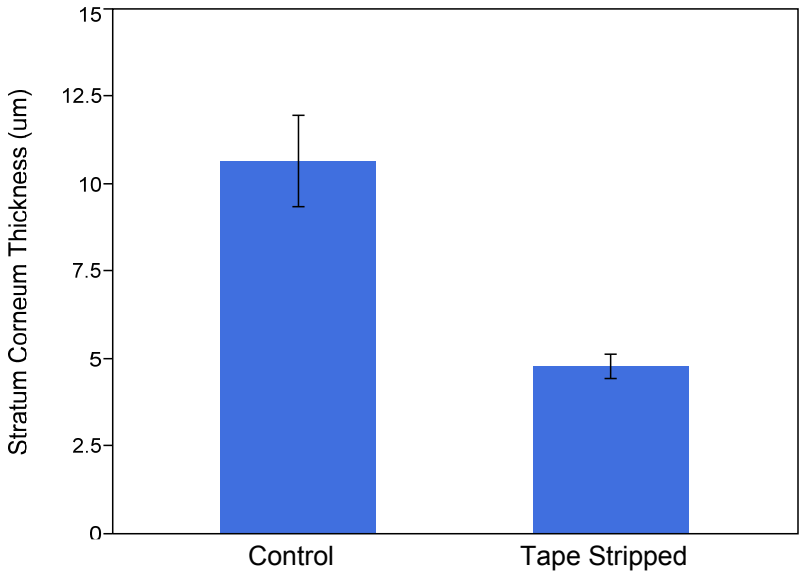

Figure 3.5 SCT in Control and Tape Stripped Sites.
SCT in sites tape stripped to three times baseline TEWL was approximately half the SCT measured in control sites. Data is represented as mean ± standard error of the mean.

3.3.2 Morphological Changes in the Viable Epidermis are Observed Immediately After Tape Stripping

Two out of the three parameters of morphology of the viable epidermis measured from RCM images were significantly impacted by the tape stripping procedure. VET was reduced by 13.8% (6.1 ± 2.0 µm) and SG cell area was reduced by 13.7% (83.8 ± 34.6 μm^2) in tape stripped sites compared to control sites (Figure 3.6).

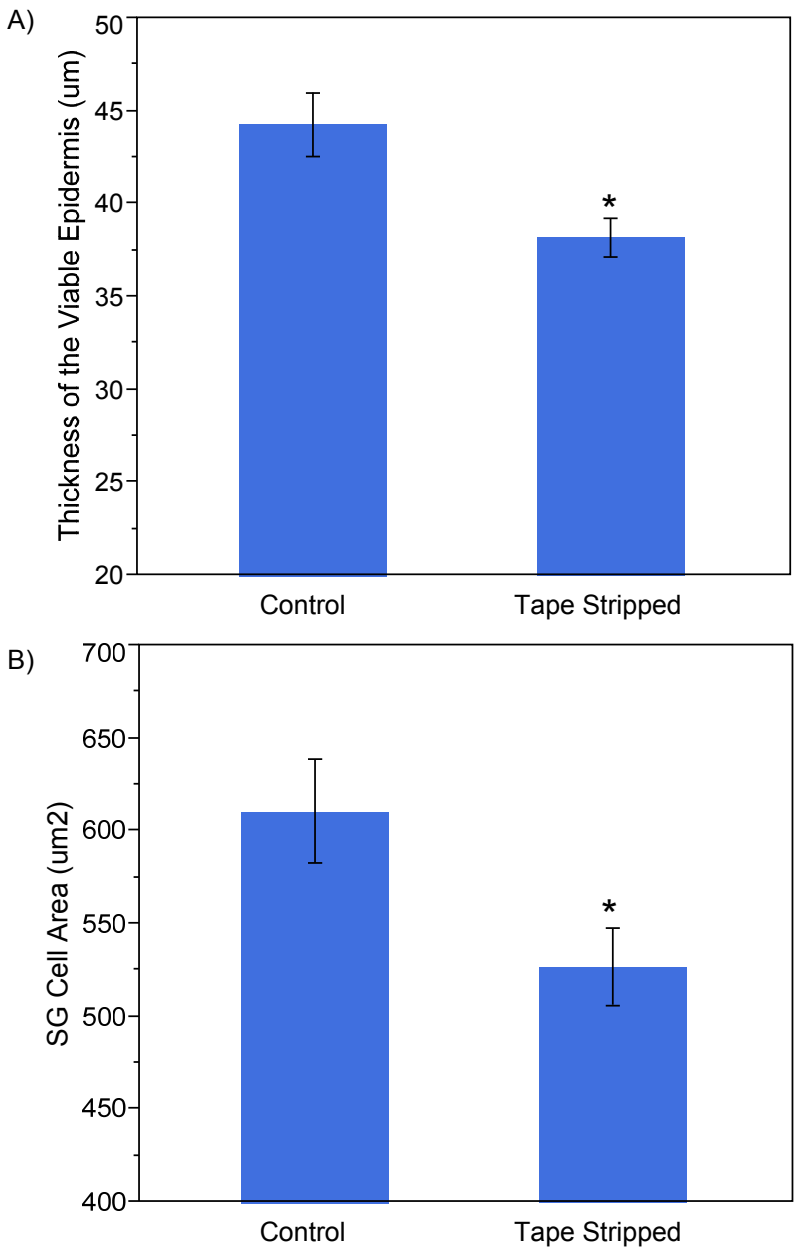

Figure 3.6 Tape Stripping Induces Morphological Changes in the Viable Epidermis. A) VET was reduced by 13.8% in sites tape stripped to TEWL values between 3 and 4 times baseline values compared to control sites. B) SG cell area was reduced by 13.7% in tape stripped sites versus control sites. (* $p<0.05$ versus Control sites, t-test).

The third parameter, SS cell area, was not statistically different in control versus tape stripped sites (610.2 ± 78.7 μm^2 vs 526.4 ± 76.8 μm^2), indicating that with the tape

stripping methodology utilized in this study, morphological effects were limited to the upper layers of the viable epidermis. Average SS cell area is reported as mean ± standard error of the mean.

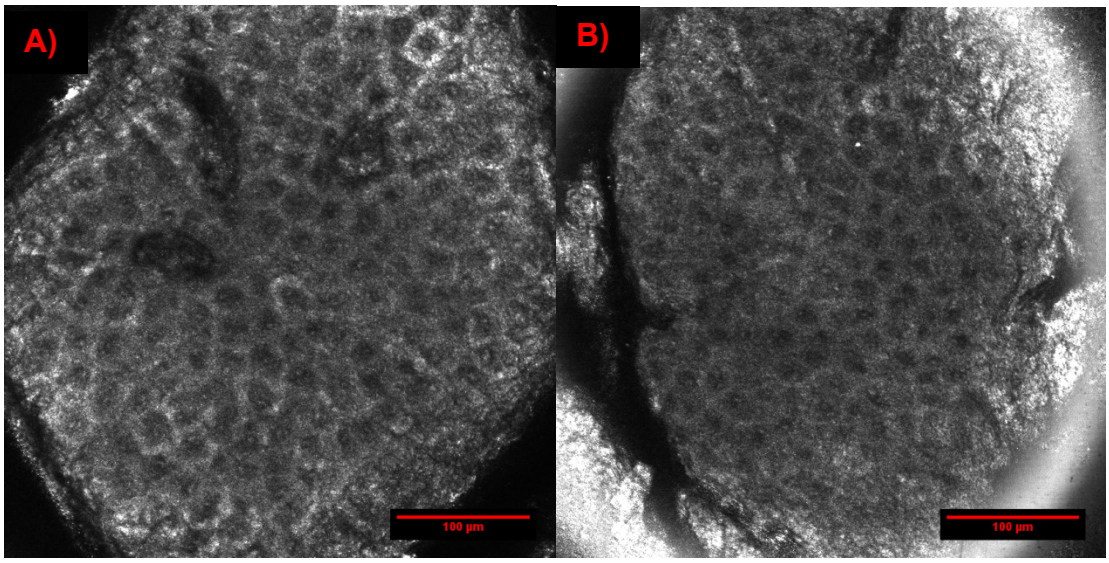

Figure 3.7 Cell Area in the SG is Reduced Immediately After Tape Stripping. Representative images of the SG layer in the control site (3.7A) and a tape stripped site (3.7B)

3.4 Results: Dynamic Measurement of the Recovery of Skin Barrier Function After Tape Stripping over One Week

3.4.1 Return of TEWL Values to Basal Levels is Approximately Linear Over Time

The recovery of TEWL to basal levels was evaluated at each time point as the percent reduction of the initial TEWL increase induced by the tape stripping insult (Percent recovery = [1 – [a – b]/[c-b]]*100, where a = TEWL measurement at a particular timepoint, b = TEWL measurement at baseline, c = TEWL measurement immediately after tape stripping). TEWL Percent Recovery increased in a linear manner over the

seven day study (r^2 = 0.94 in petrolatum treated sites, r^2 = 0.98 in untreated sites). TEWL Recovery increased between 10-11% per day, and after 7 days TEWL Recovery was near 80% (Figure 3.8).

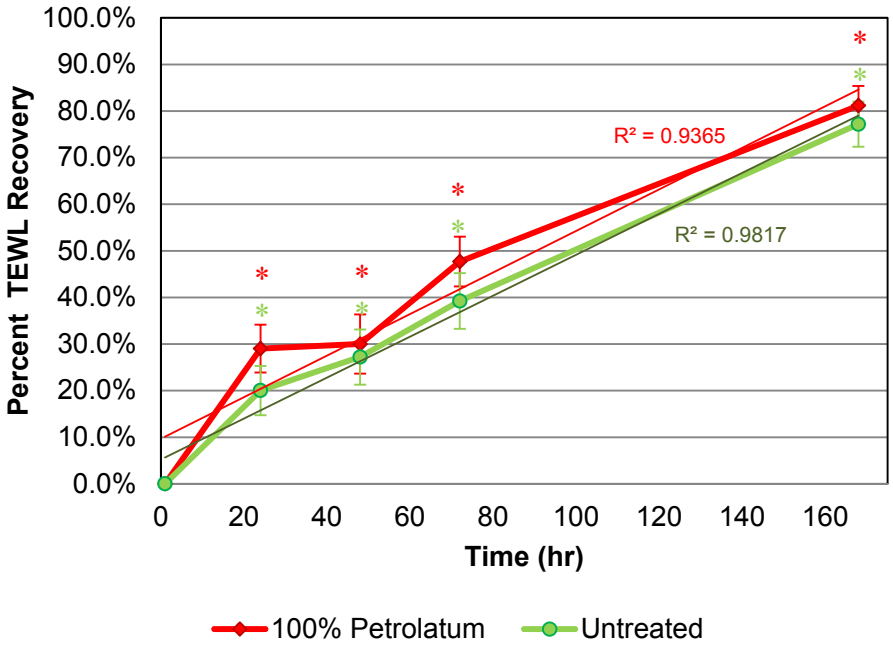

Figure 3.8 Percent TEWL Recovery is Linear with Time After Tape Stripping. TEWL values did not completely return to baseline levels (* = Percent TEWL Recovery different from 100% at all timepoints, $p<0.0001$ single sample t-test). Percent TEWL Recovery was similar in untreated sited (green) and in sites treated twice daily with petrolatum (red), and increased linearly over time.

To further evaluate the kinetic response of TEWL recovery over time, additional regression analyses on the raw data were performed. When regression analysis was performed including all test sites within a treatment, the r^2 values were 0.70 and 0.66 in Petrolatum and Untreated sites, respectively (Figure 3.9). Additionally, regression analysis was performed for each test site individually, and the average r^2 over all test sites was 0.83 (range 0.39-0.99, median 0.87). These additional regression analyses confirm the linear response of TEWL recovery over time.

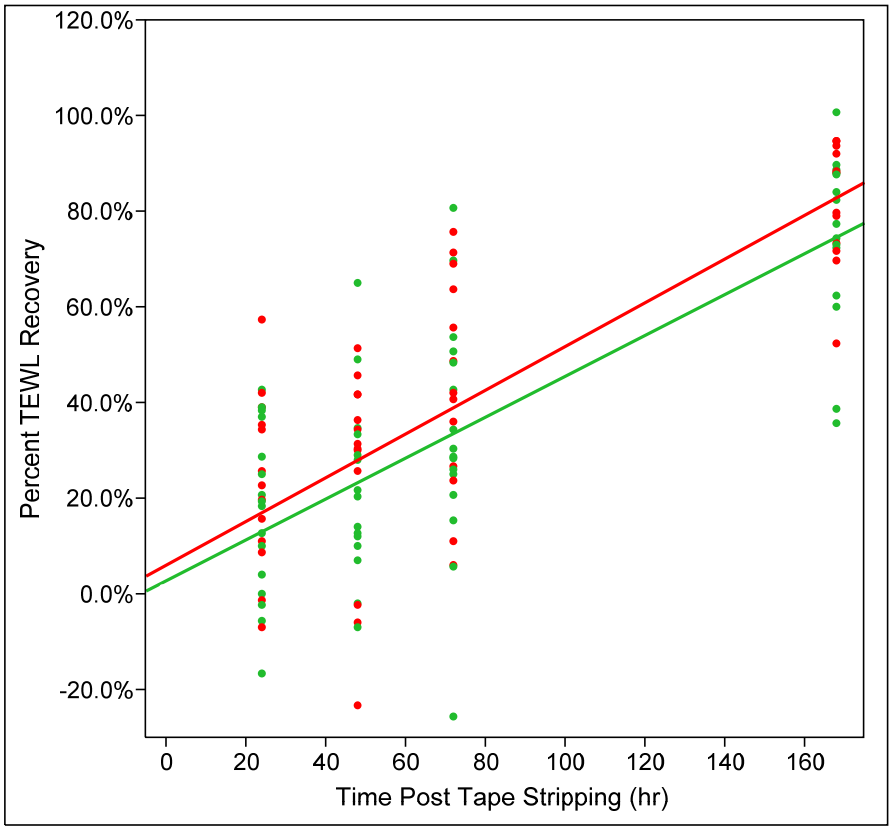

Figure 3.9 Distribution of TEWL Percent Recovery Across Subject Population
Data from Petrolatum treated sites is shown in red and data from Untreated sites is shown in green. Linear regression lines for each data set are shown in the respective colors. r^2 = 0.70 for the Petrolatum group and r^2 = 0.66 for the Untreated group. All test sites begin at 0% recovery at t=0 hours.

Evaluation of TEWL values over the course of the study without standardization by level of barrier damage also demonstrates a linear response. However, removal of the normalization factor increases the variability in the data at earlier timepoints. When regression analysis is performed on the un-normalized data, the correlation coefficient decreased from 0.70 / 0.66 to 0.32 / 0.27 in Petrolatum treated and Untreated sites, respectively (Figure 3.10).

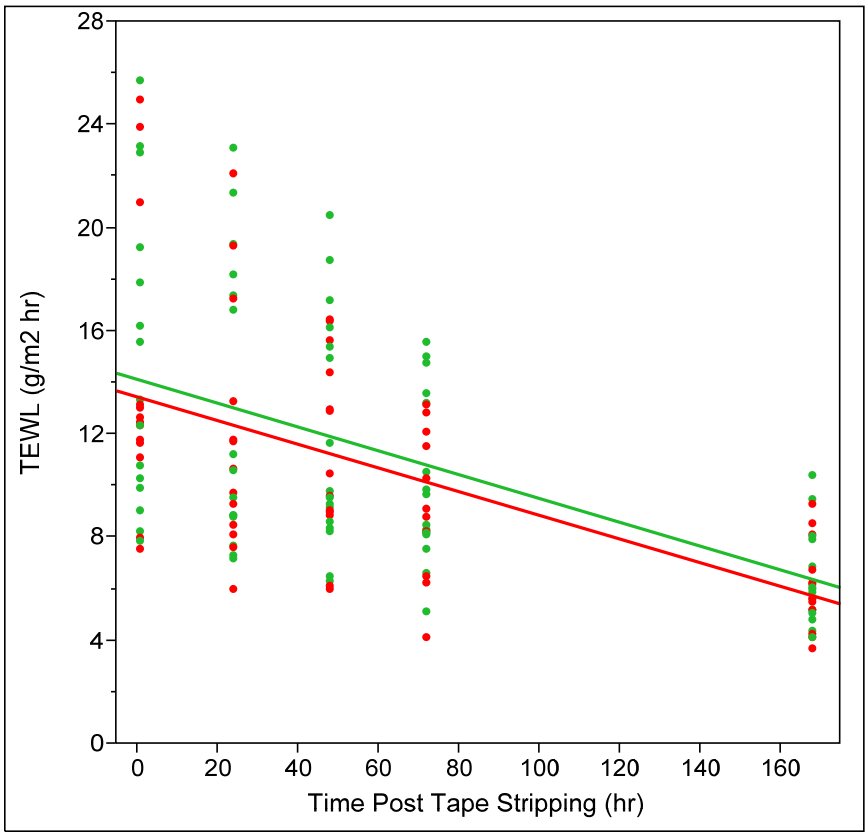

Figure 3.10 Time course of TEWL values is similar to that observed in Percent TEWL Recovery.
The same linear trend is observed in TEWL return to baseline values in non-normalized data. Variability at the earlier timepoints was increased when the data was not standardized to Percent TEWL Recovery due to the inter-individual and inter-test site variability in basal TEWL levels. Individual TEWL values are represented as filled circles (Petrolatum – red, Untreated – green), and linear regression lines are shown in the respective colors. $r^2 = 0.32$ for the Petrolatum group and $r^2 = 0.27$ for the Untreated group.

3.4.2 Erythema Peaks at 24 hours Post Tape Stripping

Irritation at the test sites was evaluated through cross-polarized digital imaging. Introduction of orthogonally oriented linear polarization filters at the light source and in front of the camera eliminates specular reflection from the surface of the skin (shine), and therefore enables more sensitive evaluation of color changes (Figure 3.11) [95].

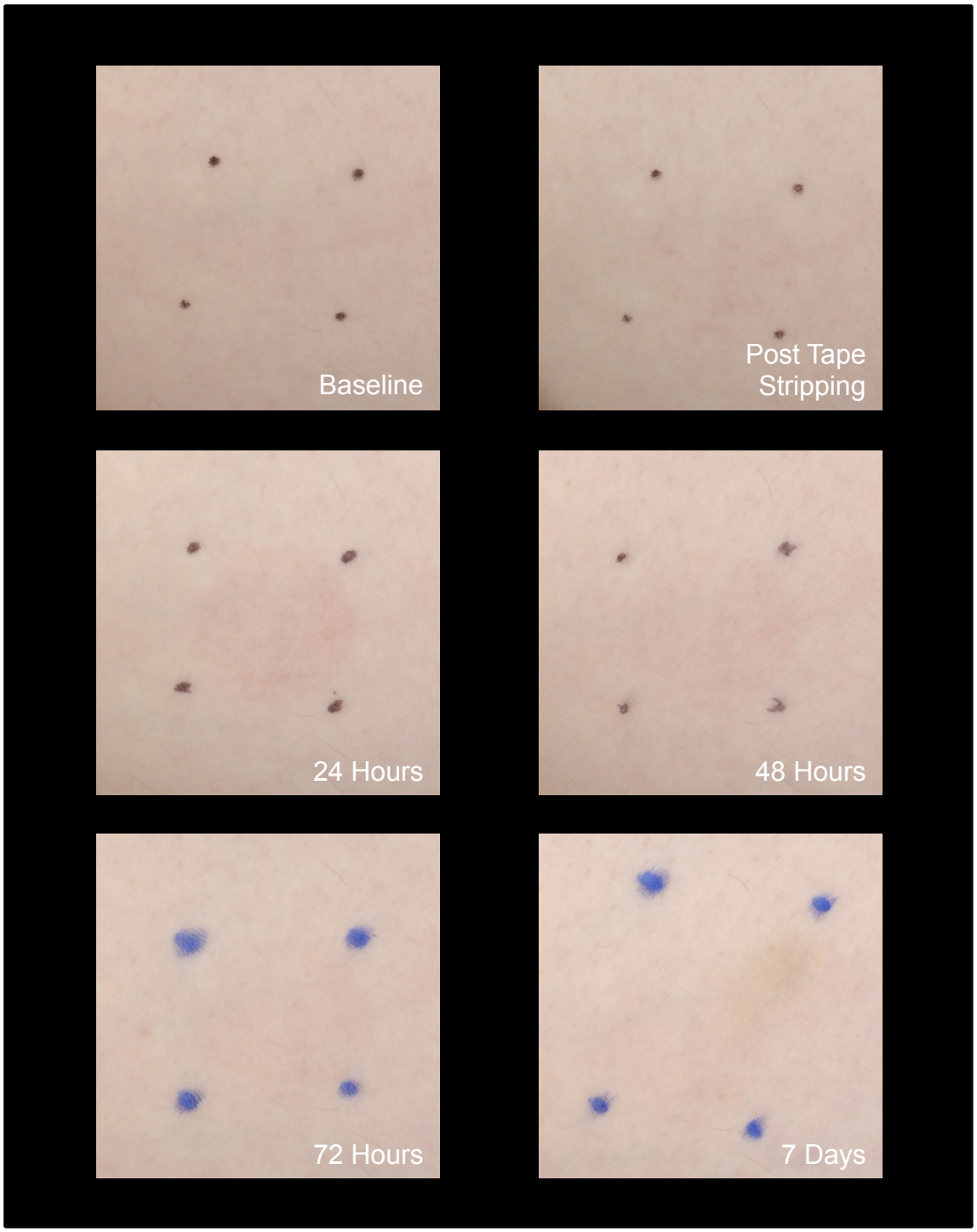

Figure 3.11 Representative Cross Polarized Images Demonstrate Maximum Erythema at 24 Hours Post Tape Stripping

Cross polarized images of a representative test site over the course of the study. The corners of the test site were marked at each visit, and subjects were instructed to re-mark the test sites if needed between timepoints.

A proprietary algorithm was used to generate maps of Erythema Index (EI) based on RGB values of the images, and the change in EI from baseline was calculated at each test site at each timepoint (Figure 3.12).

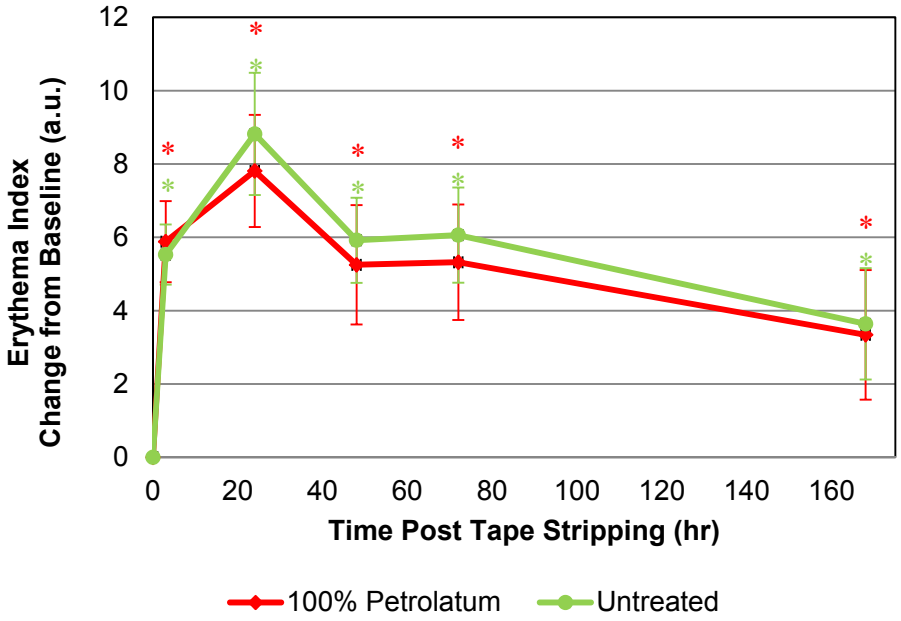

Figure 3.12 Erythema Index Increases After Tape Stripping.
Erythema Index (EI), calculated from cross-polarized digital images, peaked at 24 hours post tape stripping and remained elevated throughout the study. There was no difference in EI due to treatment. (Average change in EI different from 0, * $p<0.05$ single sample t-test)

EI peaked at 24 hours post tape stripping, then decreased gradually but remained above baseline values in both Petrolatum treated and Untreated sites over seven days. The maximum EI response at 24 hours post stimulus consistent with the erythema response observed after UV exposure, another example of an acute stimulus inducing an inflammatory response [96].

3.4.3 Changes in SCT and VET after Tape Stripping Demonstrate Different Kinetics

Tape stripping removed approximately half of the SC, and following the tape stripping procedure SCT increased linearly at a rate of approximately 0.5 µm / day. After seven days SCT did not fully return to control site thickness (Figure 3.13). There were no statistical differences between the treatments; however a post-hoc power analysis indicates that a difference of 1.1 µm in SCT, as observed between the Petrolatum and Untreated sites at 7 days, would be found in a sample size of 20 subjects (alpha = 0.05, power level 80%). These data may be useful in future studies evaluating treatments for determination of sample size.

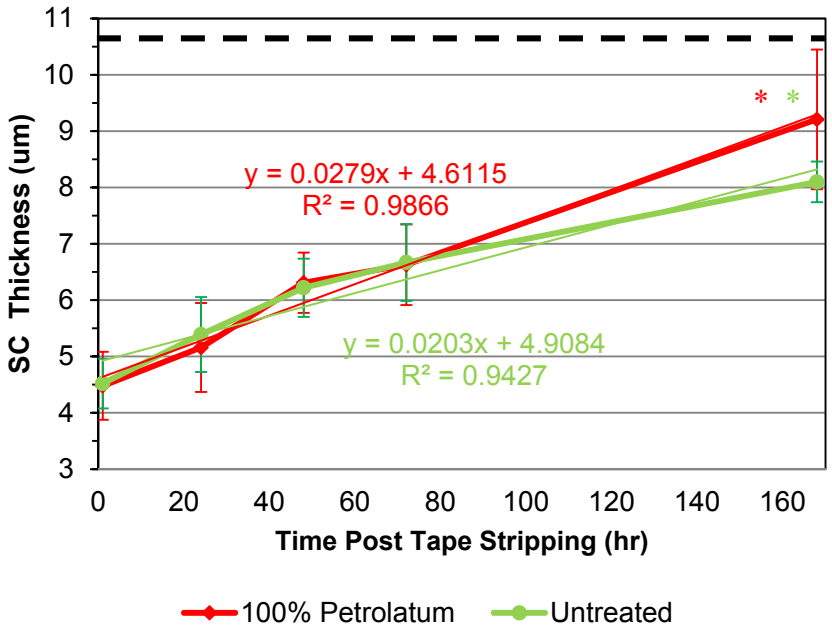

Figure 3.13 SCT increased linearly after tape stripping at a rate of 0.5 µm / day. After 7 days, SCT is elevated compared to post tape stripping (* $p<0.05$ Dunnett's test with control) but remained reduced compared to control site SCT (indicated as black dashed line)

VET was reduced immediately following tape stripping, but at 24 hours post tape stripping increased to control site levels (Figure 3.14). VET continued to increase until 48 hours and then returned to control site levels for the duration of the study. VET was statistically greater than immediately post tape stripping at all subsequent study timepoints.

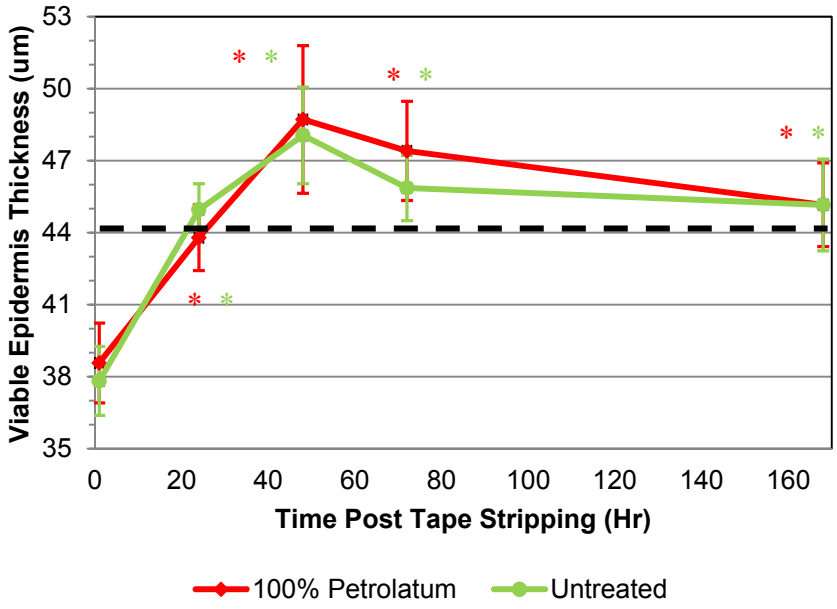

Figure 3.14 Evolution of VET After Tape Stripping.
VET is reduced immediately after tape stripping, and increases above control site levels (indicated as black dashed line) at 48 hours post tape stripping. After 7 days, VET in tape stripped sites returns to control site levels. VET is greater at all timepoints post-tape stripping compared to immediately after tape stripping in both Petrolatum and Untreated sites (* $p<0.05$ versus post tape stripping, Dunnett's test with control).

3.4.4 Cells in the SG and SS Layers Respond to Barrier Disruption with Different Kinetic Patterns

Barrier disruption through tape stripping induces an immediate response in the SG, as indicated by the 13.7% reduction in SG cell area in post tape stripped sites versus control (Figure 3.6B). SG cell area continues to decrease through 72 hours post tape stripping, and remains lower than control site values throughout the 7 day study (Figure 3.15A).

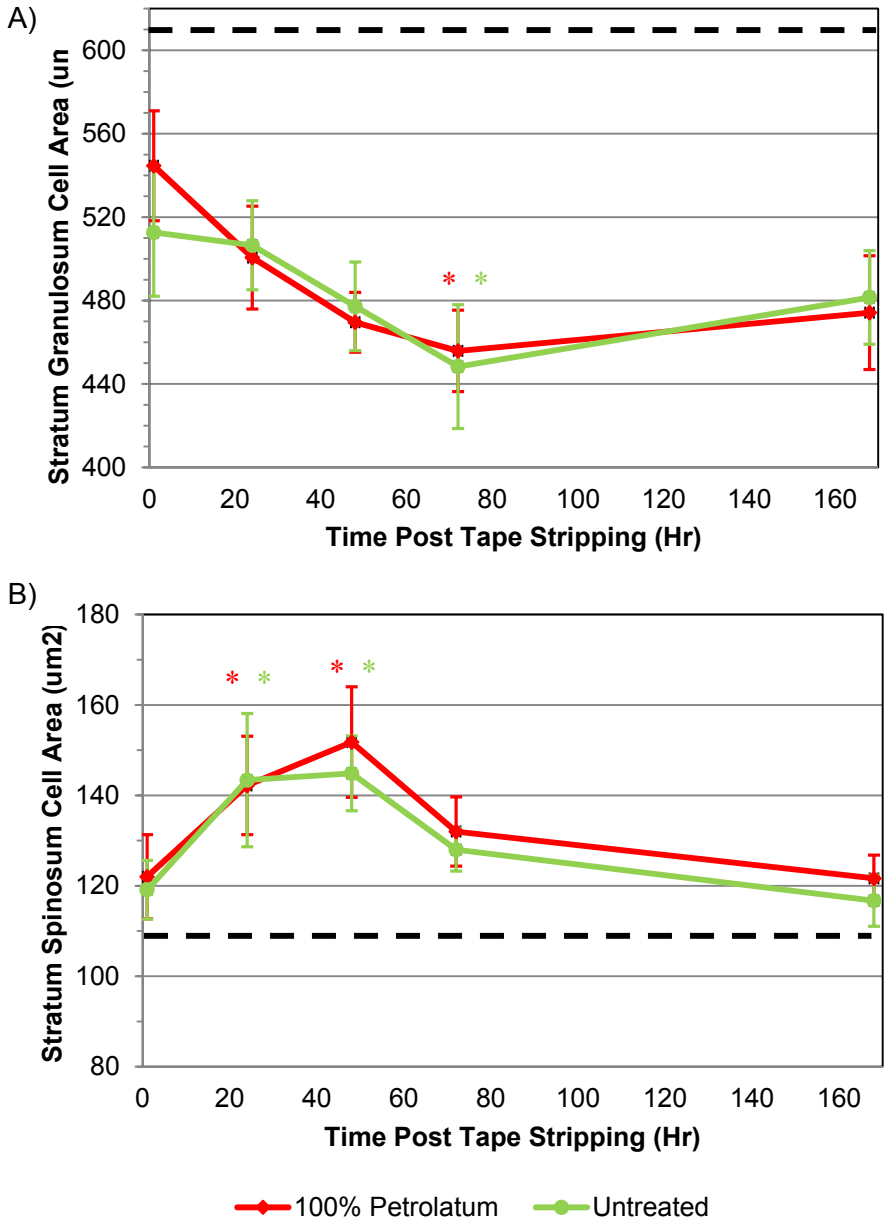

Figure 3.15 Changes in Area of SG and SS Cells Indicate Differing Roles in Epidermal Barrier Repair.
A) SG cell area was lower immediately after tape stripping than in control sites, and continued to decrease through 72 hours post tape stripping. SG cell area was significantly decreased at 72 hours versus immediately after tape stripping in both Petrolatum treated and Untreated sites. B) SS cell area increases at 24 and 48 hours post tape stripping (* $p<0.05$ versus immediately after tape stripping, Dunnett's Test with Control). Control site values are indicated on each graph as the black dashed line.

In contrast to the SG, cell area in the SS appeared to not be immediately affected by tape stripping. SS cell area increases at 24 and 48 hours post tape stripping, and returns to control site values by one week post tape stripping (Figure 3.15B). The kinetics observed in SS cell area are similar to the changes in VET observed throughout the study.

3.5 Discussion & Conclusions

The results of the present study demonstrate the morphological changes and corresponding functional effects of a moderate disruption to the skin barrier. In-vivo imaging and microscopy were utilized to capture these significant dynamic changes in situ, and TEWL measurements were collected to monitor overall skin barrier function. Tape stripping to three times baseline TEWL values removed approximately half of the SC, and immediate changes in the viable epidermis were observed after tape stripping, as both SG cell area and the thickness of the viable epidermis were reduced. Erythema was observed following the tape stripping procedure, and peaked at 24 hours post tape stripping. The functional performance of the skin barrier, as measured by TEWL, recovered in a linear manner over the course of the study. The thickness of the SC, the

layer which provides the much of the permeability barrier function of the skin, also increased in a linear manner over the course of the study.

In this work, we demonstrate how RCM may be used to probe and visualize dynamic changes occurring at a microscopic level within the skin, revealing new insights by monitoring changes which have been previously observable only through histological evaluation. We show evidence of morphological changes in response to barrier disruption, effects which to our knowledge have not been quantitatively measured in vivo. While the physical process of tape stripping in this study is confined to the SC, changes in the morphology of the viable epidermis were observed, potentially indicative of signal transduction between the SC and the viable layers. Several mechanisms of signal transduction are known to occur in the skin, based on mechano-transduction, chemokines, and cellular response to changes in ion and water concentration gradients [97-100]. Identification of a mechanism of action of this potential signal transduction was beyond the scope of this thesis, and may be further explored utilizing the methodologies developed through this work as well as the methods developed in the subsequent chapters of this thesis.

Immediately after tape stripping, we observed a decrease in the area of SG cells and a decrease in the thickness of the viable epidermis. Immediate reduction in SG cell area after barrier disruption has been qualitatively described in the literature following full removal of the SC, and hypothesized to be reflective of cell desiccation [42]. While desiccation of the SG would be expected when the full SC is removed and the SG is

exposed to the external environment, in the present study approximately half of the SC remained. The remaining SC protected the SG from direct exposure and the potential for desiccation, suggesting that the morphological changes in the viable epidermis observed after tape stripping were initiated through biological processes. Histological evidence from animal studies has elucidated some of biological repair processes which are stimulated by barrier disruption. Lamellar bodies containing pro-barrier lipids have been shown to be secreted from SG cells to the SC / SG interface within 30 minutes following barrier disruption, which suggests that the reduction in SG cell area immediately after tape stripping may be due to lamellar body degranulation [76]. The changes in SG cell area and VET shown in the present study are likely due to a combination of biophysical and biological responses, and further work and additional tools are necessary in order to separate the contributions of each.

Through comparison of our study on skin barrier recovery after a moderate disruption to reports in the literature of barrier recovery after full SC removal, we are able to assess the effect of level of disruption to the barrier on the kinetic rate of recovery as measured through both functional and morphological endpoints. In this study, TEWL did not completely return to baseline values after one week, and the Percent TEWL Recovery increased in a linear manner approximately 10% per day (corresponding to TEWL decreases on the order of 1-2 g/m^2hr per day). After tape stripping to remove the full SC, Bargo et al. observed a linear decrease in TEWL on the order of 10 g/m^2hr per day for the first three days post tape stripping [42]. The rate of SCT increase was also elevated after removal of the full SC compared to the moderate barrier disruption in the present study

(2.3 μm / day versus 0.5 μm / day) [42]. These findings provide the groundwork for the further studies which are necessary to conclusively demonstrate that the level of barrier disruption determines the kinetics of barrier repair.

Comparison of the amount of SC removal to increase in TEWL is also useful to evaluate the efficiency of the barrier at different levels within the SC. Bargo et al observed an increase of approximately 7-9x TEWL with full removal of the SC. In the present study, removal of half of the SC resulted in an increase of approximately 3x TEWL. This suggests that the lower portion of the SC provides a greater proportion of barrier efficiency than the upper half of the SC. The hypothesis of differing levels of barrier efficiency at different levels of the SC has been explored in the literature through various techniques, and our work adds additional evidence to support this hypothesis [101-103].

The evolution of epidermal morphology may be used to infer proliferation and differentiation status. Previous studies using RCM have demonstrated that increases in VET correspond to validated markers of proliferation: Peppelman et al correlated increases in VET to increases in Ki67 through immunohistochemistry of biopsy sections, and Bargo et al correlated VET to tryptophan fluorescence, which has been used as an in-vivo marker for proliferation [31, 42, 104]. In addition, reduced SG cell area has been shown in skin states of enhanced proliferation [5]. We demonstrated that SG cell area is reduced immediately after tape stripping, potentially an immediate response of lamellar body degranulation, and continues to decrease up to 72 hours after tape stripping. The reduction in SG cell area in the 72 hours after tape stripping is observed with a

concomitant increase in VET, which together indicate a proliferative response to the tape stripping barrier insult. SS cell area increases at 24 and 48 hours post tape stripping, potentially due to enhanced cellular metabolism. The relationship of projected cell area to proliferation status may be further confirmed as in-vivo imaging technologies improve to enable measurement of epidermal cell volume (area and thickness) and therefore definitively assess whether changes in epidermal layer thickness are due to enlargement of cells or increases in cell number.

There are conflicting reports in the literature on the impact of topical treatment with petrolatum on skin barrier function and repair. Petrolatum has been shown to accelerate, impair, or have no effect on skin barrier recovery [105-107]. The absence of an observed effect in this study may be due to the small sample size, the fairly moderate initial barrier disruption, the choice of the upper inner arm as test site, and / or the timepoints chosen for assessments. The upper inner arm is naturally semi-occluded due to clothing as well as physical proximity to the body. The mechanism of action of petrolatum is generally considered to be occlusion so to optimally differentiate changes in barrier function due to treatment, the control site would need to be completely unoccluded. In addition, subjects were instructed to not apply petrolatum on the mornings of the study visits, in order to ensure that the measurements were not impacted by product remaining on the surface of the skin.

In this study, we demonstrate in-vivo through combined microscopic and macroscopic measures that morphological changes in the epidermis are accompanied by changes in

barrier function. Our results confirm the previously published kinetic response of VET after barrier disruption, and further show that the rate of replenishment of the SC layer corresponds to the level of barrier disruption. We also demonstrate that RCM measurements of cell area of the SG and SS layers may be additional morphological parameters useful to quantify epidermal barrier function and proliferation / differentiation status. To our knowledge, this work is the first to utilize dynamic and quantitative measures of cell area in vivo to show changes in skin barrier function, and these findings indicate that measurement of epidermal morphology at the cellular level may help to better understand the biological process of skin barrier recovery.

Areas for future investigation include work to deconvolve the biological and biophysical processes contributing to barrier function within the skin. Emerging technologies which integrate measurements of skin morphology and composition, such as combined reflectance confocal microscopy and Raman confocal microspectroscopy, may provide additional insights. Advances in RCM instrumentation to increase axial resolution will enable work to further elucidate mechanisms of the proliferative response of the epidermis through monitoring of cell volume as well as number of cells within the various layers.

3.6 Supplemental Information

3.6.1 Disposition of Subjects and Analysis Dataset

24 subjects were screened, out of which 20 subjects were enrolled and 19 subjects completed the study procedures. Some subjects who completed the study were excluded from the data analysis as explained below. Four subjects were discontinued at the initial visit due to screen failures baseline, specifically the baseline TEWL values were below the minimum set in the inclusion criteria. One subject was discontinued at the third visit due to a protocol violation (took steroidal medication). One subject's data was excluded from the analysis dataset due to an adverse event. In the remaining 18 subjects, test sites where TEWL increased greater than 4 times the baseline value after tape stripping were excluded from all analyses (3 sites, all randomized to Petrolatum treatment). TEWL measurements from two additional subjects were excluded due to instrument malfunction, resulting in a final TEWL dataset of n = 16 subjects for the Untreated group and n = 13 for the Petrolatum treated group. Baseline cross-polarized images from two subjects were not usable, resulting in a final EI data set of n = 16 for the Untreated group and n = 14 for the Petrolatum treated group. RCM was collected on a subset of 8 subjects, and in two subjects the Petrolatum site was excluded from analysis as the TEWL increase after tape stripping was greater than 4 times baseline value. Therefore, the RCM data presented represents n = 8 subjects for the Untreated group and n = 6 subjects for the Petrolatum treated group.

3.6.2 Additional Analyses of RCM Images

Two additional endpoints potentially related to skin barrier recovery processes were explored in the RCM images: dilation of the capillary lumens and scattering intensity profiles. The tape stripping procedure produced a measurable amount of erythema, as documented in the cross polarized images. Theoretically, this macroscopic erythema derives from increased blood flow to the superficial vessels, including the capillary loops extending into the dermal papillae. RCM image stacks were examined for the presence of capillaries, and while capillary loops were discernable in nearly all of the image stacks, the capillary lumens were not consistently clearly distinguishable to enable quantification (Figure 3.16). In future studies, this endpoint may be further evaluated if the imaging locations are chosen such that the capillary lumens are clearly distinguishable.

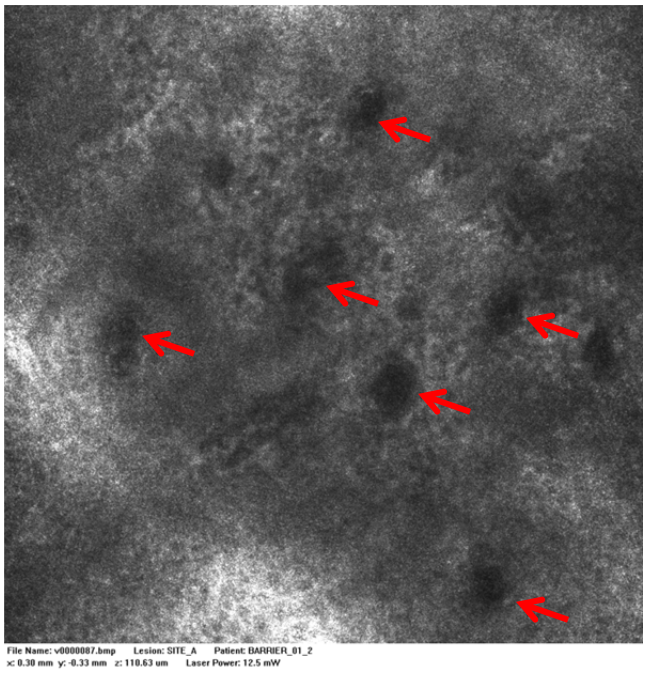

Figure 3.16 Representative Image of Dermis in RCM
Capillary loops are visible in images of the dermis (red arrows), however the individual capillary lumens were not distinguishable enough for quantification.

Scattering properties of the epidermis and upper dermis may be quantified by calculating the average grayscale intensity within a specified ROI as a function of depth within the image stack and normalizing the intensity by the source laser power. This analysis method was explored because scattering intensity profiles have been shown to be different in infant and adult skin, and hypothesized to be related to differences in collagen and elastin bundles in the upper reticular dermis [5]. In this study, we did not observe any differences in scattering intensity profiles within the viable epidermis and upper dermis across timepoint or treatment (Figure 3.17). Additionally normalized scattering intensity was not different between the control sites and tape stripped sites. These initial data suggest that the moderate tape stripping barrier insult did not induce changes in the collagen and elastin structure in the upper dermis.

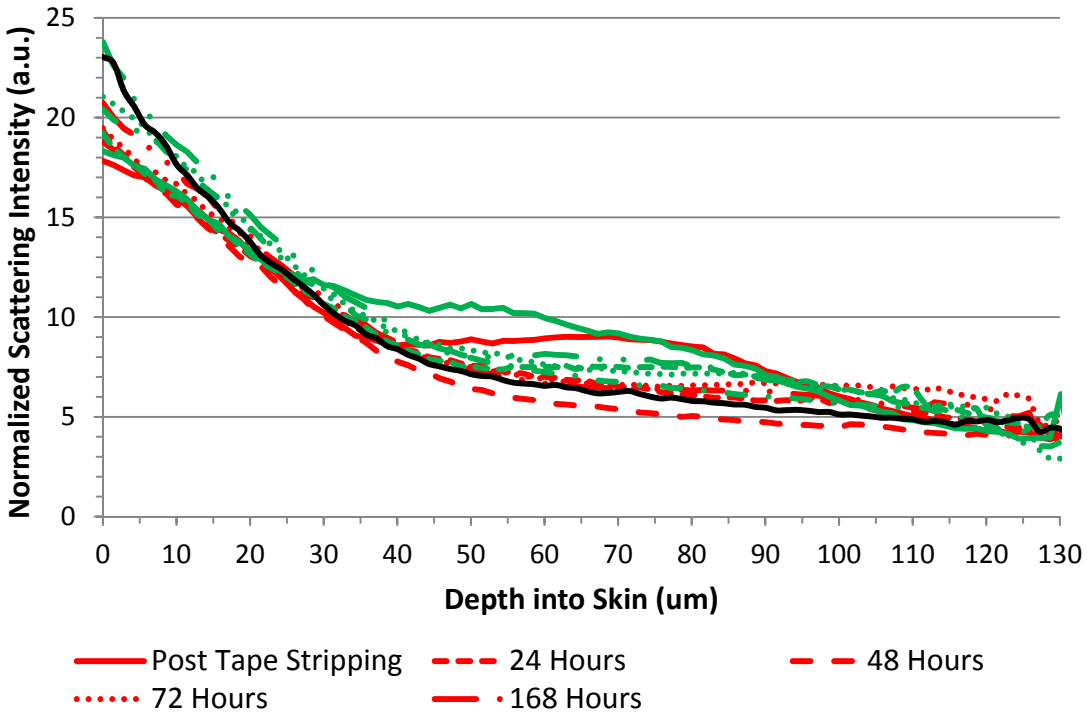

Figure 3.17 Normalized Scattering Intensity Profiles are Similar across Treatments and Timepoints

Average scattering intensity within a designated region of interest was calculated across images within a stack, and each average intensity was normalized by the laser power of image acquisition. The control site is shown in black, petrolatum treated sites are shown in red, and untreated sites are shown in green. Line style corresponds to timpoint for petrolatum and untreated site scattering intensity profiles as shown in the legend. The plateaus shown in the Post Tape Stripping timepoints (solid lines) for both the petrolatum and untreated sites were due to a few sites' proximity to hair follicles, which affect dermal structure. Image stacks at subsequent timepoints were collected at sites away from hair follicles to avoid this effect.

CHAPTER 4 Molecular Changes in Stratum Corneum Lipid Order Result in Functional Changes in Skin Barrier

The materials, images and text used in this chapter have been previously published, at least in part, in Experimental Dermatology as an original manuscript (M. Catherine Mack Correa, Guangru Mao, Peter Saad, Carol R. Flach, Richard Mendelsohn, Russel M. Walters. "Molecular Interactions of Plant Oil Components Correlate with Clinical Measures of Skin Barrier Function", Experimental Dermatology, 23:39-44, 2014). This publication represents the original work of Mary Catherine Mack as a first author as part of collaborative effort with several co-authors as customary to this field of research. Mary Catherine Mack has significantly contributed the following to this publication: literature search, designing the clinical protocol and overseeing execution of the clinical study, analyzing the clinical study data and creating the relevant figures and tables, writing the clinical sections of the manuscript and incorporating the in-vitro and ex-vivo sections from co-authors, responding to reviewers' comments, and submission of the manuscript.

4.1 Abstract

The molecular order of stratum corneum (SC) lipids contributes to the permeability barrier of the skin. Topically applied exogenous agents may interact with the SC lipids and these interactions are hypothesized to lead to changes in skin barrier function. The objective of this study was to develop in-vivo methodologies to mechanistically assess the interaction of topical ingredients with SC lipids and overall impacts on barrier function. Two components of plant-derived oils were used as model compounds: oleic acid (OA) and glyceryl trioleate (GT). The effects of OA, GT, and OA/GT mixtures on

skin barrier were assessed in-vivo through measurement of transepidermal water loss (TEWL) and fluorescein dye penetration before and after a single application. OA's effects on stratum corneum (SC) lipid order in-vivo were measured with infrared spectroscopy through application of deuterated OA (OA-d_{34}). The oil mixtures increased both TEWL and fluorescein penetration 24 hours after a single application in an OA dose dependent manner, with the highest increase from treatment with pure OA. OA-d_{34} penetrated into skin and disordered SC lipids. The interaction between topically applied components and SC lipids likely determine the extent of their penetration and clinically measurable effects on skin barrier functions.

4.2 Background and Objective

In the prior chapter, we investigated the impact of epidermal morphology on skin barrier function, and demonstrated that non-invasive confocal microscopic techniques may be used to quantify morphological features of the epidermis that relate to skin barrier function. In addition to epidermal morphology, the composition and functional quality of the stratum corneum (SC) has a large impact on the resulting barrier function. For example, psoriasis is a hyperproliferative disease where transepidermal water loss (TEWL) is elevated in spite of the increased thickness of the viable epidermis and plaques of SC remaining on the surface due to impaired desquamation [108]. The work presented in this chapter combines microscopic and spectroscopic techniques in order to demonstrate in-vivo that molecular order of the SC lipids is directly related to skin barrier function.

The quality of skin barrier function is to a large extent determined by the structural order of intercellular SC lipids, the only continuous transport route throughout SC [109]. SC lipids, comprised of ceramides, cholesterol, and free fatty acids (FFAs), form ordered structures in multiple dimensions. The lipids arrange in lamellar layers with repeat distances of 6 and 13 nm [10]. Laterally, SC lipids organize in orthorhombic and hexagonal crystalline phases [50] with some disordered lipids also present [13]. Perturbation of the lamellar organization increases drug permeability in SC lipid models [51]. Prevalence of the more tightly packed orthorhombic phase has been shown to correlate with higher SC integrity and barrier efficiency as measured by TEWL [13, 110].

The structural organization of SC lipids is affected by both pathological conditions and the permeation of exogenous materials. In-vitro models have also demonstrated that SC lipid composition affects structural order and water transport properties thus presenting opportunities for development of therapeutic interventions to normalize lipid composition, restoring barrier function [111-113]. Abnormal lamellar structure and disrupted lateral order have been associated with compromised barrier function clinically in patients with psoriasis, ichthyosis, and atopic dermatitis as well as preclinically in cultured models of the epidermis [109, 114-119]. Additionally, exogenous compounds from topical skincare products can affect SC lipid molecular order and therefore have the potential to impact barrier function. Surfactants are well known to perturb the skin barrier through endogenous lipid removal and disordering [53, 55, 120]. The penetration of actives and delivery systems has been shown to disrupt SC lipid structural order [121-123] and is

often associated with increased TEWL [124]. OA, therapeutically used as a penetration enhancer, is known to be an irritant and to cause a significant increase in TEWL [125].

Plant-derived oils are a common ingredient in skincare product formulations. The chemical compositions of these oils consist primarily of triglycerides with various fatty acid chains and small fractions of FFAs [126, 127]. Commonly, oil-based formulations form an occlusive layer on the skin surface with penetration no further than the first few layers of the SC [128]. However, hydrolyzing conditions during manufacturing and storage may elevate FFA content in products. In addition, FFAs can be added directly to products as emollients or emulsifying agents. FFAs are known to penetrate into SC and enhance the permeation of other species [129, 130]. In this study OA, GT, and mixtures of the two were used to mimic the natural oils used in skincare formulations to better understand their effects on skin barrier function. We investigate the molecular interactions of OA with SC lipids in-vivo by infrared (IR) spectroscopy and evaluate the corresponding changes in skin barrier function using TEWL and in-situ fluorescence confocal microscopy.

4.3 Materials and Methods

4.3.1 Materials

OA, GT, and deuterated oleic acid (OA-d_{34}, 98 atom% D) were purchased from Sigma Aldrich (St. Louis, MO). Cosmetic grade sodium fluorescein (D&C yellow #8) was

purchased from Sensient Cosmetic Technologies (South Plainfield, NJ). All chemicals were used without further purification.

4.3.2 Clinical Protocol

Caucasian female subjects, Fitzpatrick skin types I-III, aged 21-40 years were recruited to participate in two studies. The subjects were in general good health with no history of skin disease and had no lesions or marks on the volar forearms which would interfere with the study measurements. The study protocols were approved by the Allendale Investigational Review Board (Old Lyme, CT) and conducted in accordance with the ethical principles of the Declaration of Helsinki. Written informed consent was obtained from all participants prior to enrollment.

Twelve subjects participated in Study 1. Five 2×6 cm^2 areas were marked on volar forearms and baseline measurements were acquired after 30 minutes acclimatization to room conditions. Four sites were treated with oils according to a randomization scheme, leaving one site as an untreated control. For the treated sites, 48 uL of either 100% OA, 50% OA/50% GT, 25% OA/75% GT or 100% GT (wt%), was gently rubbed onto the skin with a pre-saturated gloved finger. All sites were then covered with gauze. Plastic wraps were supplied to cover the arms while bathing. Measurements were taken 24 hours after the treatment following 30 minutes acclimatization to the testing room conditions.

Two subjects were included in Study 2. Two 2×6 cm^2 sites were marked on the volar forearms with one site treated with OA-d_{34} and the other serving as an untreated control. Treatments and measurements followed the same procedure as in Study 1, with the addition of an attenuated total reflectance Fourier transform infrared spectroscopy (ATR-FTIR) measurement.

4.3.3 Clinical Evaluations

TEWL was measured with a Vapometer (Delfin Technologies, Kuopio, Finland). Penetration of fluorescein was measured after 24 hours on a subset of subjects (n=5) in Study 1. Fluorescein (0.15% in water) was patched on each site for one hour, and fluorescence confocal image stacks were collected with the Vivascope 1500 (Lucid Technologies Rochester NY) using 445 nm laser illumination. 3 image stacks were collected on each treatment site. Fluorescein penetration was assessed semi-quantitatively through fluorescence intensity profiles calculated as follows: within-stack image registration was performed using Fiji's 'Register Virtual Stack Slices' algorithm, and two or three regions of interest (ROI's) were selected in each fluorescence image stack, taking care that the ROIs did not overlap with epidermal glyphics [131, 132]. The mean intensity, normalized by illumination laser power, was calculated as a function of depth for each ROI using Matlab (The Mathworks, Natick, MA). Average fluorescence intensity depth profiles for each treatment were calculated by first averaging the intensity at each depth in all ROI's per site and then averaging the site intensity depth profiles from all subjects. ATR-FTIR spectra were taken with a Thermo Nicolet Nexus 670 FTIR

Spectrometer, equipped with 2 x 0.2 inch ZnSe ATR crystal (Thermo Scientific, Waltham, MA) in Study 2. Two duplicate spectra were collected and averaged at each site with 128 scans and 4 cm^{-1} spectral resolution.

4.4 Results: Clinical Measures of Barrier Function

4.4.1 Topical Application of OA increases Transepidermal Water Loss

Epidermal barrier function was assessed in-vivo through TEWL measurements before and after topical treatments (Figure 4.1). Compared with the baseline TEWL value, no statistically significant change was detected after 24 hours in both the untreated sites and sites treated with 100% GT. However, TEWL at sites treated with OA or OA/GT mixtures increased significantly from the baseline level.

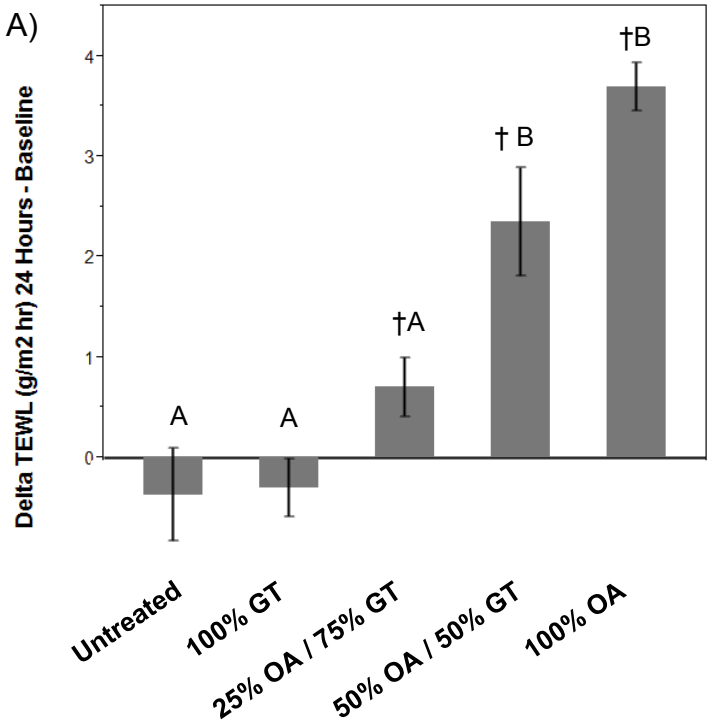

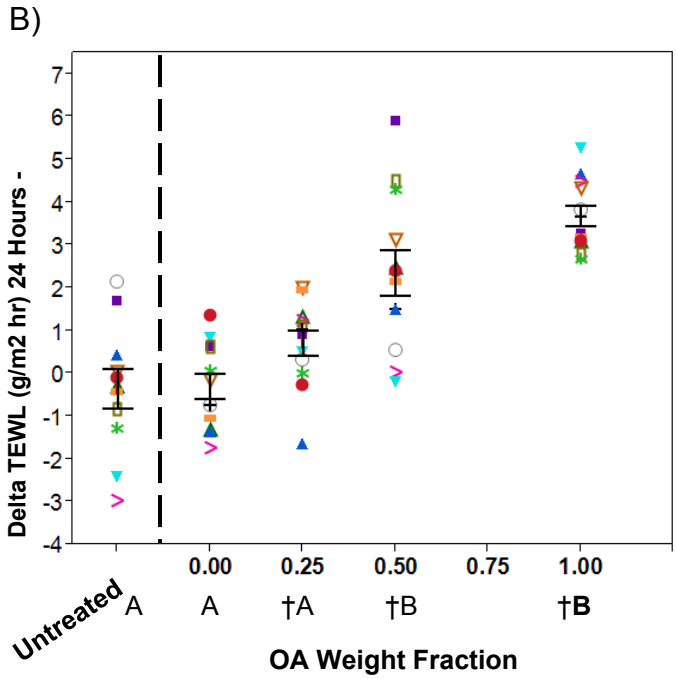

Figure 4.1 Application of Oleic Acid (OA), but not Glyceryl Trioleate (GT), Disrupts Skin Barrier Function.
A) Average changes in TEWL at untreated control sites and sites treated with OA, GT and their mixtures. TEWL increases over baseline values in sites treated with OA and OA/GT mixtures (†, $p<0.05$, paired t-test), but not in untreated sites and sites treated with 100% GT. The TEWL increase in sites treated with 100% OA and 50% OA / 50% GT is greater than that in sites treated with 25%OA / 75% GT, 100% GT, and untreated control (treatments not connected by the same letter are significantly different, one way ANOVA with Tukey's HSD post-test, $p<0.05$). Error bars represent 1 standard error of the mean (SEM). B) When GT is considered to be the vehicle, a dose response in change in TEWL with increasing weight fraction of OA is observed. Within subject trends follow trends observed in mean values (black circles represent the mean, and error bars represent 1 SEM). Reproduced with permission from [133] under the Creative Commons Attribution Non-Commercial License.

TEWL increases monotonically at sites treated with higher OA content (Figure 4.1A) indicating that OA disrupts the skin barrier and facilitates water transport. The change in TEWL after treatment with OA and 50%OA/50%GT was also found to be significantly higher than 25%OA/75% GT, 100% GT, and untreated control. Within subject changes in TEWL follow the same trend observed in mean values (Figure 4.1B).

4.4.2 OA Increases Penetration Potential of A Marker Compound

In order to assess the outside-in epidermal barrier function, the penetration of fluorescein dye into the skin after treatment was evaluated through fluorescence confocal microscopy. Average fluorescence intensity, normalized to the laser power used for image acquisition, decreased with depth into skin for all treatments (Figure 4.2). Fluorescence intensity was elevated versus control in all treated sites. Profiles increased with increasing OA fraction monotonically up to 30 μm.

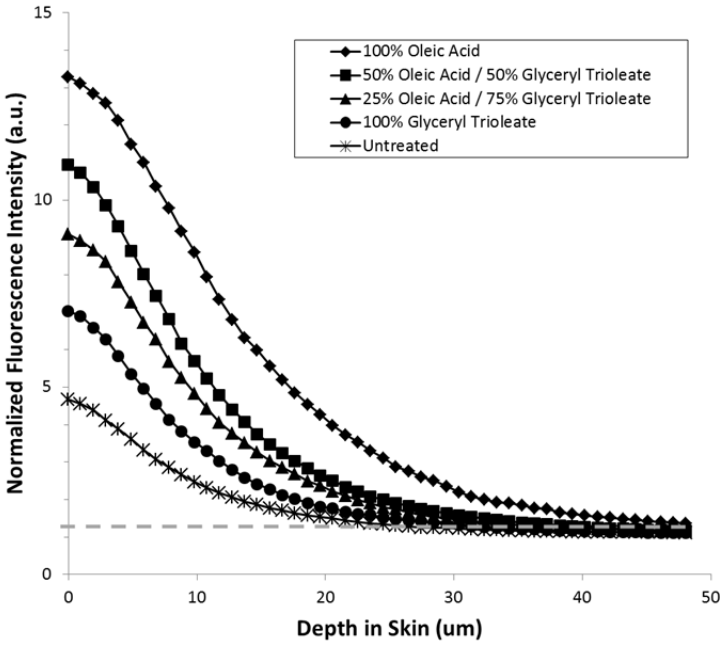

Figure 4.2 Penetration of Sodium Fluorescein is Measured in-vivo Through Fluorescence Confocal Microscopy.
Fluorescence intensity profile, normalized to laser power, is higher at the surface of the skin in sites treated with OA and OA/GT mixtures. Elevated fluorescence is observed throughout the stratum corneum and into the viable epidermis. Background signal is indicated by the grey dashed line. Reproduced with permission from [133] under the Creative Commons Attribution Non-Commercial License.

Strong fluorescence was observed at the cell outlines, presumably representing fluorescein dye primarily localized to the continuous lipid phase in the SC (Figure 4.3) and to the cell membranes in the viable epidermis (Figure 4.4), with subsequent diffusion into the keratin matrix of the corneocytes and cytoplasm of the keratinocytes. Differences in projected cell area in the viable epidermis were not observed between the treatments. Partially desquamated corneocytes also appeared to strongly fluoresce (Figure 4.3, green arrow). Dye also accumulated in the glyphics, serving as a secondary source for permeation (Figures 4.3 and 4.4, yellow arrowheads) [134].

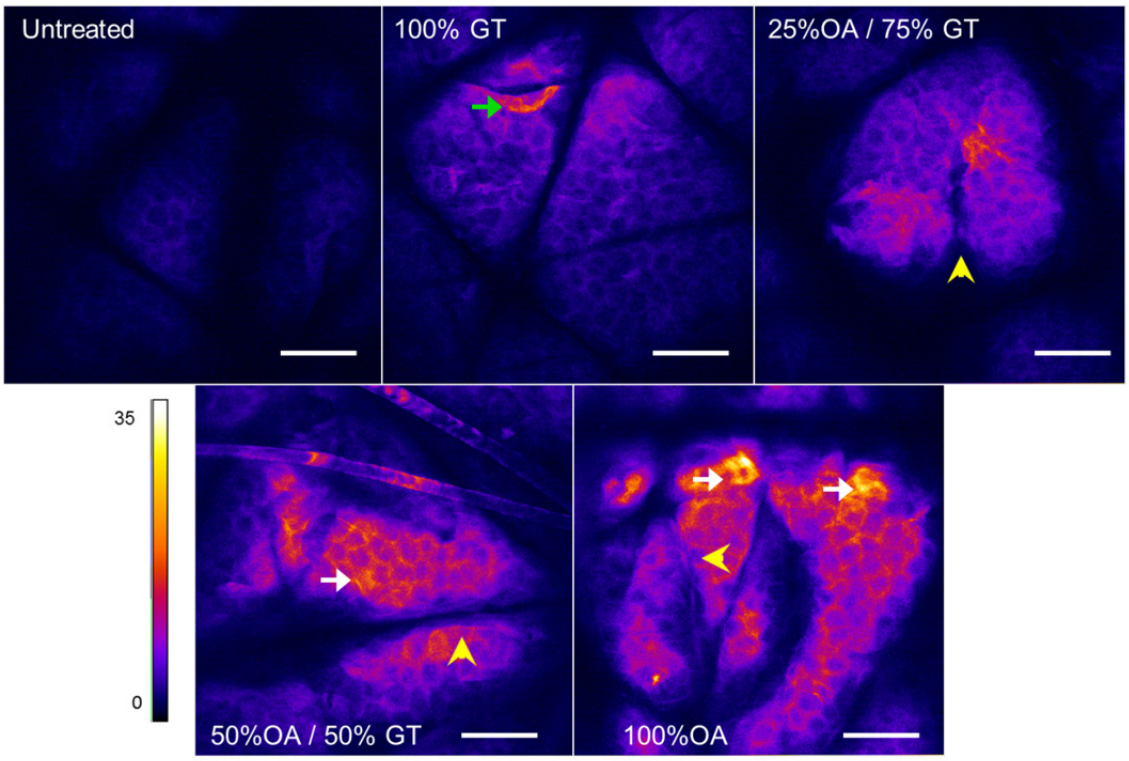

Figure 4.3 Representative Normalized Fluorescence Intensity Images at the Surface of the Stratum Corneum
Images at the surface of the SC were selected through visual inspection of representative image stacks. Localized areas of elevated fluorescence are observed at the surface of the skin (white arrows) and in clumps of partially desquamated corneocytes (green arrow). Fluorescence is not observed in the glyphics at the surface (yellow arrowheads). Scale

bars are 100 µm. Reproduced with permission from [133] under the Creative Commons Attribution Non-Commercial License.

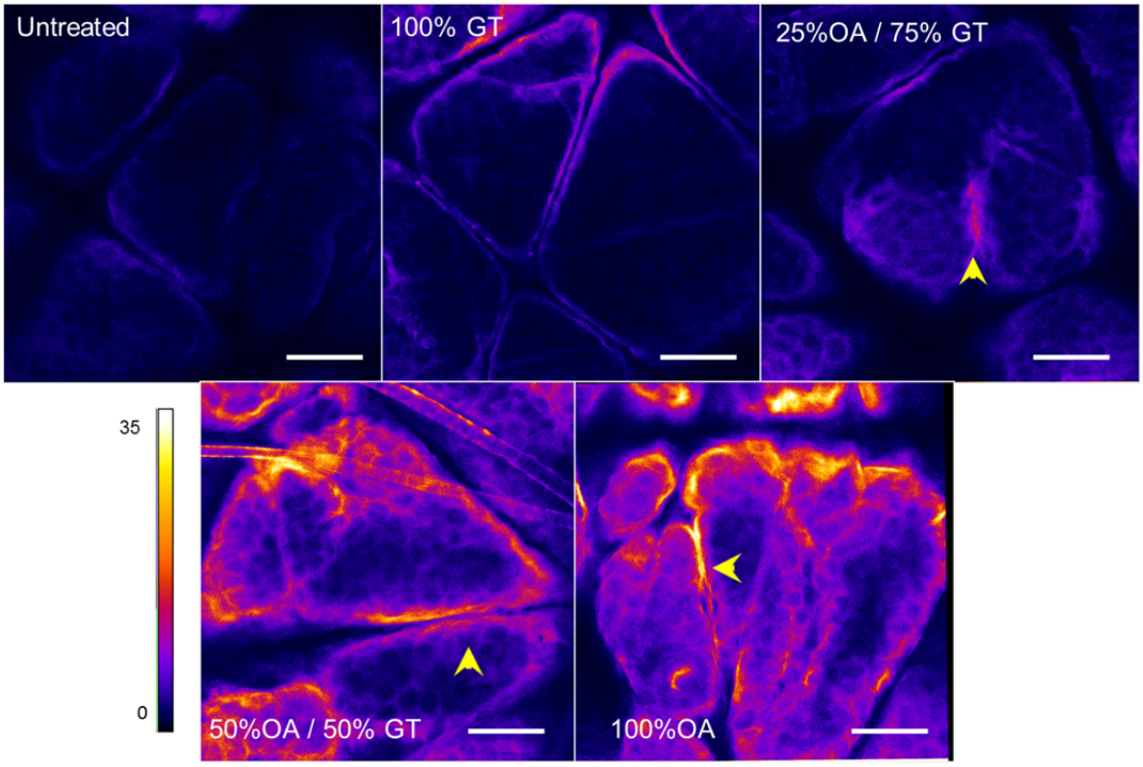

Figure 4.4 Representative Normalized Fluorescence Intensity Images of the Viable Epidermis (20µm into the skin)
Images at 20 µm into the skin were selected from the same representative stacks as shown in Figure 4.3. Fluorescence is observed in the bottom of glyphics, but not at the surface (yellow arrowheads). Scale bars are 100 µm. Reproduced with permission from [133] under the Creative Commons Attribution Non-Commercial License.

4.5 Results: Oleic Acid Disrupts Stratum Corneum Lipid Order in-vivo

Application of deuterated OA permitted monitoring both the OA-d_{34} penetration and SC lipid acyl chain order independently via ATR-FTIR. Because the IR beam only penetrates 1-2 µm into skin with the ZnSe ATR substrate and corneocytes are approximately 1 µm thick, spectra are derived from the top SC layers, averaged over a large lateral area [135,

136]. ATR-FTIR is therefore better suited to study the changes in SC lipid order before and after topical treatment, compared with the IR imaging approach, when spatial resolution is not required. The contact of the skin with the ATR plate influences overall spectral intensity, and in subsequent analyses band intensities were normalized to a peak of predominately protein (either Amide I or Amide II). Topically applied OA-d_{34} penetrated into the SC, confirmed by the presence of CD_2 stretching bands in spectra collected 24 hours after application (Figure 4.5A). The effects of OA-d_{34} on SC lipid order were monitored through both the CH_2 stretching band (Figure 4.5B) and CH_2 scissoring band (Figure 4.5C) [53, 137].

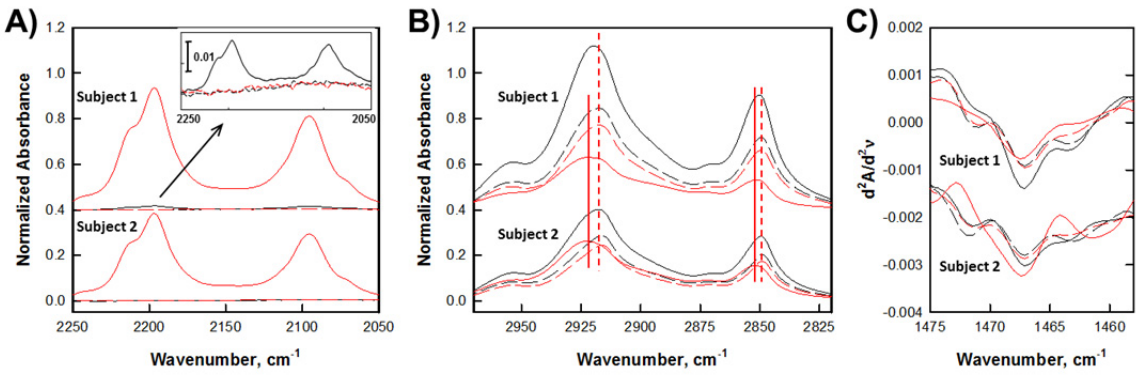

Figure 4.5 Effects of OA-d_{34} on the Endogenous Stratum Corneum Lipid Order. ATR-FTIR spectra, normalized to the Amide I band intensity, of untreated sites (black,control) and OA-d_{34} treated sites (red) before OA-d_{34} application (dashed lines) and 24 h after application (solid lines) in A) the CD_2 stretching region demonstrating OA-d_{34} penetration into skin, B) CH_2 stretching region and C) second derivative spectra of the CH_2 scissoring region. Inset in A) shows spectra of the CD_2 stretching region on a magnified scale to display the control site of subject 1, 24 h after treatment. The vertical red lines in B) indicate the peak position of the CH_2 stretching peaks before (dashed) and after (solid) treatment. The elevated peak position after treatment reflects more disordered alkyl chains in the SC lipids. Reproduced with permission from [133] under the Creative Commons Attribution Non-Commercial License.

The 24 hour in vivo treatment of OA-d_{34} shifted the CH_2 stretching bands to higher frequencies in both subjects (Figure 4.5B), indicating that OA-d_{34} disorders SC lipid acyl chains. OA-d_{34} also affected the lateral packing of SC lipids. Three peaks were observed in the second derivative spectra of the CH_2 scissoring band in both subjects before OA-d_{34} application (Figure 4.5C). The center peak at ~1467 cm^{-1} arises from SC lipids that are packed in hexagonal and liquid crystalline phases, while the two shoulders at ~1463 and ~1472 cm^{-1} are from orthorhombic phase [54]. After OA-d_{34} treatment (red solid lines), the two shoulders diminished while the center peak broadened, indicating the fraction of orthorhombic phase decreased. Overall, OA-d_{34} is observed to penetrate into SC in-vivo, disordering SC lipids and shifting their packing towards less densely packed phases.

A small amount of OA-d_{34} was detected in the control site of subject 1, (Figure 4.5A, inset), which may contribute to the small frequency shift observed in the 24 hour control site spectrum (Figure 4.5B). This trace amount of OA-d_{34} is likely due to lateral transport from the treated site to the adjacent control site.

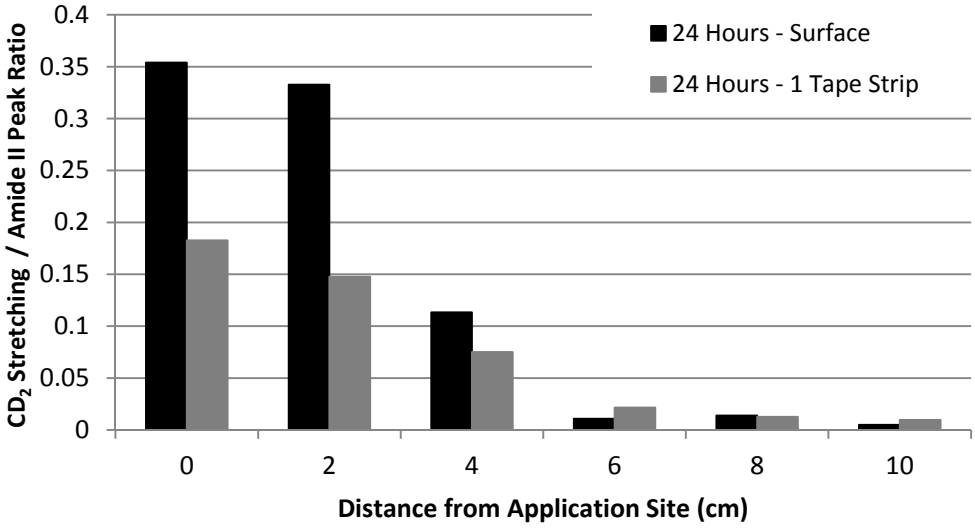

Figure 4.6 Lateral Transport of OA-d_{34} in-vivo after 24 Hours Exposure
The lateral transport of OA-d_{34} was measured through quantification of the CD_2 stretching band intensity, normalized to the Amide II band intensity, from ATR-FTIR spectra taken at the application site and at 2 cm intervals up to 10 cm from the application site. At each location, spectra were acquired, one tape strip was gently applied and removed, and a second set of spectra were acquired. OA-d_{34} was detectable both at the surface of the SC and after the removal of one tape strip up to 8 cm away from the application site.

Additional sites were measured to further investigate lateral transport, and diminishing concentrations of OA-d_{34} were observed up to 8 cm from the treatment site (Figure 4.6). In subject 2, the treated site and control site were placed on different arms to avoid this effect.

4.6 Discussion and Conclusions

Plant derived oils have been traditionally used as massage oils and have recently gained popularity in skin care formulations. Several studies have investigated the effects of plant oils as skin protectants [138, 139]. However, the presence of FFAs in plant oils and their associated skin penetration requires more thorough study. Herein, the effects of several OA/GT mixtures on skin barrier function were studied in vivo. The mixtures were found to disrupt both the inside-out (TEWL) and outside-in (fluorescein penetration) skin barrier functions in an OA dose dependent fashion. A single topical application of the mixtures with >25% OA was able to elevate TEWL and fluorescein penetration in 24 hours, suggesting that the occlusive effects of triglycerides, major components of plant oils, are not able to counteract the skin barrier disruption caused by FFAs. Further efforts should be devoted to elucidate the maximum FFA percentage in plant oil based formulations to guarantee safe repetitive topical application.

Despite the same acyl chain length and unsaturation level, OA and GT interact differently with SC lipids, penetrating skin to dissimilar depths (Supplemental Information, Figure 4.7). OA penetration was confirmed clinically, where it was observed to disorder lipid packing in the outer layers of the SC. Alternatively, the glycerol head group of GT presumably hinders the mobility and packing efficiency of GT. GT displayed minimal effects on skin barrier function, likely due to GT remaining at the surface of the skin (Supplemental Information, Figure 4.7).

In conclusion, we have demonstrated that OA penetrates into the skin and disorders the outer layers of SC lipids. This structural disruption in the SC lipids contributes to clinically measurable impaired barrier function. We also show that higher levels of OA lead to greater disruptions of the skin barrier. Taken together, this work demonstrates that application of advanced in-vivo skin measurement techniques may provide insight into the molecular interactions of exogenous materials with components of the skin barrier and corresponding changes in overall skin barrier function.

4.7 Supplemental Information

4.7.1 Subject Disposition and Analysis Dataset

Twelve subjects were enrolled in and completed the study. Confocal microscopy was performed on a subset of five subjects. The TEWL data presented represents the full dataset (n=12), and the fluorescein dye penetration results include the subset (n=5).

4.7.2 Ex-vivo Evaluation of OA and GT Permeation into Skin

The following work was performed in conjunction with that presented in the body of this chapter, and is included as supplemental information to aid in interpretation. The text and figure are reproduced with permission from [133] under the Creative Commons Attribution Non-Commercial License.

Human surgical abdominal skin (otherwise to be discarded) was obtained with informed consent and ethics board approval. Skin samples were tape stripped twice to remove surface sebum and attached to home-built Franz diffusion cells, 8mm in diameter, with the SC facing the donor chamber (Figure 4.7). Approximately 120 μL of OA-d_{34} or GT was added to the donor chamber while the receptor was left empty. Samples were incubated at 34°C for 24 hours. Excess liquid was removed after incubation and the skin surface was cleaned with cotton swabs. Skin sections, approximately 8 μm thick, were microtomed perpendicular to the skin surface for IR imaging.

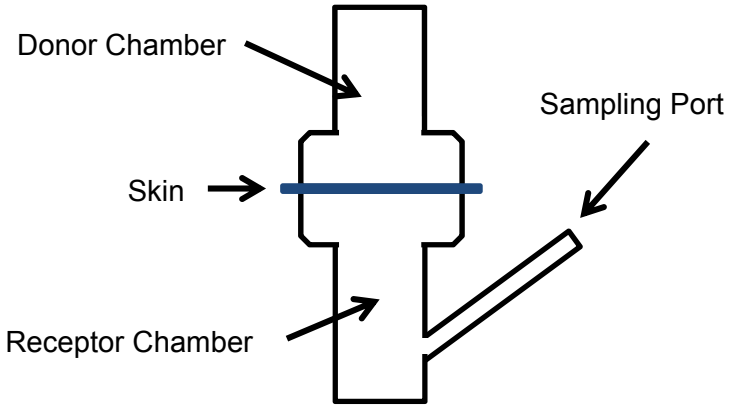

Figure 4.7 Diagram of Franz Diffusion Cell
For the ex-vivo permeation experiments, skin samples were placed in a Franz Diffusion Cell with the SC facing the donor chamber. The permeant (OA-d_{34} or GT) was added to the donor chamber and incubated at 34°C for 24 hours.

IR microspectroscopic images of skin cross-sections were collected with a PerkinElmer Spotlight 300 system (PerkinElmer Life and Analytical Sciences, Inc., Waltham, MA) [140]. 32 spectra with a spectral resolution of 4 cm^{-1} were averaged for each 6.25x6.25 µm pixel. Visible images of the sampled skin regions were acquired with the integrated microscope. Absolute concentrations of OA-d_{34} and GT were calculated with extinction coefficients determined from their respective octanolic solutions (Figure 4.8).

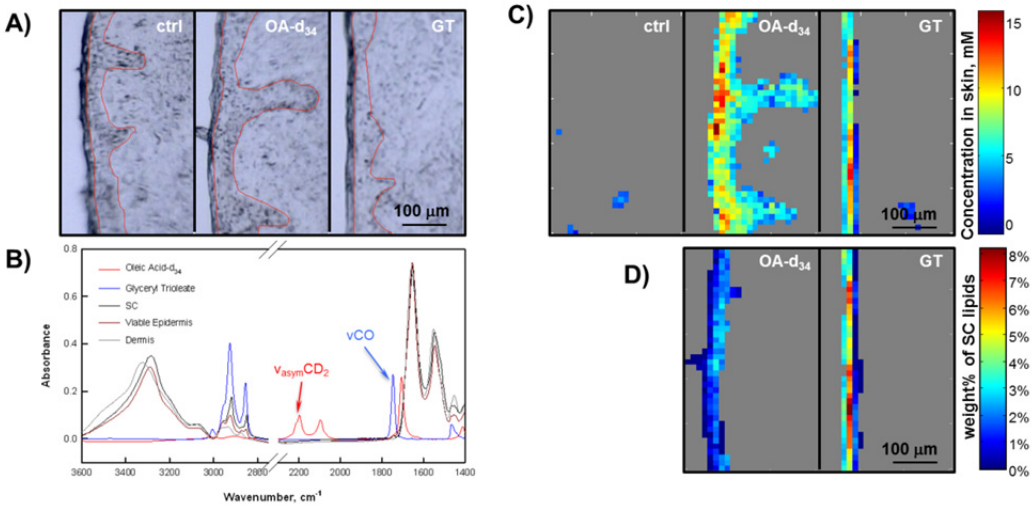

Figure 4.8 Detection of OA-d_{34} and GT Penetration Ex-vivo

A) Microscopic images of skin cross sections, with the SC located to the left of each image. The untreated control sample and samples treated with OA-d_{34} and GT are placed from left to right. The SC/viable epidermis and viable epidermis/dermis boundaries are outlined with thin red lines. B) IR spectra of pure OA-d_{34} (red), GT (blue), SC (black), viable epidermis (brown) and dermis (gray). The CD_2 asymmetric stretching peak at 2196 cm^{-1} ($\upsilon_{asym}CD_2$) was used for quantification of OA-d_{34} penetration. The CO stretching peak at 1742 cm^{-1}(υCO) was used for quantification of GT penetration. C) Images from the same sections shown in (a) of OA-d_{34} or GT concentration in untreated control, OA-d_{34} concentration in OA-d_{34} treated skin, and GT concentration in GT treated skin, left to

right, respectively. Detection limits were set with thresholds on the peak height at 2196 cm^{-1} or 1742 cm^{-1} to minimize detection in the untreated control sample, as no deuterated compounds and/or minimal amounts of esters (with sebum removed by tape stripping) were present in the untreated skin. D) Levels of OA-d_{34} and GT in SC regions expressed as the mass percentage of endogenous SC lipids**.** For visualization purposes, the viable epidermis and dermis are masked to highlight the differing concentrations of OA-d_{34} and GT in the SC.

These ex-vivo studies demonstrate that OA penetrates through the SC and into the viable epidermis whereas GT remains within the SC at the surface of the skin (Figure 4.8C). The OA-d_{34} penetration profile confirms the clinically observed penetration of OA-d_{34} into the SC shown in Figures 4.5 and 4.6, and further shows that OA penetrates into the viable epidermis. The molecular differences between OA and GT and their interaction with SC lipids likely plays a role in the differing penetration profiles observed ex-vivo and the different clinical effects on skin barrier function.

CHAPTER 5 In-Vitro Measures of Lipid Interactions Correlate to In-Vivo Effects on Skin Barrier

The materials, images and text used in this chapter have been previously published, at least in part, in Langmuir as an original manuscript (Guangru Mao, Dina VanWyck, Xin Xiao, M. Catherine Mack Correa, Euen Gunn, Carol R. Flach, Richard Mendelsohn, Russel M. Walters. "Oleic Acid Disorders Stratum Corneum Lipids in Langmuir Monolayers", Langmuir, 29:4857-65, 2013). This publication represents the original work of Mary Catherine Mack as a coauthor in collaboration with the first author and several coauthors as customary in this field of research. Mary Catherine Mack contributed the following to this publication: analysis of Brewster Angle Microscopy images and writing and/or editing the relevant sections of the manuscript.

5.1 Abstract

Oleic acid (OA) is well known to affect the function of the skin barrier. In this study, the interaction between OA and model stratum corneum (SC) lipids consisting of ceramide, cholesterol and palmitic acid (PA) was investigated with Langmuir monolayer and associated techniques. Mixtures with different OA/SC lipid compositions were spread at the air/water interface. The domain structure of the monolayers was studied through Brewster Angle Microscopy (BAM). Lower concentrations of OA were found to mix with and disorder the ceramide enriched domains. This was followed by perturbation of the PA enriched domains and disruption of SC lipid domain separation at higher OA levels.

5.2 Background and Objective

Previous work both in the literature and work described in Chapter 4 of this thesis have shown that OA penetrates into the skin and disrupts skin barrier function. OA has been shown to predominantly interact with SC lipids rather than keratin [141, 142], and therefore to further elucidate the mechanism of OA's disruption of skin barrier function, in-vitro experiments were performed to model interaction of OA with SC lipids.

Two mechanisms have been proposed to understand OA's interaction with SC lipids: disordering of SC lipids and formation of separate disordered OA enriched domains [143, 144]. Recent studies have shown that OA promoted phase separation in SC lipids [145] while molecular dynamic simulations suggested that OA reduced SC lipid bilayer density and thickness [146]. In these studies, the composition ratio between OA and SC lipids was not controlled or was only examined at a few values. As the composition ratio may impact the nature of the OA / SC lipid interaction, we investigated these interactions in a range of mixtures with OA both as a minor component and as the major component.

An equimolar mixure of ceramide, cholesterol, and palmitic acid (PA) was used as a model for SC lipids has been previously described [50, 52, 147, 148]. Additional mixtures were prepared by incorporating OA at mole fractions of 0.1 – 0.9. The SC lipid mixture alone and OA alone were also included as controls. Miscibility and phase behavior of the OA / SC lipid mixtures were investigated with Langmuir monolayers and domain morphology was directly visualized through Brewster Angle Microscopy (BAM) [149]. When the bare air/water interface is illuminated with p-polarized light at the

Brewster angle, no reflection occurs and the water surface appears black. When the refractive index is modified by the presence of a lipid monolayer, contrast arises. Different levels of brightness can also be observed within films from regions that vary in density or thickness, resultant from molecular interactions and/or acyl chain orientation. Monolayers and domain structure can thus be visualized through BAM [150, 151].

The objective of this work was to investigate the mechanism by which OA disrupts skin barrier function through imaging the domain structure of OA / SC lipid mixtures.

5.3 Materials and Methods

5.3.1 Materials

Bovine brain ceramide (type III), cholesterol, PA, and OA were purchased from Sigma Aldrich (St. Louis, MO). The ceramide belongs to the NS ceramide family with nonhydroxy fatty acid chains composed predominantly of stearic acid (C18:0) and nervonic acid (C24:1) attached to a sphingosine headgroup through an amide bond. Sodium chloride, ethylenediaminetetraacetic acid (EDTA), and chloroform were purchased from Fisher Scientific (Hampton, NH). All lipids were dissolved separately in chloroform at ~1.00 mg/mL; individual solutions were combined volumetrically to make the mixed solutions desired. Mixtures containing OA are referenced by their molar percentages of OA.

5.3.2 Monolayer Measurements

A KSV NIMA Langmuir trough (KN1006, Biolin Scientific, Sweden) was used to acquire surface pressure-mean molecular area (π-A) isotherms. In the context of Langmuir monolayer measurements, surface pressure is the difference in surface tension between the pure subphase and the subphase with monolayer, and is reported as force per unit length [152]. Monolayers were floated on a subphase of 150 mM NaCl and 1 mM EDTA adjusted to pH 5.5. Typically, ~60-80 μL of ~1 mg/mL lipid/chloroform solution was spread at air/water interface, and 15 minutes were allowed for solvent evaporation. Monolayers were then compressed with a constant barrier speed of ~4 $Å^2$/molecule/min until collapse. During compression, mean molecular area (MMA) was calculated as the area per molecule applied in the monolayer.

5.3.3 Brewster Angle Microscopy

A high-resolution KSV NIMA BAM microscope (Biolin Scientific, Vaëstra Fröluna, Sweden) was aligned to the trough center to view images of monolayers at 20 frames/s with a field of view of 720 μm (W) × 400 μm (H) and 2 μm resolution. The angle of incidence was set at 53.2°, and the polarizer and analyzer were both set to polarization at 0° for best image contrast. BAM videos were recorded during continuous film compression simultaneously with π−A isotherm collection. Image frames at selected surface pressures were captured from the videos with Accurion Image (Accurion GmbH, Goettingen, Germany) and presented with brightness adjusted upward to the same level for all of the images with Adobe Photoshop for best visualization.

5.4 Results

OA's impact on domain formation within SC monolayers was investigated through BAM. At the beginning of film compression, lipids are in a gaseous phase and the interface with low lipid density appears black. With further barrier movement, the density and acyl chain order of the lipids increases and the monolayer is visualized. BAM images for SC lipids at surface pressures of 1, 5, 10 and 30 mN/m are shown in the first row of Figure 4.1. The entire field of view was soon covered with a condensed film of SC lipids as shown in Figure 4.1A1. A few small defects in the monolayer appeared in black (white arrows, Figure 4.1A1), showing the exposed air/water (a/w) interface. The high resolution of the BAM system utilized in our investigations enabled visualization of morphological details of the aqueous SC lipid monolayer films. To our knowledge, we are the first to report on these morphological aspects of SC lipid monolayer films.

SC lipids do not form a uniform film at the a/w interface. Domains with irregular branch-like structures in bright gray color (domain A) are observed to be dispersed in a darker continuous domain (domain B). With further compression, the area of domain B contracted and the density of domain A was observed to increase with surface pressure (as shown in Figures 5.1A1-4). Figures 5.1H1-4 depict BAM images obtained from pure OA monolayers.

Adding 10% to 30% OA to SC lipids did not dramatically modify monolayer morphology but decreased the coverage of domain A and slightly increased the uniformity of its dispersion in domain B (Figures 5.1B, 5.1C, and 5.1D). With 20 and 30% OA in the mixture, an additional, very dark domain (domain C) under the BAM was observed at low surface pressures (Figures 5.1C1 and Figures 5.1D1-D3). Domain C was nearly black, but could be differentiated from the exposed a/w interface observed at the beginning of monolayer compression. Domain C soon disappeared with compression at 5mN/m and 20 mN/m, respectively, for mixtures containing 20% and 30% OA. The percentage of domain C's surface coverage and sustainable surface pressure increased with OA concentration (up to 30%) and thus it is possibly an OA enriched domain.

At 40% OA (Figures 5.1E1-4), the monolayer mixture still displayed phase separation into the bright domain A and darker domain B; however, the bright domains were well separated and had either a snowflake or circular shape. Similar to the other mixtures, the density of the bright domains increased with surface pressure. When the OA concentration increased to 60%, the initial domain structure (Figure 5.1F1) observed at 1mN/m disappeared upon compression to 5 mN/m (Figure 5.1F2). Bright circular domains appeared at 10mN/m (Figure 5.1F3) and their size and density increased with further compression (Figure 5.1F4). At 80% OA, only a few, faint structures were observed at 1 mN/m (Figure 5.1G1) and at 5 mN/m (Figure 5.1G2). No contrast was observed at higher surface pressures and black surfaces were observed as shown in Figures 5.1G3 and 4, similar to the OA monolayer (Figure 5.1H).

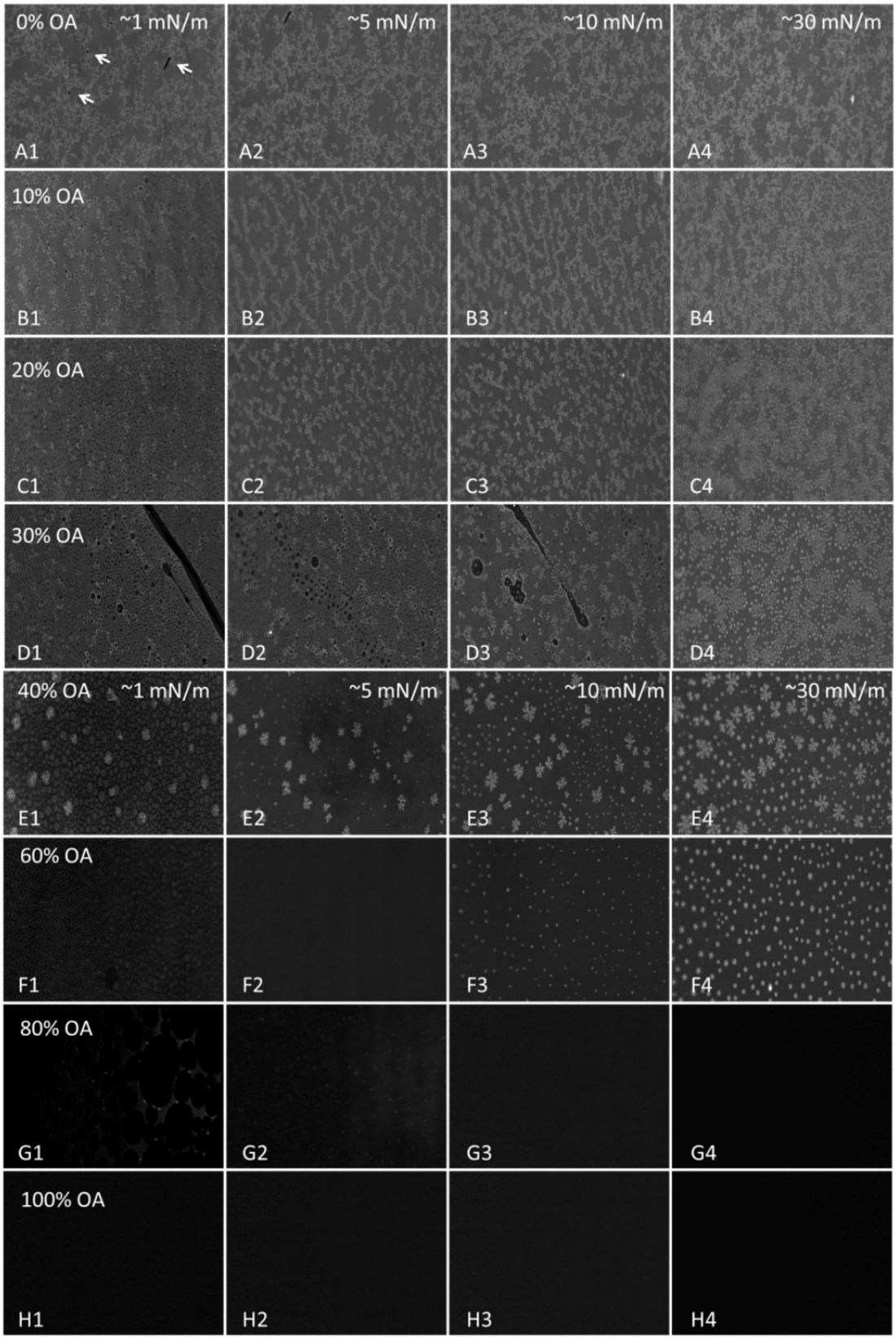
0% OA
~1 mN/m
A1
~5 mN/m
A2
~10 mN/m
A3
~30 mN/m
A4
10% OA
B1
B2
B3
B4
20% OA
C1
C2
C3
C4
30% OA
D1
D2
D3
D4
40% OA
~1 mN/m
E1
~5 mN/m
E2
~10 mN/m
E3
~30 mN/m
E4
60% OA
F1
F2
F3
F4
80% OA
G1
G2
G3
G4
100% OA
H1
H2
H3
H4

Figure 5.1 BAM images for Cer/Chol/PA, OA, and their mixtures at different surface pressures.
The phase behavior of a model mixture of SC lipids with varying concentration of OA was investigated through Brewster Angle Micrsocopy as monolayers of the lipid mixtures were compressed on a Langmuir trough. The OA concentration and surface pressures are noted on the images. The actual size of each image is 720 μm (W) × 400 μm. Reprinted with permission from Mao et al, Langmuir 2013 **29**(15): p. 4857-65. Copyright 2013 American Chemical Society.

To quantitatively assess the impact of addition of OA to SC lipids on monolayer phase behavior, the percent surface coverage of domain A was calculated from BAM images collected during compression of monolayers containing 0-60% OA (Figure 5.2).

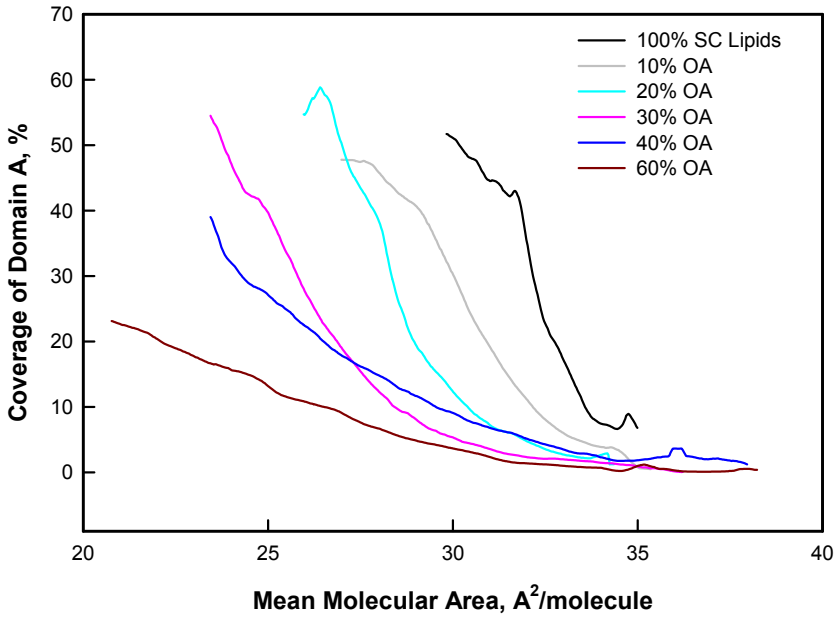

Figure 5.2 Surface Coverage of Domain A Decreases with Increasing MMA and OA Content
Percent Surface Coverage of Domain A as Function of Mean Molecular Area in monolayers of SC lipids (black line) and its mixtures with OA (mole percent) at 10% gray line), 20% (cyan line), 30% (magenta line), 40% (blue line) and 60% (brown line). Reprinted with permission from [149] Mao et al, Langmuir **29**(15): p. 4857-65. Copyright 2013 American Chemical Society.

To calculate the percent surface coverage, a gray level threshold that optimally separated domains A and B was selected for each BAM image stack based on visual assessment. Percent surface coverage of domain A was calculated as the ratio of the number of pixels with gray levels higher than the threshold to the total number of pixels in the image. A running average of the percent surface coverage of domain A over 30 neighboring frames was calculated and the mean values from two separate experiments at each OA level are plotted as a function of MMA in Figure 5.2. Percent surface coverage of domain A was not calculated for monolayers containing 80% OA or pure OA as the domain structure was not observed at surface pressures greater than 5 mN/m (Figure 5.1G-H).

The percent surface coverage of domain A increased with compression (lower MMA) for all the monolayers. However, the slope of percent surface coverage increase was dependent on the amount of OA in the film and significantly lower coverages were observed for monolayers containing 40% and 60% OA.

5.5 Discussion and Conclusions

Due to the lack of chemical identification in BAM images, the composition of domains A and B cannot be ascertained directly. An assignment is suggested below. In earlier studies, domain separation between ceramides and free fatty acids was observed with ^{2}H-NMR and IR measurements in SC lipid dispersions [50, 153, 154]. Additional experiments performed in conjunction with the Langmuir monolayer and BAM imaging presented in this chapter also suggest that in the SC lipid model system, ceramide and PA

exist in separate domains [149]. Since domain brightness observed by BAM is affected by lipid density and packing, it seems reasonable to assume that the more densely packed and more ordered PA is enriched in the bright domain A and the relatively less ordered ceramide is enriched in the more compressible domain B.

When OA was added to the mixture, it first incorporated into the ceramide enriched domains, increasing the fluidity of this domain and altering domain morphology. When the OA concentration increased to 40 mole % or above, OA started to disrupt the PA enriched, more ordered domains. Once the concentration of OA reached 80 mole %, SC lipids were completely dissolved in OA and no phase separation was observed with the BAM.

In this study, aqueous monolayers of equimolar mixtures of ceramide, cholesterol and PA were adopted to mimic a single layer of intercellular SC lipid lamellae. Model SC lipids were observed to form domains enriched in either ceramide or PA. OA was observed to preferentially mix with and disorder ceramide at low concentrations and at high concentrations to interact with PA and thus to disrupt SC domain separation. Ceramides are known to play a role in development of the SC lipid structure necessary to maintain skin barrier integrity, and therefore disordering of ceramide enriched lipid domains would likely reduce the functional integrity of the SC lipid barrier [52, 109, 155]. These results provide a mechanistic understanding of OA interaction with components of the skin barrier, which underlies the clinical findings in Chapter 4 of skin barrier disruption due to application of OA.

The methods presented in this chapter may be used to discern the mechanism of action of other compounds known to enhance penetration or disrupt the skin barrier. Further evaluation of the surface coverage of different domains as a function of MMA with additional compounds may enable identification of a quantitative relationship between these parameters.

CHAPTER 6 Dissertation Discussion

This work investigates the impact on overall skin barrier function of morphological features of the epidermis at the microscopic and molecular level. Microscopic level epidermal morphology (thickness of the cell layers and cell area) and molecular structural morphology (ordering of the stratum corneum, SC, lipid lamellae) are evaluated separately. This work lays the foundation for future studies to further elucidate the mechanisms which ultimately create the permeability barrier of the skin. Future studies which integrate measures of epidermal morphology at both the microscopic and molecular levels and correlate these endpoints to macroscopic functional parameters of the skin barrier will enable assessment of the relative contribution of each.

Through evaluation of theoretical and in-use resolution limits, we evaluated the suitability of the VivaScope to measure microscopic parameters related to skin barrier function. Lateral and axial resolution limits were compared for the three laser wavelengths available for use in the VivaScope, and we found that the practically achievable resolution limits would enable measurements of SC thickness, keratinocyte size within the viable epidermis, and thickness of the viable epidermis.

Additionally, through this work we have expanded the in-vivo, noninvasive methodologies to assess skin barrier function through identification of quantitative parameters of epidermal morphology measurable through confocal microscopy. We demonstrated that the thicknesses of the SC and viable epidermis may be used to monitor the balance of proliferation, differentiation, and desquamation, providing insight into

epidermal homeostasis. We also show that cell area of the stratum granulosum (SG) and stratum spinosum (SS) layers may be used as additional quantitative measures of proliferative state.

We investigated skin barrier recovery after mechanical disruption of the SC through tape stripping, and application of the measures described above generated new insights into the processes underlying maintenance and repair of the skin barrier function. Immediate changes in epidermal morphology were observed after skin barrier disruption, which potentially is the first in-vivo documentation of lamellar body degranulation. We found that the kinetics of recovery of barrier function are different with moderate disruption versus full removal of SC, which has been previously unreported. We showed that both transepidermal water loss (TEWL) and SC thickness recovered linearly with time after a moderate disruption, and the barrier was not fully recovered to baseline parameters after one week.

The impact of morphology at the molecular level on skin barrier function was investigated through use of infrared spectroscopy to assess conformation order and lateral packing of SC lipids. We showed that disruption of the molecular order of SC lipids results in disruption of the permeability barrier function. Oleic acid was shown to penetrate into the SC and disorder SC lipids, and the topical application of oleic acid resulted in elevated TEWL and dye penetration into the skin. Glyceryl trioleate, which is chemically similar to oleic acid but contains three oleic fatty acid chains, remained at the surface of the SC and did not disrupt skin barrier function. Application of mixtures of the

two compounds resulted in barrier function disruption that was dose dependent on oleic acid concentration.

The mechanism of OA barrier disruption was investigated through Langmuir monolayers and Brewster Angle Microscopy. Oleic acid mixed with and fluidized SC lipids, and monitoring domain morphology of the monolayers showed that OA preferentially mixed with the less ordered ceramide enriched domains at OA levels of less than 40 mole percent.

The work presented in this thesis suggests several areas for future research. The impact of epidermal morphology at the cellular level on overall skin barrier function may be further probed through studies of disease states and treatment effects. Investigation of the kinetics of skin barrier recovery, including both morphological and functional endpoints, after mild, moderate, and severe disruptions would provide insight into mechanisms by which the scale of barrier disruption determines recovery kinetics.

Further insights around the impact of SC lipid order on skin barrier function may be investigated through application of different stimuli to disrupt lipid molecular order, for example heating the skin. Additionally, measurement of the depth dependence of lipid order within the SC may potentially identify the SC layers which are most important to barrier.

Finally, integration of the methodologies presented in this thesis to investigate both cellular and molecular morphology in the SC and viable epidermis would allow for better understanding of the contribution of each to overall skin barrier function. This understanding would facilitate the assessment of the causes of barrier dysfunction in disease states and may lead to targeted therapies based on disease etiology.

The methodologies developed in this work have been shown to enable quantitative assessment of the constitutive elements of skin barrier and their impact on function. These methodologies may be further applied to investigations into the mechanisms of barrier function development and repair, dermatological disease pathology, and treatment effects.

REFERENCES

1. Lippens, S., et al., *Epidermal differentiation does not involve the pro-apoptotic executioner caspases, but is associated with caspase-14 induction and processing.* Cell Death and Differentiation, 2000. **7**(1218-1224).

2. Segre, J.A., *Epidermal barrier formation and recovery in skin disorders.* Journal of Clinical Investigation, 2006. **116**: p. 1150-1158.

3. Fuchs, E., *Epidermal differentiation: The bare essentials.* Journal of Cell Biology, 1990. **111**(6): p. 2807-2814.

4. Bergstresser, P.R., R.J. Pariser, and J.R. Taylor, *Counting and sizing of epidermal cells in normal human skin.* J Invest Dermatol, 1978. **70**(5): p. 280-4.

5. Stamatas, G.N., et al., *Infant skin microstructure assessed in-vivo differs from adult skin in organization and at the cellular level.* Pediatric Dermatology, 2010. **27**(2): p. 125-131.

6. Norlen, L., *Stratum corneum keratin structure, function and formation - a comprehensive review.* Int J Cosmet Sci, 2006. **28**(6): p. 397-425.

7. Rawlings, A.V., *Recent advances in skin 'barrier' research.* Journal of Pharmacy and Pharmacology, 2010. **62**: p. 671-677.

8. Elias, P.M. and G.K. Menon, *Structural and lipid biochemical correlates of the epidermal permeability barrier.* Advances in Lipid Research, 1991. **24**: p. 1-26.

9. van Smeden, J., et al., *The important role of stratum corneum lipids for the cutaneous barrier function.* Biochimica et Biophysica Acta (BBA) - Molecular and Cell Biology of Lipids, 2014. **1841**(3): p. 295-313.

10. Bouwstra, J.A., et al., *Structural investigations of human stratum corneum by small-angle x-ray scattering.* Journal of Investigative Dermatology, 1991. **97**(6): p. 1005-1012.

11. Forslind, B., *A domain mosaic model of the skin barrier.* Acta Dermato-Venereologica, 1994. **74**(1): p. 1-6.

12. Forslind, B., et al., *A novel approach to the understanding of human skin barrier function.* Journal of Dermatological Science, 1997. **14**(2): p. 115-125.

13. Damien, F. and M. Boncheva, *The extent of orthorhombic lipid phases in the stratum corneum determines the barrier efficiency of human skin in-vivo.* Journal of Investigative Dermatology, 2010. **130**: p. 611-614.

14. Schreiner, V., et al., *Barrier characteristics of different human skin types investigated with x-ray diffraction, lipid analysis, and electron microscopy imaging.* Journal of Investigative Dermatology, 2000. **114**: p. 654-660.

15. Kirschner, N., et al., *Tight junctions: is there a role in dermatology?* Arch Dermatol Res, 2012. **302**(7): p. 483-93.

16. Madison, K.C., *Barrier function of the skin: "La raison d'etre" of the epidermis.* Journal of Investigative Dermatology, 2003. **121**: p. 231-241.

17. Guttman-Yassky, E., et al., *Broad defects in epidermal cornification in atopic dermatitis identified through genomic analysis.* Journal of Allergy and Clinical Immunology, 2009. **124**: p. 1325-1244.

18. Hirao, T., M. Denda, and M. Takahashi, *Identification of immature cornified envelopes in the barrier-impaired epidermis by characterization of their hydrophobicity and antigenicities of the components.* Exp Dermatol, 2001. **10**(1): p. 35-44.

19. Agache, P. and P. Humbert, eds. *Measuring the skin*. 2004, Springer-Verlag: Berlin.

20. Okah, F.A., et al., *Surface electrical capacitance as a noninvasive bedside measure of the epidermal barrier function in the newborn infant.* Pediatrics, 1995. **96**(4): p. 688-692.

21. Shah, J.H., H. Zhai, and H. Maibach, *Comparative evaporimetry in man.* Skin Research and Technology, 2005. **11**: p. 205-208.

22. Zonios, G., J. Bykowski, and N. Kollias, *Skin melanin, hemoglobin, and light scattering properties can be quantitatively assessed in-vivo using diffuse reflectance spectroscopy.* Journal of Investigative Dermatology, 2001. **117**: p. 1452-1457.

23. Vogt, M. and H. Ermert, *High-Resolution Ultrasound*, in *Bioengineering of the Skin: Skin Imaging and Analysis*, K.P. Wilhelm, et al., Editors. 2006, CRC Press: Boca Raton.

24. Bachmann, A., R. Leitgeb, and T. Lasser, *Heterdyne Fourier domain optical coherence tomography for full range probing with high axial resolution.* Optics Express, 2006. **14**(4): p. 1487-1496.

25. Konig, K., et al., *Clinical optical coherence tomography combined with multiphoton tomography of patients with skin diseases.* Journal of Biophotonics, 2009. **2**(6-7): p. 389-397.

26. Li, Y., et al., *Dual mode reflectance and fluorescence confocal laser scanning microscopy for in vivo imaging melanoma progression in murine skin.* Journal of Investigative Dermatology, 2005. **125**: p. 798-804.

27. Rajadhyaksha, M., et al., *In-vivo confocal scanning laser microscopy of human skin II: advances in instrumentation and comparison with histology.* Journal of Investigative Dermatology, 1999. **113**: p. 293-303.

28. Rajadhyaksha, M., et al., *In vivo confocal scanning laser microscopy of human skin: melanin provides strong contrast.* Journal of Investigative Dermatology, 1995. **104**: p. 946-952.

29. Swindle, L.D., et al., *View of normal skin in-vivo as observed using fluorescent fiber-optic confocal microscopic imaging.* Journal of Investigative Dermatology, 2003. **121**: p. 706-712.

30. White, J.G., W.B. Amos, and M. Fordham, *An evaluation of confocal versus conventional imaging of biological structures by fluorescence light microscopy.* Journal of Cell Biology, 1987. **105**: p. 41-48.

31. Peppelman, M., et al., *Combining tape stripping and non-invasive reflectance confocal microscopy : an in vivo model to study skin damage.* Skin Res Technol, 2015.

32. Astner, S., et al., *Clinical applicability of in-vivo fluorescence confocal microscopy for noninvasive diagnosis and theraputic monitoring of nonmelanoma skin cancer.* Journal of Biomedical Optics, 2008. **13**(1): p. 014003.

33. Scope, A., et al., *In vivo reflectance confocal microscopy of shave biopsy wounds: feasibility of intra-operative mapping of cancer margins.* British Journal of Dermatology, 2010. **Epub ahead of print**.

34. Astner, S., et al., *Non-invasive evaluation of the kinetics of allergic and irritant contact dermatitis.* Journal of Investigative Dermatology, 2005. **124**(351-359).

35. Astner, S., et al., *Preliminary evaluation of benign vascular lesions using in vivo reflectance confocal microscopy.* Dermatologic Surgery, 2010. **36**: p. 1099-1110.

36. Stumpp, O.F., et al., *In-vivo confocal imaging of epidermal cell migration and dermal changes post nonablative fractional resurfacing: study of the wound healing process with corroborated histopathologic evidence.* Journal of Biomedical Optics, 2009. **14**(2): p. 024018.

37. Manfredini, M., et al., *Acne: in vivo morphologic study of lesions and surrounding skin by means of reflectance confocal microscopy.* J Eur Acad Dermatol Venereol, 2015. **29**(5): p. 933-9.

38. Longo, C., et al., *Skin aging: in vivo microscopic assessment of epidermal and dermal changes by means of confocal microscopy.* J Am Acad Dermatol, 2013. **68**(3): p. e73-82.

39. Longo, C., et al., *Proposal for an in vivo histopathologic scoring system for skin aging by means of confocal microscopy.* Skin Res Technol, 2013. **19**(1): p. e167-73.

40. Mack, M.C., G.N. Stamatas, and P. Horowitz, *Micronized sunscreen particles were not shown to penetrate beyond the stratum corneum in adults or children.* Journal of Investigative Dermatology, 2010. **130**(Supplement 1): p. S44.

41. Vergou, T., et al., *Comparison between TEWL and laser scanning microscopy measurements for the in vivo characterization of the human epidermal barrier.* J Biophotonics, 2012. **5**(2): p. 152-8.

42. Bargo, P.R., et al., *Non-invasive assessment of tryptophan fluorescence and confocal microscopy provide information on skin barrier repair dynamics beyond TEWL.* Exp Dermatol, 2013. **22**(1): p. 18-23.

43. Robertson, K. and J.L. Rees, *Variation in epidermal morphology in human skin at different body sites as measured by reflectance confocal microscopy.* Acta Derm Venereol, 2010. **90**(4): p. 368-73.

44. Neerken, S., et al., *Characterization of age-related effects in human skin: A comparative study that applies confocal laser scanning microscopy and optical coherence tomography.* Journal of Biomedical Optics, 2004. **9**(2): p. 274-281.

45. Somoza, E., et al., *Automatic Localization of Skin Layers in Reflectance Confocal Microscopy*, in *Image Analysis and Recognition*, A. Campilho and M. Kamel, Editors. 2014, Springer International Publishing. p. 141-150.

46. Caspers, P.J., et al., *Automated depth-scanning confocal raman microspectrometer for rapid in-vivo determination of water concentration profiles in human skin.* Journal of Raman Spectroscopy, 2000. **31**: p. 813-818.

47. Caspers, P.J., et al., *In-vivo confocal Raman microspectroscopy of the skin: noninvasive determination of molecular concentration profiles.* Journal of Investigative Dermatology, 2001. **116**: p. 434-442.

48. Zhang, G., et al., *Vibrational microscopy and imaging of skin: from single cells to intact tissue.* Analytical and Bioanalytical Chemistry, 2007. **387**(5): p. 1591-1599.

49. Mendelsohn, R., C.R. Flach, and D.J. Moore, *Determination of molecular conformation and permeation in skin via IR spectroscopy, microscopy, and imaging.* Biochimica et Biophysica Acta (BBA) - Biomembranes, 2006. **1758**(7): p. 923-933.

50. Moore, D.J., M.E. Rerek, and R. Mendelsohn, *Lipid Domains and Orthorhombic Phases in Model Stratum Corneum: Evidence from Fourier Transform Infrared Spectroscopy Studies.* Biochemical and Biophysical Research Communications, 1997. **231**(3): p. 797-801.

51. Groen, D., et al., *Is an orthorhombic lateral packing and a proper lamellar organization important for the skin barrier function?* Biochim Biophys Acta, 2011. **1808**(6): p. 1529-37.

52. Moore, D.J., M.E. Rerek, and R. Mendelsohn, *Role of ceramides 2 and 5 in the structure of the stratum corneum lipid barrier.* International Journal of Cosmetic Science, 1999. **21**: p. 353-368.

53. Saad, P., et al., *Infrared spectroscopic studies of sodium dodecyl sulphate permeation and interaction with stratum corneum lipids in skin.* Int J Cosmet Sci, 2012. **34**(1): p. 36-43.

54. Boncheva, M., F. Damien, and V. Normand, *Molecular organization of the lipid matrix in intact Stratum corneum using ATR-FTIR spectroscopy.* Biochim Biophys Acta, 2008. **1778**(5): p. 1344-55.

55. Denda, M., et al., *Stratum corneum lipid morphology and transepidermal water loss in normal skin and surfactant-induced scaly skin.* Arch Dermatol Res, 1994. **286**(1): p. 41-6.

56. Altintas, M.A., et al., *Reflectance confocal-laser-scanning microscopy in-vivo assessments of cigarette-induced dynamic alterations of cutaneous microcirculation on histomorphological level.* Microscopy Research and Technique, 2009. **72**: p. 347-350.

57. Scope, A., et al., *In vivo reflectance confocal microscopy of shave biopsy wounds: feasibility of intra-operative mapping of cancer margins.* British Journal of Dermatology, 2010. **163**(6): p. 1218-28.

58. Ulrich, M., S. Lange-Asschenfeldt, and S. Gonzalez, *In vivo reflectance confocal microscopy for early diagnosis of nonmelanoma skin cancer.* Actas Dermosifiliogr, 2012. **103**(9): p. 784-9.

59. Ulrich, M., S. Lange-Asschenfeldt, and S. Gonzalez, *Clinical applicability of in vivo reflectance confocal microscopy in dermatology.* G Ital Dermatol Venereol, 2012. **147**(2): p. 171-8.

60. Olivo, M., R. Bhuvaneswari, and I. Keogh, *Advances in bio-optical imaging for the diagnosis of early oral cancer.* Pharmaceutics, 2011. **3**(3): p. 354-78.

61. Mertz, J., *Introduction to Optical Microscopy*. 2010, Greenwood Village, CO: Roberts and Company Publishers.

62. Wilson, T. and A.R. Carlini, *Size of the detector in confocal imaging systems.* Optics Letters, 1987. **12**(4): p. 227-229.

63. Wilson, T. and C.J.R. Sheppard, *Theory and Practice of Scanning Optical Microscopy*. 1984, London: Academic Press Inc.

64. Cox, G. and C.J. Sheppard, *Practical limits of resolution in confocal and non-linear microscopy.* Microsc Res Tech, 2004. **63**(1): p. 18-22.

65. Bevan, A., *Statistical Data Analysis for the Physical Sciences*. 2013: Cambridge University Press.

66. Swindells, K., et al., *Reflectance confocal microscopy may differentiate acute allergic and irritant contact dermatitis in vivo.* Journal of the American Academy of Dermatology, 2004. **50**(2): p. 220-228.

67. Skvara, H., et al., *Combining in vivo reflectance with fluorescence confocal microscopy provides additive information on skin morphology.* Dermatol Pract Concept, 2012. **2**(1): p. 3-12.

68. Kim, D.Y., et al., *In vivo volumetric imaging of human retinal circulation with phase-variance optical coherence tomography.* Biomed Opt Express, 2011. **2**(6): p. 1504-13.

69. Villani, E., et al., *In vivo confocal microscopy of meibomian glands in Sjogren's syndrome.* Invest Ophthalmol Vis Sci, 2010. **52**(2): p. 933-9.

70. Denda, S., et al., *Glycolic acid induces keratinocyte proliferation in a skin equivalent model via TRPV1 activation.* J Dermatol Sci, 2010. **57**(2): p. 108-13.

71. Fartasch, M., J. Teal, and G.K. Menon, *Mode of action of glycolic acid on human stratum corneum: ultrastructural and functional evaluation of the epidermal barrier.* Arch Dermatol Res, 1997. **289**(7): p. 404-9.

72. Kim, T.H., et al., *The effects of topical alpha-hydroxyacids on the normal skin barrier of hairless mice.* Br J Dermatol, 2001. **144**(2): p. 267-73.

73. Rasband, W.S., *ImageJ*. 1997-2008, U.S. National Institutes of Health: Bethesda, Maryland, USA.

74. Schindelin, J., et al., *Fiji: an open-source platform for biological-image analysis.* Nat Methods, 2012. **9**(7): p. 676-82.

75. Talreja, P., et al., *Visualization of the lipid barrier and measurement of lipid pathlength in human stratum corneum.* AAPS PharmSci, 2001. **3**(2): p. E13.

76. Menon, G.K., K.R. Feingold, and P.M. Elias, *Lamellar body secretory response to barrier disruption.* J Invest Dermatol, 1992. **98**(3): p. 279-89.

77. Hennessy, A., et al., *The photoadaptive response to ultraviolet exposure in human skin using ultraviolet spectrophotometry.* Photodermatol Photoimmunol Photomed, 2005. **21**(5): p. 229-33.

78. Neppelberg, E., et al., *Dual effects of sodium lauryl sulphate on human oral epithelial structure.* Exp Dermatol, 2007. **16**(7): p. 574-9.

79. Hendriks, A.G., et al., *Are newly discovered drivers of immune-mediated skin disorders expressed in normal skin regenerating from standardized surface injury?* Dermatology, 2014. **228**(3): p. 255-60.

80. Rawlings, A.V. and C.R. Harding, *Moisturization and skin barrier function.* Dermatol Ther, 2004. **17 Suppl 1**: p. 43-8.

81. Bashir, S.J., et al., *Physical and physiological effects of stratum corneum tape stripping.* Skin Res Technol, 2001. **7**(1): p. 40-8.

82. Chilcott, R.P., et al., *Transepidermal water loss does not correlate with skin barrier function in vitro.* J Invest Dermatol, 2002. **118**(5): p. 871-5.

83. Goon, A.T., et al., *Barrier repair in chronic plaque-type psoriasis.* Skin Res Technol, 2004. **10**(1): p. 10-3.

84. Kim, D.W., et al., *Correlation of clinical features and skin barrier function in adolescent and adult patients with atopic dermatitis.* Int J Dermatol, 2006. **45**(6): p. 698-701.

85. Stamatas, G.N., et al., *Documentation of impaired epidermal barrier in mild and moderate diaper dermatitis in vivo using noninvasive methods.* Pediatr Dermatol, 2011. **28**(2): p. 99-107.

86. Bachelor, M., et al., *Transcriptional profiling of epidermal barrier formation in vitro.* J Dermatol Sci, 2014. **73**(3): p. 187-97.

87. Danso, M.O., et al., *An ex vivo human skin model for studying skin barrier repair.* Exp Dermatol, 2015. **24**(1): p. 48-54.

88. Sun, R., et al., *Lowered humidity produces human epidermal equivalents with enhanced barrier properties.* Tissue Eng Part C Methods, 2015. **21**(1): p. 15-22.

89. Kottner, J., et al., *Characterisation of epidermal regeneration in vivo: a 60-day follow-up study.* J Wound Care, 2013. **22**(8): p. 395-400.

90. Sextius, P., et al., *Analysis of gene expression dynamics revealed delayed and abnormal epidermal repair process in aged compared to young skin.* Arch Dermatol Res, 2015.

91. Sabadotto, M., et al., *In vivo assessment of the effect of a cream containing Avena Rhealba((R)) extract and hyaluronic acid on the restoration of the skin barrier in de-epidermised skin produced with an erbium-YAG laser.* Eur J Dermatol, 2014. **24**(5): p. 583-8.

92. Czaika, V., et al., *Comparison of transepidermal water loss and laser scanning microscopy measurements to assess their value in the characterization of cutaneous barrier defects.* Skin Pharmacol Physiol, 2012. **25**(1): p. 39-46.

93. Meinke, M.C., et al., *Characterization of atopic skin and the effect of a hyperforin-rich cream by laser scanning microscopy.* J Biomed Opt, 2015. **20**(5): p. 051013.

94. Grove, G.L., et al., *Computerized evaporimetry using the DermaLab® TEWL probe.* Skin Research and Technology, 1999. **5**(1): p. 9-13.

95. Kang, H., B. Jung, and J.S. Nelson, *Polarization color imaging system for on-line quantitative evaluation of facial skin lesions.* Dermatol Surg, 2007. **33**(11): p. 1350-6.

96. Park, S.B., et al., *Time course of ultraviolet-induced skin reactions evaluated by two different reflectance spectrophotometers: DermaSpectrophotometer and Minolta spectrophotometer CM-2002.* Photodermatol Photoimmunol Photomed, 2002. **18**(1): p. 23-8.

97. Squier, C.A., *The stretching of mouse skin in vivo: effect on epidermal proliferation and thickness.* J Invest Dermatol, 1980. **74**(2): p. 68-71.

98. Silver, F.H., L.M. Siperko, and G.P. Seehra, *Mechanobiology of force transduction in dermal tissue.* Skin Res Technol, 2003. **9**(1): p. 3-23.

99. Xu, W., et al., *The expression of proinflammatory genes in epidermal keratinocytes is regulated by hydration status.* J Invest Dermatol, 2014. **134**(4): p. 1044-55; quiz e15.

100. Menon, G.K., et al., *Localization of calcium in murine epidermis following disruption and repair of the permeability barrier.* Cell Tissue Res, 1992. **270**(3): p. 503-12.

101. Kubo, A., et al., *The stratum corneum comprises three layers with distinct metal-ion barrier properties.* Sci. Rep., 2013. **3**.

102. Doucet, J., et al., *Micron-scale assessment of molecular lipid organization in human stratum corneum using microprobe X-ray diffraction.* J Lipid Res, 2014. **55**(11): p. 2380-8.

103. van Logtestijn, M.D., et al., *Resistance to water diffusion in the stratum corneum is depth-dependent.* PLoS One, 2015. **10**(2): p. e0117292.

104. Brancaleon, L., G. Lin, and N. Kollias, *The in vivo fluorescence of tryptophan moieties in human skin increases with UV exposure and is a marker for epidermal proliferation.* J Invest Dermatol, 1999. **113**(6): p. 977-82.

105. Kucharekova, M., P.C. Van De Kerkhof, and P.G. Van Der Valk, *A randomized comparison of an emollient containing skin-related lipids with a petrolatum-based emollient as adjunct in the treatment of chronic hand dermatitis.* Contact Dermatitis, 2003. **48**(6): p. 293-9.

106. Mao-Qiang, M., et al., *Exogenous nonphysiologic vs physiologic lipids. Divergent mechanisms for correction of permeability barrier dysfunction.* Arch Dermatol, 1995. **131**(7): p. 809-16.

107. Welzel, J., K.P. Wilhelm, and H.H. Wolff, *Skin permeability barrier and occlusion: no delay of repair in irritated human skin.* Contact Dermatitis, 1996. **35**(3): p. 163-8.

108. Zhao, H., et al., *Portulaca oleracea L. aids calcipotriol in reversing keratinocyte differentiation and skin barrier dysfunction in psoriasis through inhibition of the nuclear factor kappaB signaling pathway.* Exp Ther Med, 2015. **9**(2): p. 303-310.

109. Janssens, M., et al., *Increase in short-chain ceramides correlates with an altered lipid organization and decreased barrier function in atopic eczema patients.* J Lipid Res, 2012. **53**(12): p. 2755-66.

110. Berthaud, F. and M. Boncheva, *Correlation between the properties of the lipid matrix and the degrees of integrity and cohesion in healthy human Stratum corneum.* Exp Dermatol, 2011. **20**(3): p. 255-62.

111. Bouwstra, J.A. and M. Ponec, *The skin barrier in healthy and diseased state.* Biochim Biophys Acta, 2006. **1758**(12): p. 2080-95.

112. Lee, M.H., et al., *Effect of composition on water permeability of model stratum corneum lipid membranes.* Soft Matter, 2012. **8**(5): p. 1539-1546.

113. Marschewski, M., et al., *Electron spectroscopic analysis of the human lipid skin barrier: cold atmospheric plasma-induced changes in lipid composition.* Experimental Dermatology, 2012. **21**(12): p. 921-925.

114. Bleck, O., et al., *Two ceramide subfractions detectable in Cer(AS) position by HPTLC in skin surface lipids of non-lesional skin of atopic eczema.* J Invest Dermatol, 1999. **113**(6): p. 894-900.

115. Janssens, M., et al., *Electron diffraction study of lipids in non-lesional stratum corneum of atopic eczema patients.* Biochimica et Biophysica Acta (BBA) - Biomembranes, 2013. **1828**(8): p. 1814-1821.

116. Pilgram, G.S., et al., *Aberrant lipid organization in stratum corneum of patients with atopic dermatitis and lamellar ichthyosis.* J Invest Dermatol, 2001. **117**(3): p. 710-7.

117. Lavrijsen, A.P., et al., *Reduced skin barrier function parallels abnormal stratum corneum lipid organization in patients with lamellar ichthyosis.* J Invest Dermatol, 1995. **105**(4): p. 619-24.

118. Wohlrab, J., et al., *Noninvasive characterization of human stratum corneum of undiseased skin of patients with atopic dermatitis and psoriasis as studied by Fourier transform Raman spectroscopy.* Biopolymers, 2001. **62**(3): p. 141-6.

119. Thakoersing, V.S., et al., *Nature versus nurture: does human skin maintain its stratum corneum lipid properties in vitro?* Experimental Dermatology, 2012. **21**(11): p. 865-870.

120. Ananthapadmanabhan, K.P., S. Mukherjee, and P. Chandar, *Stratum corneum fatty acids: their critical role in preserving barrier integrity during cleansing.* Int J Cosmet Sci, 2013. **35**(4): p. 337-45.

121. Benfeldt, E., J. Serup, and T. Menne, *Effect of barrier perturbation on cutaneous salicylic acid penetration in human skin: in vivo pharmacokinetics using microdialysis and non-invasive quantification of barrier function.* Br J Dermatol, 1999. **140**(4): p. 739-48.

122. Coderch, L., et al., *The effect of liposomes on skin barrier structure.* Skin Pharmacol Appl Skin Physiol, 1999. **12**(5): p. 235-46.

123. Rodriguez, G., et al., *Bicellar systems to modify the phase behaviour of skin stratum corneum lipids.* Phys Chem Chem Phys, 2012. **14**(42): p. 14523-33.

124. Barbosa-Barros, L., et al., *Lipid nanostructures: self-assembly and effect on skin properties.* Mol Pharm, 2009. **6**(4): p. 1237-45.

125. Tanojo, H., et al., *In vivo human skin barrier modulation by topical application of fatty acids.* Skin Pharmacol Appl Skin Physiol, 1998. **11**(2): p. 87-97.

126. Diraman, H. and H. Dibeklioglu, *Characterization of Turkish Virgin Olive Oils Produced from Early Harvest Olives.* Journal of the American Oil Chemists' Society, 2009. **86**(7): p. 663-674.

127. Mailer, R., *Rapid evaluation of olive oil quality by NIR reflectance spectroscopy.* Journal of the American Oil Chemists' Society, 2004. **81**(9): p. 823-827.

128. Patzelt, A., et al., *In vivo investigations on the penetration of various oils and their influence on the skin barrier.* Skin Res Technol, 2012. **18**(3): p. 364-9.

129. Nanayakkara, G.R., et al., *The effect of unsaturated fatty acids in benzyl alcohol on the percutaneous permeation of three model penetrants.* Int J Pharm, 2005. **301**(1-2): p. 129-39.

130. Takeuchi, Y., et al., *Skin penetration enhancing action of cis-unsaturated fatty acids with omega-9, and omega-12-chain lengths.* Biol Pharm Bull, 1998. **21**(5): p. 484-91.

131. Abramoff, M.D., P.J. Magelhaes, and S.J. Ram, *Image processing with ImageJ.* Biophotonics International, 2004. **11**(7): p. 36-42.

132. Schindelin, J. *Fiji Is Just ImageJ (batteries included)*. in *ImageJ User and Developer Conference*. 2008. Luxembourg.

133. Mack Correa, M.C., et al., *Molecular interactions of plant oil components with stratum corneum lipids correlate with clinical measures of skin barrier function.* Experimental Dermatology, 2014. **23**(1): p. 39-44.

134. Zhang, Q., et al., *Infrared Spectroscopic Imaging Tracks Lateral Distribution in Human Stratum Corneum.* Pharm Res, 2014: p. 1:12.

135. Bommannan, D., R.O. Potts, and R.H. Guy, *Examination of stratum corneum barrier function in vivo by infrared spectroscopy.* J Invest Dermatol, 1990. **95**(4): p. 403-8.

136. Brancaleon, L., et al., *Attenuated total reflection-Fourier transform infrared spectroscopy as a possible method to investigate biophysical parameters of stratum corneum in vivo.* J Invest Dermatol, 2001. **116**(3): p. 380-6.

137. Mao, G., et al., *Oleic Acid Disorders Stratum Corneum Lipids in Langmuir Monolayers.* Langmuir, 2013.

138. Danby, S.G., et al., *Effect of olive and sunflower seed oil on the adult skin barrier: implications for neonatal skin care.* Pediatr Dermatol, 2013. **30**(1): p. 42-50.

139. Viola, P. and M. Viola, *Virgin olive oil as a fundamental nutritional component and skin protector.* Clin Dermatol, 2009. **27**(2): p. 159-65.

140. Mao, G., et al., *Imaging the distribution of sodium dodecyl sulfate in skin by confocal Raman and infrared microspectroscopy.* Pharm Res, 2012. **29**(8): p. 2189-201.

141. Francoeur, M.L., G.M. Golden, and R.O. Potts, *Oleic acid: its effects on stratum corneum in relation to (trans)dermal drug delivery.* Pharm Res, 1990. **7**(6): p. 621-7.

142. Tanojo, H., et al., *In vitro human skin barrier perturbation by oleic acid: Thermal analysis and freeze fracture electron microscopy studies.* Thermochimica Acta, 1997. **293**(1â€“2): p. 77-85.

143. Naik, A., et al., *Mechanism of oleic acid-induced skin penetration enhancement in-vivo in humans.* Journal of Controlled Release, 1995. **37**: p. 299-306.

144. Ongpipattanakul, B., et al., *Evidence that oleic acid exists in a separate phase within stratum corneum lipids.* Pharm Res, 1991. **8**(3): p. 350-4.

145. Rowat, A.C., N. Kitson, and J.L. Thewalt, *Interactions of oleic acid and model stratum corneum membranes as seen by 2H NMR.* Int J Pharm, 2006. **307**(2): p. 225-31.

146. Hoopes, M.I., et al., *Bilayer Structure and Lipid Dynamics in a Model Stratum Corneum with Oleic Acid.* The Journal of Physical Chemistry B, 2011. **115**(12): p. 3164-3171.

147. Wang, X., et al., *Characterization of mimetic lipid mixtures of stratum corneum.* Colloids Surf B Biointerfaces, 2010. **78**(1): p. 92-100.

148. Wertz, P.W. and D.T. Downing, *Ceramides of pig epidermis: structure determination.* J Lipid Res, 1983. **24**(6): p. 759-65.

149. Mao, G., et al., *Oleic Acid Disorders Stratum Corneum Lipids in Langmuir Monolayers.* Langmuir, 2013. **29**(15): p. 4857-65.

150. Henon, S. and J. Meunier, *Microscope at the Brewster angle: Direct observation of first-order phase transitions in monolayers.* Review of Scientific Instruments, 1991. **62**(4): p. 936-939.

151. Hoenig, D. and D. Moebius, *Direct visualization of monolayers at the air-water interface by Brewster angle microscopy.* The Journal of Physical Chemistry, 1991. **95**(12): p. 4590-4592.

152. Dennin, M., *Langmuir Monolayers*, in *Experimental and Computational Techniques in Soft Condensed Matter Physics*, J. Olafsen, Editor. 2010, Cambridge University Press.

153. Chen, X., et al., *Fatty acids influence "solid" phase formation in models of stratum corneum intercellular membranes.* Langmuir, 2007. **23**(10): p. 5548-56.

154. Kitson, N., et al., *A model membrane approach to the epidermal permeability barrier.* Biochemistry, 1994. **33**(21): p. 6707-15.

155. Janssens, M., et al., *Lamellar lipid organization and ceramide composition in the stratum corneum of patients with atopic eczema.* J Invest Dermatol, 2011. **131**(10): p. 2136-8.